Scanning tunneling microscopy of layered materials

by

Xiaorong Qin

B.Sc. Tsinghua University (Beijing, China) 1983

M.Sc. Tsinghua University (Beijing, China) 1986

A THESIS SUBMITTED IN PARTIAL FULFILLMENT OF

THE REQUIREMENTS FOR THE DEGREE OF

DOCTOR OF PHILOSOPHY

in the Department

of

Physics

SIMON FRASER UNIVERSITY

August 1992

ISBN 0-315-83755-1

Approval

Name: Xiaorong Qin

Degree: Doctor of Philosophy

Title of Thesis: Scanning tunneling microcopy of layered materials

Examining Committee:

Chairman: Dr. M. L. W. Thewalt

Dr. J. C. Irwin
Senior Supervisor

Dr. G. Kirczenow

Dr. R. F. Frindt

Dr. B. Frisken

Dr. Inder P. Batra
External Examiner
IBM Almaden Research Center

Date Approved: Aug 26/92

PARTIAL COPYRIGHT LICENSE

I hereby grant to Simon Fraser University the right to lend my thesis, project or extended essay (the title of which is shown below) to users of the Simon Fraser University Library, and to make partial or single copies only for such users or in response to a request from the library of any other university, or other educational institution, on its own behalf or for one of its users. I further agree that permission for multiple copying of this work for scholarly purposes may be granted by me or the Dean of Graduate Studies. It is understood that copying or publication of this work for financial gain shall not be allowed without my written permission.

Title of Thesis/Project/Extended Essay

Scanning Tunneling Microscopy of Layered Materials

Author:

(signature)

XIAORONG ZHAI

(name)

Aug. 28, 1992

(date)

Abstract

This dissertation describes studies of the surfaces of layered materials, including graphite intercalation compounds, transition-metal-dichalcogenides, and single layers of MoS_2, with scanning tunneling microscopy (STM).

In order to understand how tunneling images reflect the atomic nature of sample surfaces, the electronic and structural properties of intercalated graphite surfaces imaged with STM have been investigated theoretically. The corrugation amplitude (CA) and carbon site asymmetry (CSA) are sensitive to the number of graphite layers covering the first intercalate layer, to the amount and distribution of the charge transferred from intercalate to host and to the surface subband structure. The CA and CSA can be used to map the stage domains across a freshly cleaved surface. The STM images of the surfaces of both donor and acceptor graphite intercalation compounds are discussed. The theory successfully explained the available experimental results, and yielded some predictions which have been verified in recent experiments.

A STM system for operation in air was assembled. The crystalline surfaces of graphite and three transition-metal-dichalcogenides (2*H*-MoS_2, WTe_2 and $ReSe_2$) have been studied with the STM system.

Single layers of MoS_2 can be obtained by the exfoliation of lithium-intercalated MoS_2 powder in water and in several alcohols. In the STM observations, the samples were prepared by depositing either an aqueous or butanol suspension of single-layer MoS_2 on graphite substrates to form restacked films with two monolayers of solvent molecules included between the layers of MoS_2. The real-space images obtained from the films all showed the existence of an approximate 2x1 superstructure on the surfaces, although the 2x1 pattern can be modulated by the interface interaction between the MoS_2 layer and the solvent molecules. These results, in conjunction with existing x-ray diffraction and Raman

results, imply that the single layers of MoS_2 adopt a distorted octahedral structure. In addition, STM images have been obtained from dry restacked MoS_2 films and these indicate that on drying the structure transforms back to the hexagonal MoS_2 pattern.

To my parents

Acknowledgements

It is my pleasure to thank many people who had given various advices and assistances in the work presented here. Specially, I thank Professor J. C. Irwin, my senior supervisor, for providing very supportive and helpful conditions throughout the work. He always gave me gracious encouragement, and allowed me to choose my own approaches and to learn from the practices. I have also learned and benefited from his working and writing style, a way to quickly focus on the point of a problem with simple and clear steps. His supervisions and optimism made the work presented in this thesis possible.

I am indebted to Professor G. Kirczenow, whom I worked with for more than one year on the theory of STM imaging of intercalated graphite. It was a privilege to study so closely from a leading expert of the theory of intercalation compounds. His direct and educational instructions on the subject, and his kind encouragement made me confident to finish the theoretical part of the thesis. By trying to convince him each step of the calculations, I have not only benefited from numerous afternoon discussions with him, but also from his advices on subjects other than physics alone, which will also be very helpful in my future scientific career.

Thanks go to Professor R. F. Frindt, for supplying so many interesting samples which provided an excellent application field of the STM. During the collaboration on the single-layer MoS_2 studies, his kind advices and his humor made the work in the group more enjoyable.

The members of Prof. Frindt research group supported the work in several ways. Per Joensen gave me his valuable advices in many techniques in the lab when I first started the experimental work. R. Divigalpitiya provided me single-layer MoS_2 films on glasses at the beginning of the project, the successful imaging of the single layers was based on this

initial experience. I have benefited from discussions with R. Divigalpitiya on the single-layer MoS_2 properties, and have enjoyed the collaboration work with D. Yang.

I am very appreciative of the continuing encouragement and support given by my husband and my fellow student, Detong Jiang, during the years of work of the thesis.

Lastly, I wish to express my gratitude to the members of my examining committee for their comments on this thesis.

Table of Contents

List of Figures

Chapter 2

Chapter 3

Chapter 4

Chapter 5

Chapter 6

Chapter 1

Introduction

The scanning tunneling microscope (STM),[1, 2] a superb tool for surface science, was invented by Binnig, Rohrer, and co-workers in 1981.[3-5] It enables one to image geometric and electronic surface structures directly with atomic resolution, and hence to "see" the real world of surfaces atom by atom. The famous example for people to realize the importance of STM is that the 7x7 reconstruction of the silicon (111) surface was demonstrated in the STM image,[6] which was a puzzle that had remained unsolved for 25 years. Beyond real-space imaging, there are also expanding methods of using STM, for instance, to include other probe-sample interactions like forces,[7] or to manipulate atomic and molecular entities on surfaces to intentionally induce permanent local structural or chemical modifications.[8-11]

In the past decade many types of STM's have been made[1, 12-14] in order to have them operate under various conditions. For instance, STM's are operated in an ultra-high-vacuum (UHV) environment for observing surface structure and the growth of metals and semiconductors,[6] in liquid nitrogen or liquid helium for imaging charge-density waves in some transition metal chalcogenides,[15, 16] and in air at ambient pressure for studying inert surfaces of layered materials.[17]

A STM in air has advantages in many ways. Obviously, the controls are easily accessed, and one has considerable freedom in operating the STM. Also, the apparatus is simplified, and hence the structure is compact and vibrations are correspondingly minimized. However, the samples have to be limited to those whose surfaces are

chemically inert and free from contamination in air or easy to cleave. Layered materials, such as graphite and transition-metal-dichalcogenides, satisfy the above conditions and provide valid experimental objects. In particular, if a layered material contains water or alcohol between the layers, then the STM observations in air are necessarily required and an UHV environment would not be appropriate. The main purpose of this thesis is to understand theoretically how a surface electronic structure determines the STM image by means of studying graphite intercalation compounds, and to determine experimentally the atomic structures of some transition metal dichalcogenide crystals and single layers of MoS_2 in liquid suspensions by using a STM in air.

In this introductory chapter, I start with a brief discussion of the basic principle of STM and its operation modes. Then I move to the theoretical understanding of the mechanism of STM. Finally, I give an overview of the work presented in this thesis.

1.1 The principle of STM

STM is based on the principle of electron tunneling. There are two fundamental components to form the tunneling unit, the conducting sample under observation and a conducting fine tip (ideally terminating in a single atom). To generate tunneling, the tip-to-surface distance has to be reduced to a few angstroms, and a small bias voltage applied to the tunneling unit to cause electrons to tunnel between them. The tunneling current is roughly proportional to the overlap of the charge densities between the tip and sample surface, and hence depends exponentially on the tip-to-surface separation. Such extreme sensitivity of the tunneling current to the tip-to-surface distance is the key to the extremely high resolution of the STM. By taking advantage of this relationship and using piezoelectric

elements to electronically control the tip motions, the STM can effectively "map" the atomic structure of the sample surface.

One way of using the STM is called the constant-current mode. By adjusting the z-position of the tip with a feedback circuit while tip scanning across the surface, the tunneling current is monitored and regulated to the preset demand value thousands of times per second. A constant tunneling current is thus maintained, and the tip z-motion will trace out the profile of the sample surface. Usually, the image has a close relation with the surface topography.

Another way of using STM is called constant-height mode. In this mode, the tip height is not changed during the scan, and the STM measures the tunneling current which changes as the tip-to-surface distance varies in the scan. Smooth surfaces with corrugation amplitudes less than the average tunneling distance, can be imaged by recording the tunneling-current deviations instead of the z-displacement of the tip. A faster scan speed is possible in the constant-height mode and thus the information can be moved into a higher frequency range where the low frequency noise is minimized. The constant-height mode image can also be called the current image.

No matter which mode of operation is used, tunneling at positive tip bias with respect to the sample accesses the filled states of the sample surface since electrons tunnel from the sample toward the tip; while at negative tip bias we are probing the empty states because electrons tunnel from the tip toward the sample surface.

1.2 Theoretical models

A theoretical understanding of the mechanism of STM is essential to enable an interpretation of the experimental results. Particularly, a realistic and practical theoretical model to describe the atomic resolution nature of STM images would be most desirable.

The existing theories can be classified into two groups.[18] One is based on a free-electron model in which the tip and the surface are characterized as box electrodes containing free electrons.[19] The other is based on a transfer Hamiltonian approach[20] with the surface characterized by its atomic structure.

The former group is an extension to the traditional one-dimensional tunnel theory. The description of the wave function tail of the tunnel electron in the tip-surface gap and the image potential in the gap region can be effectively treated by the theories. Thus the models can evaluate the electron transmission probabilities through the tip-surface gap rather rigorously, and give more accurate information of the tunneling current as a function of the bias voltage and of the tip-surface distance. However, the atomic nature of the tip-surface system is difficult to describe in the framework of these models.

The second group is more realistic in terms of the atomic structure of the tunneling unit. The tunneling barrier is treated as a perturbing Hamiltonian, in which two electrodes (tip and sample) are regarded as two independent systems with very weak coupling, and an electron can transfer from a state of one electrode to a state of the other one. In this approach, the careful description of the wave function tail or the image potential in the gap are supposed to be of minor importance, because the STM image is determined by the relative change of the tunneling current over the surface and not necessarily its absolute value. Based on the first order time-dependent perturbation theory, the tunneling current can be described by[20-22]

$$I \sim \int_{-\infty}^{\infty} dE\ \rho_s(E+eV)\rho_t(E)\ |M(E)|^2\ [f(E) - f(E+eV)] \qquad (1)$$

where M is the tunneling matrix element, $f(E) = \{\ 1 + exp[(E - E_F)/k_BT\ ]\}^{-1}$ is the Fermi function, V is the bias potential between the sample and the tip, and ρ_s and ρ_t are the

densities of states in the sample and the tip, respectively. We see that the tunneling current is proportional to the convolution of the electronic states of sample and tip.

Tersoff and Hamann[23, 24] introduced the use of a transfer Hamiltonian approach. By modeling an *s* wave function tip, they showed that the tunneling current could be simplified in the low voltage and low temperature limit to the local density of states (LDOS) of the sample evaluated at the center of the tip,

$$I \propto \rho_S(\mathbf{r},E_F) = \sum_{\mathbf{k}n} |\Psi_{\mathbf{k}n}(\mathbf{r})|^2 \delta(E_{\mathbf{k}n}-E_F) \qquad (2)$$

where $\mathbf{r}$ is the center of curvature of the tip and $\Psi_{\mathbf{k}n}(\mathbf{r})$ and $E_{\mathbf{k}n}$ are the electron eigenstates and energy eigenvalues of the sample. This relation shows that the tunneling tip follows a contour of constant local density of the surface states in the constant-current mode. At low bias voltage, only the states near the Fermi level of the sample contribute to the tunneling current.

Tersoff and Hamann's theory is attractive because the problem of understanding the STM image simply becomes the evaluation of the local density of states at the surface, irrespective of the tip state. The theory is important and relatively practical in focusing on the relationship between the tunneling current and the atomic structure of the sample surface. In fact, the Tersoff and Hamann theory provides a good interpretation of many STM images, for instance, the anomalous features in the image of graphite surface.[25, 26] In this thesis, I am interested in how the tunneling image reflects the surface electronic structure, and hence the transfer Hamiltonian approach of Tersoff and Hamann is used.

One should keep in mind, however, that equation (1) represents the tunneling process in a more general way, in that the tip may have a profound impact on the appearance of the STM image. It is true that in experiments the geometric (multi-tip)[27] and electronic (not *s*

but d_{z^2} state)[28] properties of the tip are found to dramatically influence the STM image. Since the tip state is always difficult to determine *in situ* in the usual experimental system (though people propose to obtain ρ_t by means of analyzing the simultaneously acquired local tunneling spectra in UHV[29]), the image interpretation, particularly on the atomic scale, can be rather subtle. One has to recognize the existence of tip effects and exercise caution in the image interpretation.

1.3 Overview of the thesis

There are two sections in this thesis: a theoretical section on electronic structure calculations for STM images of graphite and graphite intercalation compounds (Chapter 3); and an experimental section on the atomic scale imaging of layered materials including graphite (Chapter 2), transition-metal-dichalcogenides 2*H* -MoS_2, WTe_2 and $ReSe_2$ (Chapter 4), and a novel material—single layer MoS_2 (Chapter 5-6).

Chapter 2 describes the assembly and properties of a STM designed to operate in air. Graphite images obtained with the STM are presented, which demonstrate the capability and quality of the apparatus. The graphite images show two remarkable anomalies which differ drastically from the surface topography, and which can be explained in terms of the electronic structure of the surface. Some multi-tip effects are also presented.

In Chapter 3, a theory of the STM images of graphite and graphite intercalation compounds is presented. The theory is based on the Tersoff and Hamann model that STM images depend on the local electron density of states (LDOS) of the sample surface at the Fermi level. Since the graphite stacking sequence and electronic structure can be modified by intercalation of electron donor and acceptor species, the STM images of graphite intercalation compounds (GIC's) should provide information useful to elucidate further the

electronic origins of the two anomalies found in a pristine graphite image. Also, the results can be used to map surface domains of different graphite layers above the first intercalate layer close to the surface. Our theoretical calculations for the image of pristine graphite represent the two anomalous features and are in good agreement with those obtained using different theoretical methods, indicating that the theory is reasonably valid. Our theory is applicable to both donor and acceptor intercalate species and to different staged structures. Our calculations of the images of GIC's have yielded several predictions which have been evidenced in some recent experimental data.

Chapter 4 is devoted to the experimental studies of the crystalline surfaces of 2*H* - MoS_2, WTe_2 and $ReSe_2$ with the STM described in Chapter 2. Atomic-resolution images show the expected basal plane projection lattices, however, the internal structures within the unit cells are often dependent on the tip properties. Though it is difficult to determine whether Mo or S atoms have been observed in the STM image, the STM images of $ReSe_2$ and WTe_2 are primarily due to the chalcogen layers on the top surface but with clear influences from the metal layers underneath. We then compare the structure differences and similarities between the three crystals, which might give certain hints to the structural transformations of the novel material described in Chapter 5 and Chapter 6.

In Chapter 5 and Chapter 6, single layers of MoS_2 have been studied with the STM in air. The single molecular layers are obtained by exfoliation of Li-intercalated MoS_2 in water and in alcohols. When either an aqueous or butanol suspension of single-layer MoS_2 is deposited on graphite substrates, restacked films will be formed with solvent molecules included between layers of MoS_2. The STM images obtained from both types of films show that the unit cell of the single layers corresponds to an approximate 2x1 superlattice of the hexagonal 2*H* -MoS_2 structure, though the "2x1" pattern can be modulated by the interface interaction between the MoS_2 layer and the solvent molecules. The image of dry

restacked MoS_2 obtained from an aqueous suspension transforms back to the hexagonal MoS_2 pattern. We then speculate on the mechanism of the role of the suspension liquid in modifying the electronic structure of MoS_2 at the end of Chapter 6.

In Chapter 7, we present a summary of the thesis and discuss possible directions that future experiments might take.

Chapter 2

A scanning tunneling microscope in air

The main instrumental problems to be overcome to enable one to obtain atomic resolution STM images are those associated with the mechanical stability of the tip-surface gap which exponentially determines the tunneling current. The STM must achieve and maintain precise tip-surface distance within fractions of an Å throughout the time required to obtain a complete image (~1 min.). Such stability is mainly limited by vibrations transmitted to the tunneling unit or created in the scanning process itself. Usually the external vibrations are blocked by a vibration-isolation system, for instance, by a spring suspension system. The influence of internal vibrations is reduced by mechanical rigidity and an electrical low-pass filter (or an integrator) in the feedback loop. The idea of mechanical rigidity is to make the mechanical eigenfrequencies of the tunneling unit much greater than the tip scan rate (controlling the raster scan motion of the tip), the bandwidth of the feedback loop (controlling the vertical motion of the tip) and the frequencies of significant external vibrations. Therefore, the tip motion is limited to frequencies below the lowest mechanical eigenfrequency, such that all the mechanical eigenfrequencies cannot be excited in the scanning process or excited externally.

There are other problems in regard to a STM design, such as those associated with material thermal drift, piezoelectric elements properties, and the coupling between x, y and z drive arms (e.g. the x-y motion is not entirely orthogonal to z). These factors may cause distortion of the image, and hence influence the quality of the results.

In order to reproducibly achieve atomic resolution images the sharpness and the physical and chemical stability of the tunneling tip are critical. Currently, the most popular tip materials being used are tungsten and $Pt_{0.8}$-$Ir_{0.2}$ wires. The standard methods of obtaining workable tips are electrochemical etching[13, 30] and mechanical grinding or cutting. But the *in situ* tip structure is difficult to determine, since the tip is often reformed during imaging because of tip-surface interactions associated with the scanning and tunneling process. As we know, with the tip positively biased , the electrons from occupied states in the sample tunnel to the empty states of the tip; on the other hand, with the tip negatively biased, the tunneling current is determined by the occupied states of the tip and the empty states of the sample. In other words, the tunneling current is determined by a convolution of the sample density of states (DOS) and the tip DOS.[31] The tip thus may induce some artifacts in the surface image, and one must therefore exercise caution in the image interpretation.

In this chapter, the assembly and properties of a STM designed to operate in air are described. Following this, some graphite images obtained with the microscope will be presented, which served to establish the capability of the apparatus and to introduce the author to practical STM techniques.

2.1 Instrumentation

The STM head used for all of the work in this thesis is shown in Fig.2-1. This STM head was built by Jericho *et al* at Dalhousie University, and is similar to their previous design.[32]

The main support frame is machined from two pieces of brass and the whole structure is pocket size (~ 9cm in height) in order to achieve high mechanical rigidity. Also the

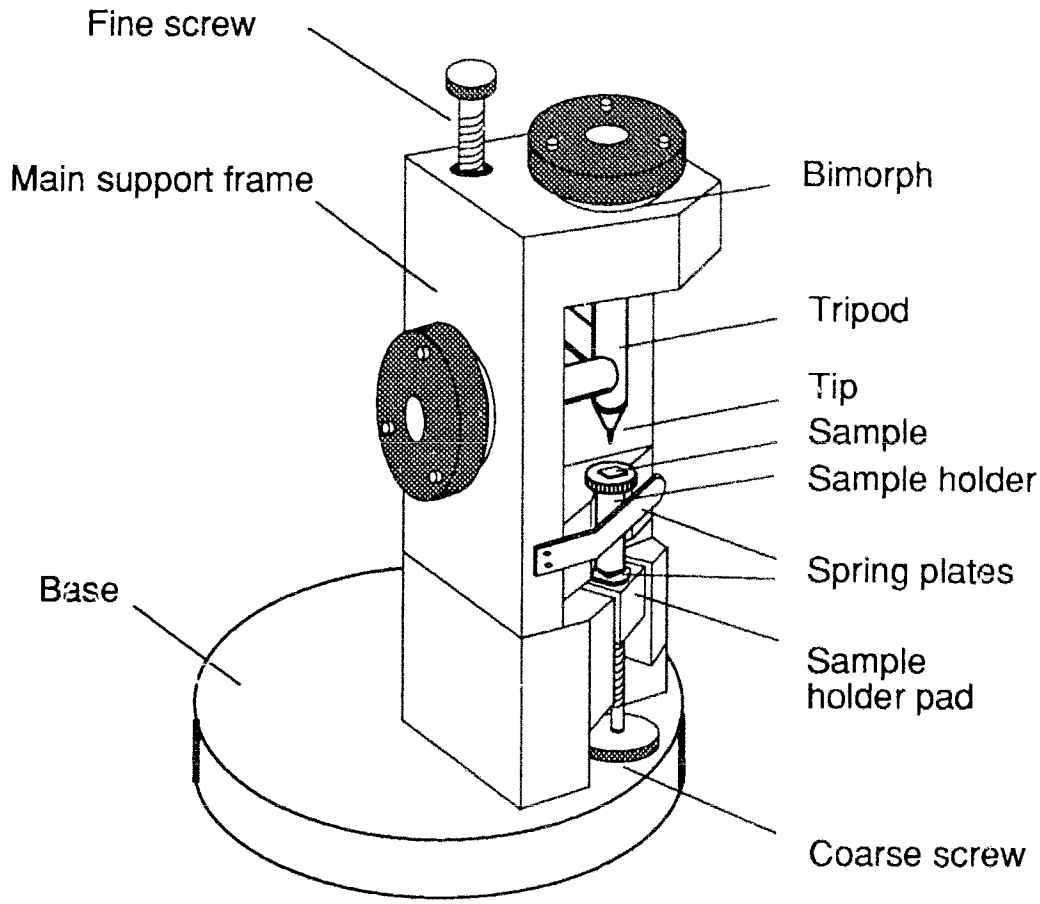

Fig.2-1: Drawing of mechanical parts of the instrument.

tripod, sample holder, sample holder pad, mechanical coarse and fine positioning screws, and the base (~6.3cm in diameter and 1.3cm thick) for holding the support frame are all constructed of brass. Therefore, thermal drifts caused by using materials with different expansion coefficients are greatly reduced.

The tip holder is fixed on a rigid tripod configuration and its movements are controlled with three identical bimorph piezoelectric disks. The bimorph consists of two Channel 5800 piezo disks,[33] each disk is 14mm in diameter and 1mm thick. When a positive voltage signal is applied to the z-bimorph, the effect is to drive the tip down and thus shorten the tip-surface distance. The sensitivities of the x and y bimorphs were calibrated using graphite images and were about 8.8 Å/V and 10.3 Å/V, respectively. In actual experiments, graphite images are always used to calibrate atomic-resolution images of the surface under observation. For large scale imaging, that is, for areal scans greater than 200Å x 200Å, we have to use the measured bimorph sensitivities to determine the dimensions of surface features, since in this case the graphite lattice constant is too small to be resolved and thus cannot be used for the scale calibration. One can measure the scan voltages applied to the x and y piezoelectric bimorphs, and multiply them by the corresponding sensitivities to find the scanning range.

Commercial 0.25-mm or 0.5-mm diameter $Pt_{0.8}$-$Ir_{0.2}$ tips[34] were used for the work presented in this thesis. They were used either directly or after a mechanical resharpening treatment. The tip wire was mounted tightly into a stainless steel syringe needle with very good conduction between them. The syringe needle was glued with insulating 5-minute epoxy on a conically shaped brass holder which screws into the end of the z-axis drive arm. Electrical connection to the tip is made by soldering a fine insulated wire on the syringe needle and leading the wire to the outside circuit. Every tip was gently washed with 2-propanol before use.

Usually, a sample is glued onto a thin glass plate to insulate it from the sample holder, and then mounted on the horizontal face of the holder with 5-minute epoxy. Electrical connection to a sample can be made by gluing a very fine copper lead wire on the sample surface with conductive silver paste and connecting the other end of the wire to the feedback circuit.

The "T" shaped brass sample holder (see Fig.2-1) is mounted by two copper spring plates. One holds it tightly and presses it horizontally toward the main support frame and the other one holds it vertically from the bottom. One end of vertical spring plate is fixed on the middle of a brass pad, which is not shown in Fig.2-1, and the sample holder sits on the other end. The brass pad has two threaded holes, a mechanical coarse-positioning screw passes through one hole pointing directly to the free end of the lower spring plate, and the fine-positioning screw uses the other hole placed on the other end of the pad far (~ 3 cm) from the sample holder. If either the coarse or the fine positioning screw is adjusted counter-clockwise, the sample holder will be moved upward causing a decrease of the tip-surface gap.

In our lab, the influence of external vibrations is reduced in the following ways. The STM head is put on an extremely heavy table (granite slab on LO-REZ springs) originally used for optical experiments, and several soft papers are put in between the STM head and the table as cushions. A paper box is used over the STM head, which is found very effective to isolate the vibrations caused by air currents and acoustic vibrations in the air. After a tunneling current is established by mechanically coarse and fine positioning the sample holder and electrically positioning the tip, the coarse-positioning screw is retracted and the sample holder is then held in position by the upper spring plate alone. The tunneling unit (tip and sample) is then basically attached to the top piece of brass of the main support frame and vibrations cannot be transferred through the coarse positioning

screw. Meanwhile, the feedback circuit will provide an offset signal to maintain the tunneling current, compensating any change to the tip-surface gap during the operation. This procedure was suggested by Dalhousie University and was found effective in reducing the relevant mechanical vibrations.

2.2 Electronics

The block diagram of our STM electronics is shown in Fig.2-2. The important parts for the STM are a conducting tip held by a tripod and a conducting sample surface. As the tip-surface gap approaches a distance of ~ 10Å,[4] electrons can tunnel with a reasonable probability between the tip and surface. A bias voltage is applied to the tip, the sample is virtually grounded, and the resulting current is a sensitive measure of the tip-sample separation. A feedback loop is used to control tip z displacement. While the tunneling tip is scanned laterally across the surface with x and y bimorphs controlled by the raster scan circuit, the tunneling information is simultaneously collected by a PC/AT 286 computer (IBM compatible) and displayed on an analog RGB color graphics monitor.

There are two operational modes for the STM:

(1) constant-current mode

The tip-to-surface distance is set by comparing the tunneling current to the demand preset current and is regulated by a negative feedback loop. The feedback amplifier, consisting of a pre-amplifier circuit and a feedback main circuit, is basically the same as that shown in Ref.[32]. In the feedback main circuit, a log amplifier is used to linearize the exponential behavior of tunneling current, a reference-adjust stage is used to set a demand current, and an integrator is used to filter the error signal. The output of the integrator drives the z-bimorph through a high-voltage amplifier (KEPCO BOP1000M)[35] which has

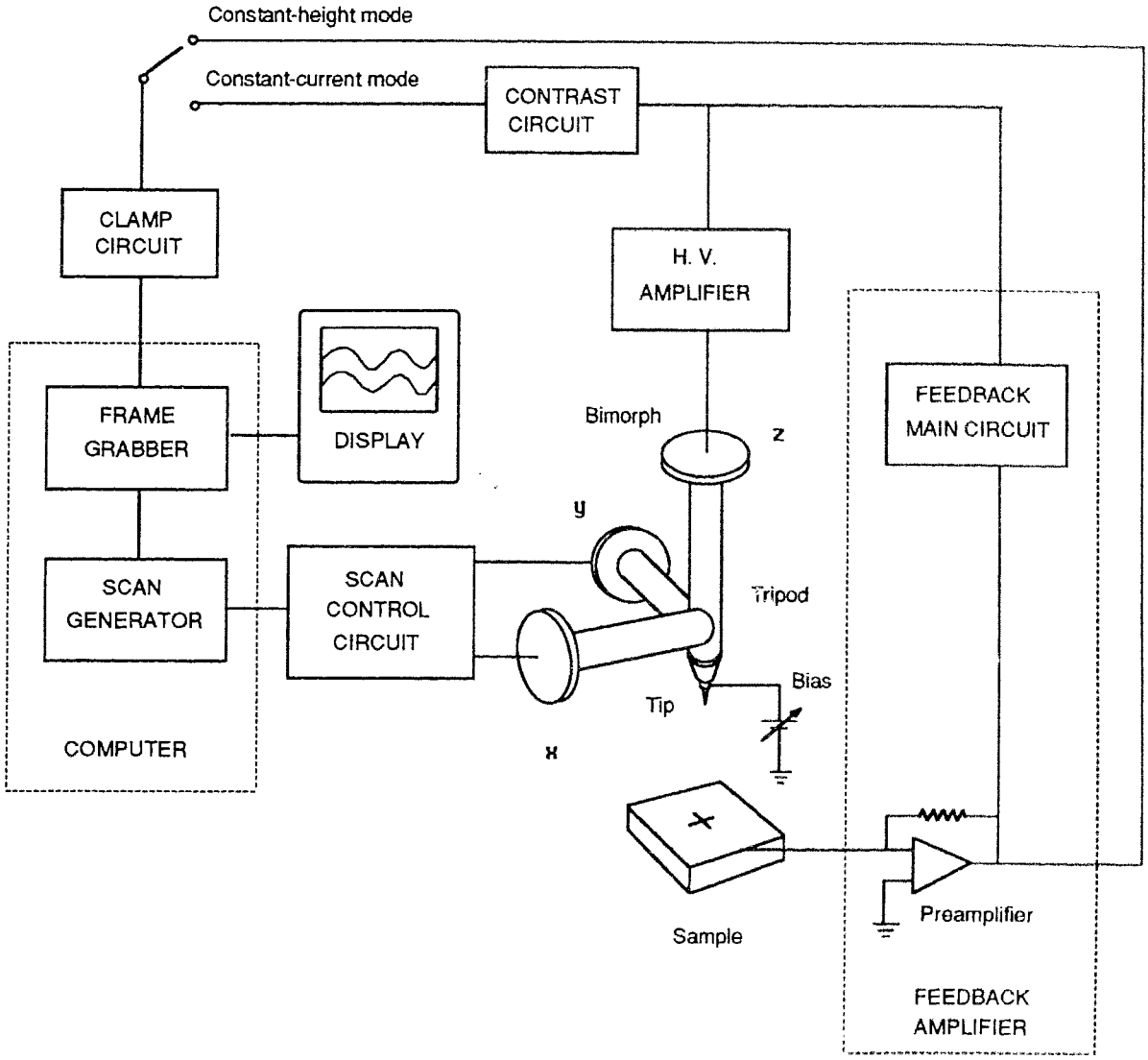

Fig.2-2: Block diagram of the electronic circuitry of the STM.

an output offset range of -1000 to +1000V with a gain of 100. By adjusting time constant ($\tau = R_\tau C$) of the integrator into a small value, one can operate the STM in constant-current mode with proper tip scan rate. As small τ results in fast response of the feedback circuit, and hence fast response to the change in tip-to-surface gap, the feedback system thus can keep the tunneling current constant on a short time scale. The typical τ value used in my experiments is 0.2 ~ 0.6 ms in this mode. As shown in Fig.2-2, the voltage applied to the z-bimorph (before the high-voltage amplifier) is recorded because the tip z-motion reflects the surface profile in this mode. A contrast circuit is used to enlarge or reduce the voltage signal in order to obtain best contrast image on the display monitor.

(2) constant-height mode:

One can apply a steady voltage to the z-bimorph through out the tip scanning, so that the absolute tip height is fixed, and the tunneling current is then recorded. By adjusting the time constant (τ) of the integrator to a large value, we can operate the STM in constant-height mode with fast tip scan rate. As large τ results in slow response of the circuit, hence slow response to the z-displacement of tip, thus the feedback system only keeps the *average* current constant. The typical τ value used in my experiments is 0.1 ~ 0.3 s for the constant-height mode. As shown in Fig.2-2, the tunneling current is taken directly from the output of the pre-amplifier. Since the output sensitivity of the pre-amplifier is 100mV/nA and the typical tunneling current is set about a few nano-amperes in experiments, such that the converted voltage value is large enough that it usually fits properly within the input window of a DT2851 frame grabber board[36] which is inside the computer and thus the amplifying contrast circuit is not necessary here.

A clamp circuit is used to limit the amplitude of electric signal between 0V and 1.2V as required by the input of the frame grabber board in both modes of operation.

Scan control circuits include a rotation circuit and magnification circuits, which are used to drive the x and y piezoelectric bimorphs. Based on raster scan signals generated by a scan generator board inside the computer, the rotation circuit provides the function of rotating the tip scan orientation, with which one can find out if the tip shape is symmetric within the scan plane and rule out the relevant artifacts. The magnification circuits provide the ability to enlarge or reduce the scan signals from the scan generator, and thus control the scan scales. We usually use another two high-voltage amplifiers (KEPCO OPS 1000B)[35] after the outputs of the magnification circuits if large scale imaging is required. As mentioned in Ref.[32], one can safely apply ± 800V to the bimorphs without concern for strain damage, therefore the maximum scale is at least 12000Å in each direction.

All the circuits mentioned above are shown in the Appendix.

A commercial scan generator[37] built inside the computer is used to provide a triangle wave for x scan direction and a wave for incrementing y after every x scan, both with a voltage range of ±5V. The frame grabber board is also a commercial one which is designed for the IBM PC/AT computer. On the monitor screen, the STM images are composed of raster scans, with left-to-right scans displayed and right-to-left scans blanked; the horizontal scan lines proceed from top to bottom, and the upward retrace is also blanked.

Commercial computer software[37] is used for data acquisition and presentation. All the images presented in this thesis are basically raw data without fast Fourier transform filtering.

2.3 Atomic resolution images of graphite with the STM

We can obtain a large atomically flat graphite surface simply by cleaving the sample with Scotch tape in air, and the resulting surface is very clean and inert. Graphite is the

easiest material to be imaged by STM, and the imaging has been used to evaluate instruments and to calibrate other sample images.

Fig.2-3(a) illustrates the structure of graphite, which is very simple with hexagonal layers of carbon atoms stacked in an *ABAB* sequence. The crystal is composed of an α sublattice consisting of atoms with neighbors directly above and below in adjacent layers and a β sublattice consisting of sites without such neighbors.

The STM image of a graphite surface at low bias has two remarkable features, a large corrugation in the tunneling current over the center of each carbon hexagon, and a pronounced asymmetry in the current between adjacent carbon atom sites,[1, 2, 25, 26, 31, 38-40] i.e. the two kinds of carbon-atom sites appear not equivalent and β sites are more visible than α sites (see Fig.2-3(b)). As was shown by Tersoff, [25] the fundamental reason for the corrugation is that the STM probes the local electron density of states at the Fermi level. Since the Fermi surface of graphite is very small, the STM image is a reflection of the spatial dependence of the wave functions of just a few electron states, and the current "hole" at the center of each hexagon is due to a node in the wave functions of the Fermi electrons.[25] Batra *et al.*,[26] and Tomanek and co-workers[39, 40] have shown that the carbon-atom site asymmetry is a property of the electron eigenstates resulting from the *AB* stacking of the graphite.[26, 39, 40] The bonding between the interlayer nearest neighbors affects the surface charge density. We will present a simple tight-binding model shown in Chapter 3 which is also capable of describing the main features of the STM image of pristine graphite.

The microscope described in previous sections has been used to image the surface of a highly oriented pyrolytic graphite (HOPG). In Fig.2-4, the three images were obtained in constant-height mode on three different surface locations of the graphite with a 0.5-mm $Pt_{0.8}$-$Ir_{0.2}$ tip. The brightness in the images does not correspond to the height of the

(a)

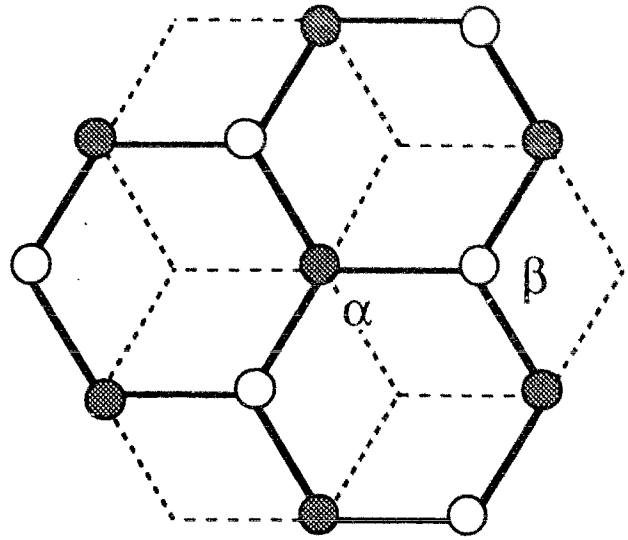

(b)

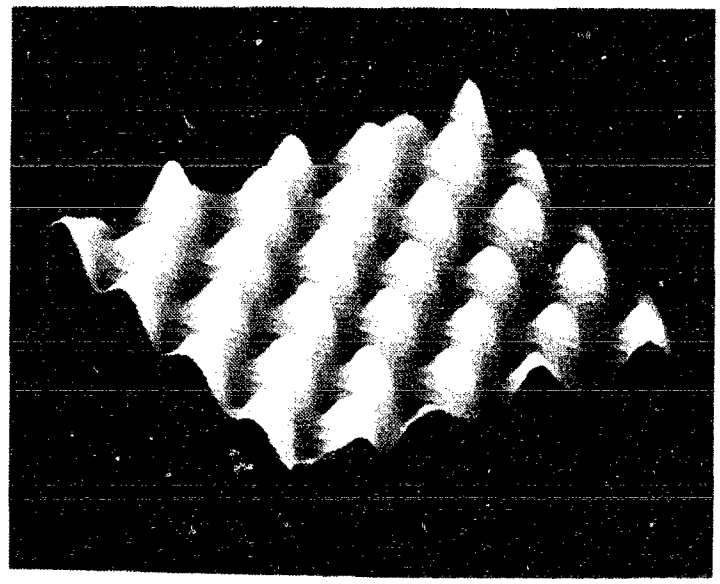

Fig.2-3: (a) Graphite *AB* stacking structure with α- and β- type carbon-atom sites in 2D perspectives. The surface graphite layer is indicated with solid hexagons and the nearest subsurface graphite layer with dashed hexagons.
(b)Individual β- type atoms spaced 2.45Å apart are resolved on a graphite image (3D perspective) obtained with the STM in constant-height mode.

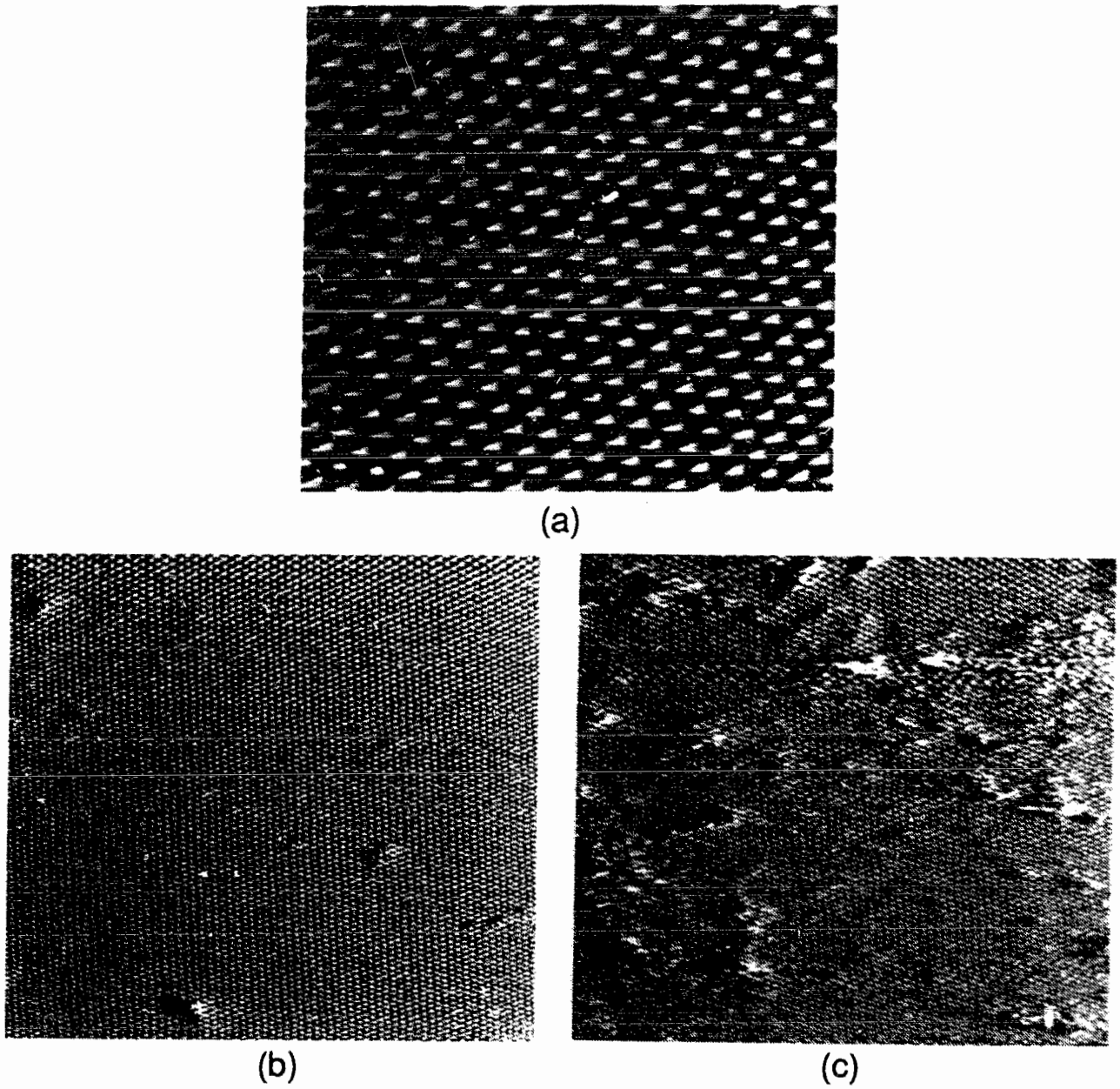

Fig.2-4: Current images (~36Åx50Å and ~150Åx210Å) of three different surface locations of a graphite, obtained with a positive tip bias of ~10mV, an average current of 4.5nA for (a) and of 2nA for (b) and (c).

surface, but to the variation of the tunneling current at a fixed tip height. Fig.2-4(a) shows the typical graphite image consisting of an array of bright spots with the expected hexagonal structure and only three bright spots per carbon hexagon. The image was taken at a positive tip bias of 8.4 mV and an average tunneling current of 4 nA. Two larger area atomic-resolution images obtained later are shown in Fig.2-4(b) and (c), taken at about the same tip bias and an average current of 2 nA. The deviation from the ideal hexagonal pattern that is apparent in the figure results from the different x and y scales of the screen from which the photograph was taken.

From the images, we see that the surface is not that perfect when viewed in relatively larger scale, there are some defects as small in size as that of a few atoms. Upon closer examination of Fig.2-4(c), one notices that there is a little distortion along the y direction that appears in the form of zigzag rows. Since the scan frequency on the x direction is much larger than that on the y direction of the computer screen, and faster scan will help to separate the signal from low frequency noise, one finds it relatively easier to get image distortions along the y direction.

Four more graphite images shown in Fig.2-5 demonstrate tip induced artifacts and the subtlety of interpreting atomic-resolution STM images. In the image shown in Fig.2-5(a), the bright spots appear triangular in space; in Fig.2-5(b), a honeycomb array appears in the image; in Fig.2-5(c), the image shows a loss of three-fold symmetry because the bright spots are stretched in rows; in Fig.2-5(d), the bright spots appear round in shape. Mizes *et al.*[27] have shown that two single-atom tips can cause effects that account for the image variations shown. The STM image is a superposition of two single-atom-tip images, the second shifted by the relative separation of the two tip atoms. Since each image is dominated by only three independent Fourier components, the superposition would result in the 3rd set of three Fourier components of differing amplitudes and phases. Different

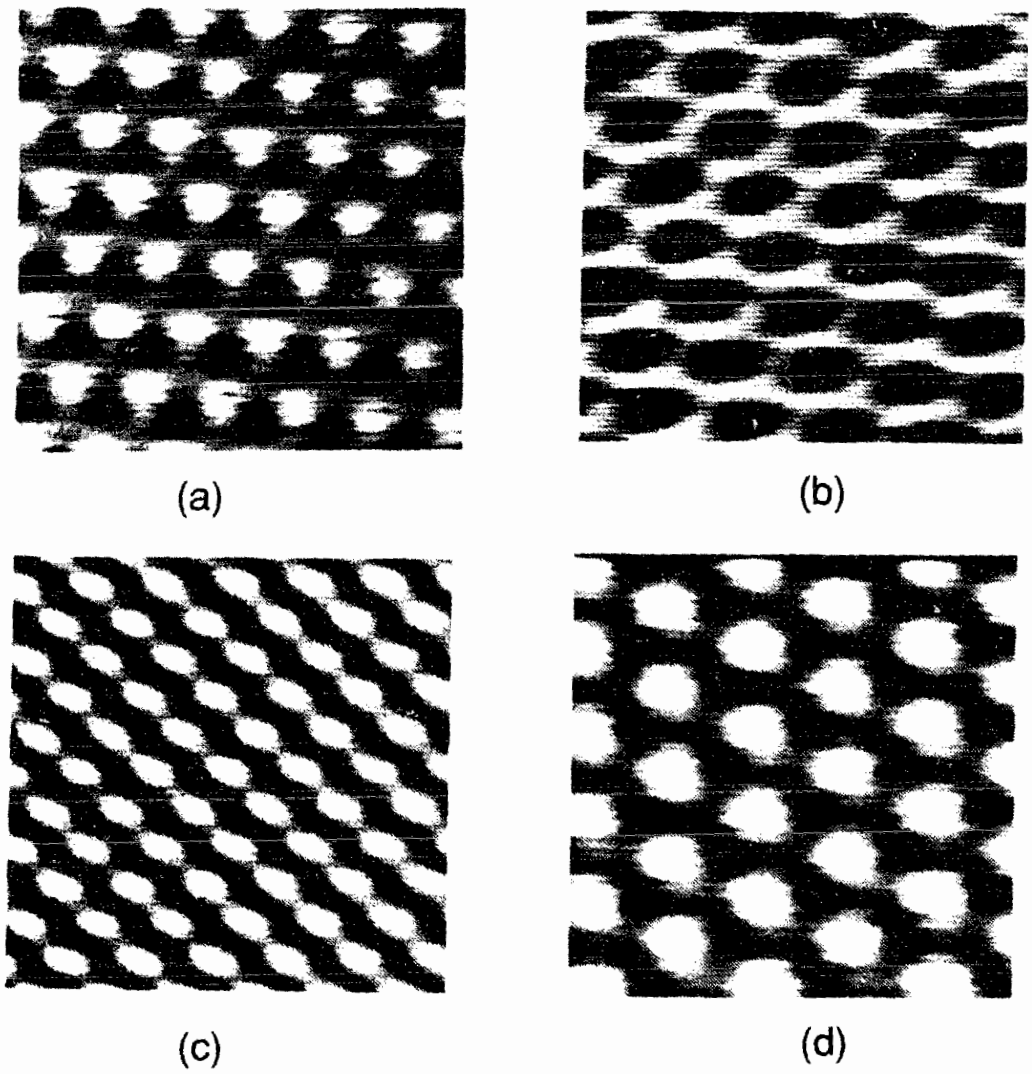

Fig.2-5: Four different types of graphite images obtained with the STM. (a)The bright spots appear triangular in space. (b)A honeycomb array appears in the image. (c)The image shows a loss of three-fold symmetry. (d)The bright spots appear round in shape.

combinations the final amplitudes and phases of the same Fourier components will give rise to various image patterns shown in Fig.2-5. Since the tip structure is unknown and its properties are also involved in the tunneling process, it is hard to determine experimentally which image is the principal image obtained with a single atom tip. Images shown in Fig.2-5(b) and (c) can be ruled out because of the known symmetry of the crystal lattice, but the remaining two are the candidates for a principal image. Nevertheless, *the unit cell periodicity of the crystal is always visible* in all of the four images.

The last two images, shown in Fig.2-6, were obtained from a graphite surface being scanned in perpendicular directions to demonstrate the rotation functions of the control circuits. We see the defect (about 15 Å x 30 Å in size) has changed in orientation by 90 degrees from one image to another, as a result of rotation of imaging. The brightening effect shown in Fig.2-6 is an electronic artifact, as one notices that the brightness is always associated with those horizontal scan lines over the defect. Such an artifact is related to the way in which the data are acquired. Because in constant-height mode the time constant (τ) of the feedback circuit is very large, and with fast scan operation the circuit responds insensitively to the tip-surface gap variation related with the surface unit cell periodicity, but the feedback still functions in terms of keeping the *average current constant*. The tunneling current is recorded to profile surface atomic structure in this operation mode. When we deal with a perfect surface there is no electronic artifact due to the feedback function. However, when we image a surface with a larger defect like the one shown in Fig.2-6, the strong current depression over the defect leads to a compensating current growth (the brightness) near the defect due to the feedback function in order to reach constant average current.

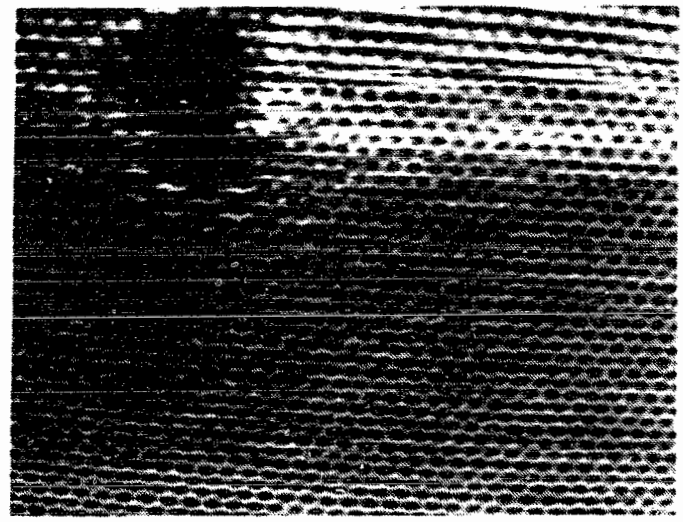

(a)

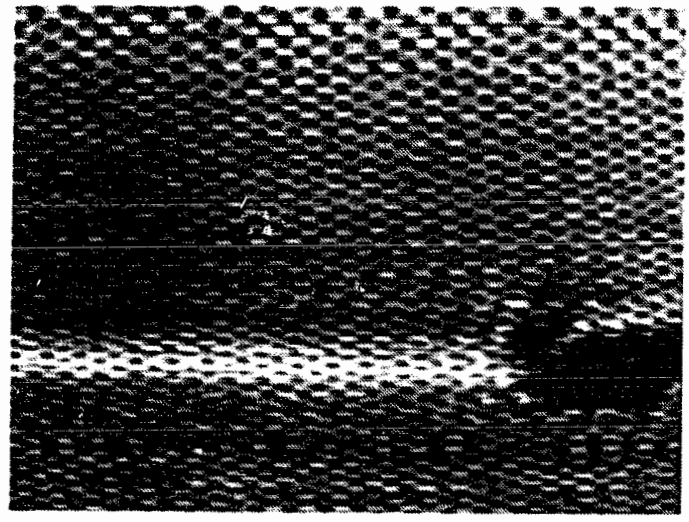

(b)

Fig.2-6: Constant-height mode images obtained from a graphite surface being scanned in perpendicular directions demonstrate the rotation function in the control circuits.

Chapter 3

Theory of STM imaging of intercalated graphite

Graphite has been a prototype material for STM studies, since it is very easy to get large atomically flat surface that exhibits a perfect lattice over thousands of angstroms. As we have seen in Chapter 2, there are two anomalous features in a graphite image–a large corrugation over the center of each carbon hexagon and a substantial asymmetry of neighboring carbon sites, which differ drastically from the surface topography. Also, neither of them can be understood within a simplistic picture that the STM images the total electron charge density of the surface which shows only modest variations across the basal plane.[26, 31] The first anomaly, as shown by Tersoff,[25] is due to the unusual electronic structure of a single graphite layer, in which the Fermi surface collapses to a point at the corner of the surface Brillouin zone. Because the STM probes the local electron density of states at the Fermi level, the small Fermi surface of graphite results in a node in the wave functions of just a few electron states over the center of each hexagon. Others found that elastic interactions between the STM tip and the surface could strongly enhance the corrugation amplitude,[41] especially in the case of contaminated surfaces.[42] The second anomaly, as demonstrated by Batra *et al* [26] and Tomanek and co-workers[39, 40] is primarily a property of the bulk material, attributed to the *AB* stacking of the graphite.

The electronic properties of graphite can be modified systematically by intercalating various guest species into the galleries between the carbon layers. Since intercalation always occurs with a charge transfer between the intercalate and the graphite, the intercalate is defined as a donor or an acceptor according to the direction of the Fermi level

displacement. These structure and additional charge modifications will influence the energy bands and the Fermi surface at the sample surface, and should be reflected in the electron tunneling process. While the physics of graphite intercalation compounds (GIC's) has attracted a great deal of attention in recent years,[43, 44] the surface properties of these compounds remain largely unexplored. The STM should be an excellent probe for these surfaces.

In this Chapter we present our theory of the STM images of graphite and GIC surfaces, which is applicable to both donor and acceptor intercalate species and to staged structures.[45, 46] We show that the corrugation amplitude and the carbon site asymmetry are sensitive to the charge transfer between the guest and host, to the distribution of the transferred charge among the host layers close to the surface, and to the near-surface band structure. Based on this, it should be possible to use the STM to map out the pattern of stage domains at a GIC surface. Even in the bulk case, there are important unanswered questions about the domain structure and electronic properties of GIC's,[43, 44] which makes such surface studies all the more interesting. A surprising prediction of our theory is that in many cases there should be *no* carbon atom asymmetry in the STM image even when the usual AB stacking of the graphite layers occurs at the GIC surface, and that the asymmetry should switch on *discontinuously* with decreasing charge transfer. We also predict that donor GIC's should have stronger carbon site asymmetries than acceptor GIC's with the same absolute value of the charge transfer per carbon atom. We present a possible explanation of the remarkable absence of atomic-scale features in the STM images of BiCs-graphite reported by Gauthier *et al* .[47] The absence of carbon-site asymmetry and the reduced corrugation amplitude predicted by the model for the STM images of $SbCl_5$-graphite have recently been supported by Biensan *et al* in their experiments on a similar charge transfer coefficient GIC, $CrCl_3$-graphite.[48]

We briefly summarize the structure of graphite intercalation compounds in **3.1**. Our theoretical model is described and analyzed in **3.2**. The results are presented in **3.3**. Finally, we outline our conclusions in **3.4**.

3.1 Graphite intercalation compound (GIC) structure

When a layered host material such as graphite is intercalated with a guest species, the guest atoms fill some of the galleries between the host layers, leaving others empty. The new ordered structure has a period consisting of a guest layer followed by n graphite host layers. This is called a stage n compound.

The characteristic structure of a GIC is represented in Fig.3-1 which shows a slice through the crystal perpendicular to the host layers. Fig.3-1 shows a stage 4 compound with every 4^{th} gallery occupied by the guest, but the crystal is divided into Daumas-Hérold domains with different galleries being occupied by the guest in adjacent domains.[49] In this Chapter we will discuss surfaces such as the top surface in Fig.3-1, where the number m of graphite layers covering the guest layer closest to the surface depends on the particular domain involved. These m surface graphite layers are very different from the ordinary pristine graphite. It is known that the formation of GIC's is accompanied by charge transfer and screening effects. The electrons (holes) which are transferred to the graphite from the donor (acceptor) guest screen the charged guest layers, and their concentration is highest in the graphite layers closest to the guest. Because of the unusual band structure of the graphite, the screening is nonexponential, with the screening charge density and the associated potential decaying roughly as a power of the distance from the closest guest layer.[50] Consequently, in the surface region, there are electrostatic potential differences between the m graphite layers, which should be included in the Hamiltonian of the system.

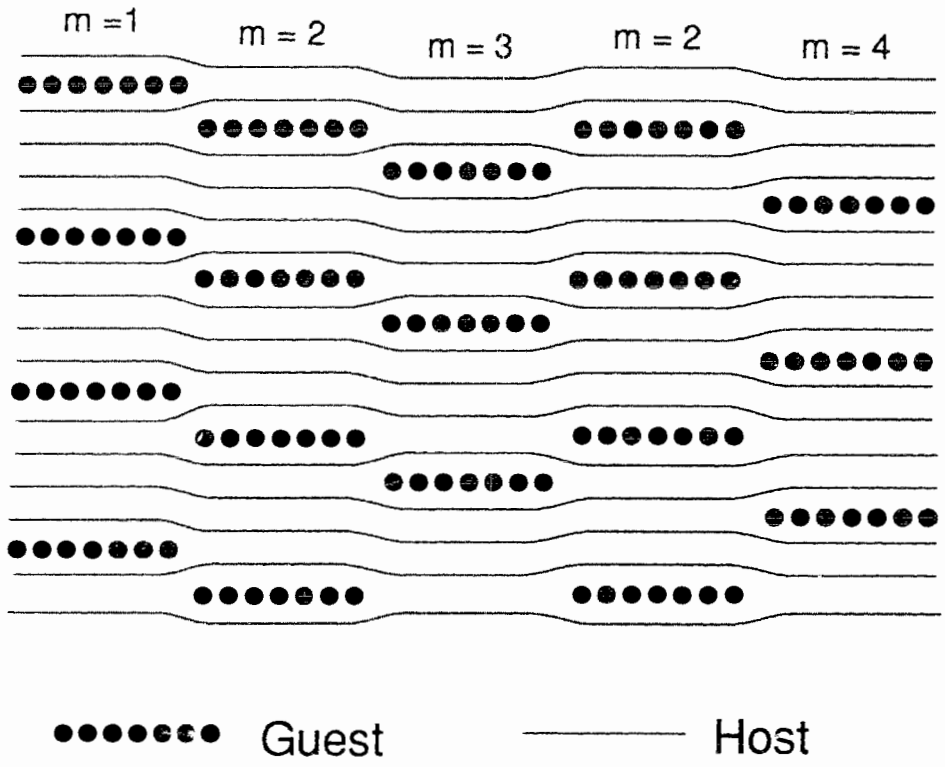

Fig.3-1: Schematic representation of stage order and domain structure in a stage-4 GIC.

In addition, the Fermi level of the system is shifted from that of pristine graphite because of the transferred charge. Clearly , the different (m) surface domains have different potential distributions, energy bands and Fermi surfaces, and, therefore, STM images which can differ markedly from each other and from that of pristine graphite.

In our model we assume that the stacking sequence of graphite layers, *where it is not interrupted by the presence of a guest layer*, is still the usual graphite *ABAB* stacking sequence. This is known to be correct in the bulk case for most staged GIC's.[43, 44] In this stacking there are two kinds of carbon atom sites: α sites which are adjacent to carbon atom sites in the neighboring graphite layer(s), and β sites which are adjacent to the (vacant) centers of the carbon hexagons in the neighboring layers, as shown in Fig.3-2(a) and (b).

Experimentally, surfaces such as those shown in Fig.3-1 can be prepared by cleaving a GIC sample, and at least in the case of $SbCl_5$-graphite, the surface domain structure appears to be sufficiently stable to be studied in vacuum, according to the high-resolution scanning ion microprobe work of Levi-Setti *et al.*[51] Laguës, D.Marchand and C.Frétigny[52] have suggested that some guest species may tend to segregate towards the surface leading to an increased guest concentration in the first sub-surface gallery, while the opposite effect may occur for other guests. Our theory is applicable also to such systems, as well as to graphite mono-layers and multi-layers on clean metal surfaces.

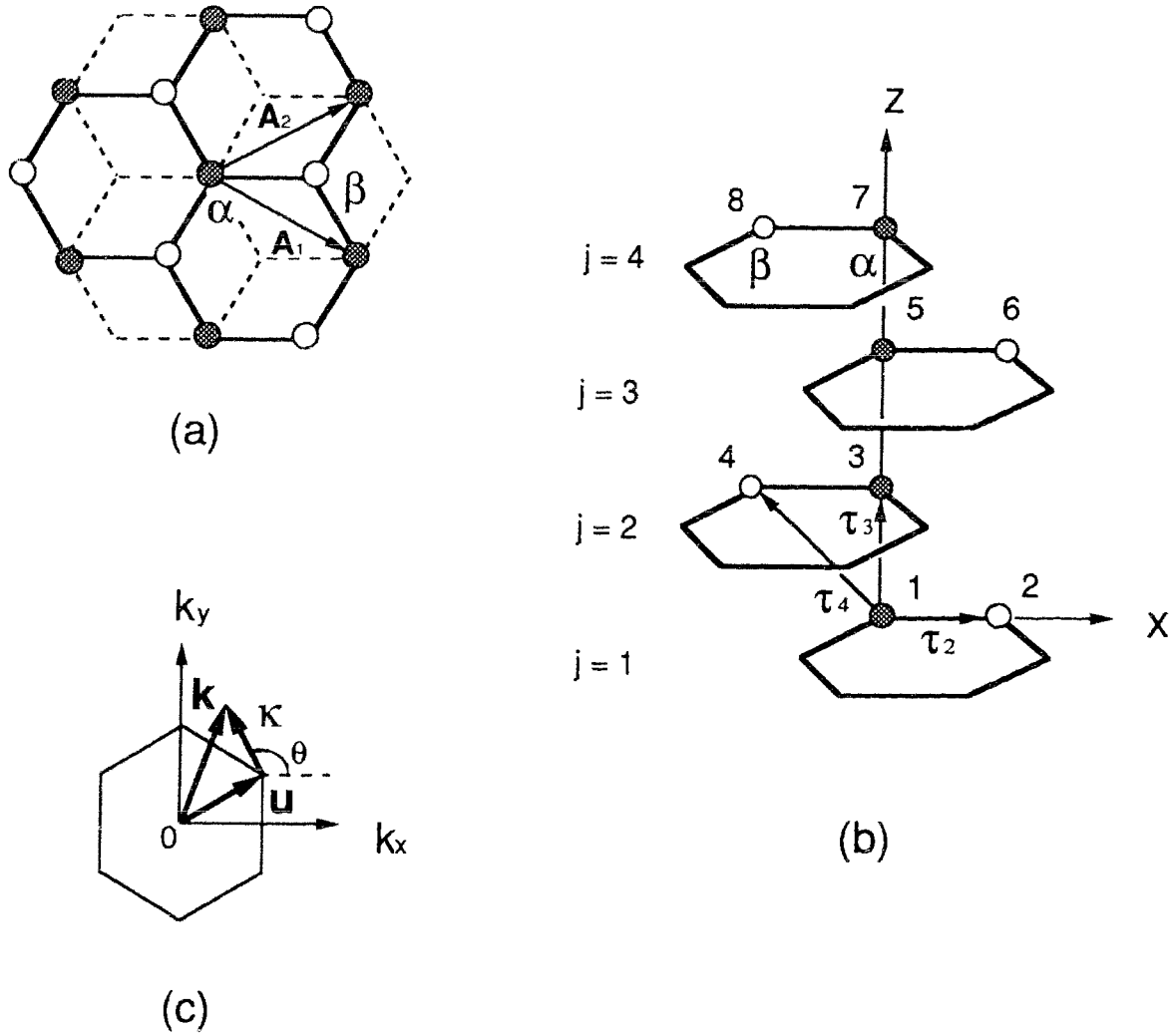

Fig.3-2: Graphite *AB* stacking structure with α and β type carbon-atom sites in (a)2D and (b)3D perspectives where $|\tau_2| = b = 1.42$Å and $|\tau_3| = c_0 = 3.35$Å, and (c) the hexagonal 2D Brillouin Zone where wavevector $\mathbf{k} = \mathbf{u} + \kappa$ and $\mathbf{u} = (2\pi/3b, 2\pi/3^{3/2}b)$.

3.2 The theoretical model

Our starting point is the result of Tersoff and Hamann,[24] that at low bias voltages, for a simple *s*-wave model of the STM tip, the tunneling current is proportional to the local density of states at the Fermi energy E_F which is given by

$$\rho(\mathbf{r},E_F) = \sum_{\mathbf{k}n} |\Psi_{\mathbf{k}n}(\mathbf{r})|^2 \delta(E_{\mathbf{k}n}-E_F)$$

where $\mathbf{r}$ is the center of curvature of the tip and $\Psi_{\mathbf{k}n}(\mathbf{r})$ and $E_{\mathbf{k}n}$ are the electron eigenstates and energy eigenvalues of the sample. The STM image in the constant-current mode represents a contour of constant $\rho(\mathbf{r},E_F)$.

The whole idea of the theoretical considerations is presented in the block diagram shown in Fig.3-3. To calculate $\rho(\mathbf{r},E_F)$ for the STM image of a surface domain, we structure the model Hamiltonian of the system so as to include the effects of transferred charge distribution (which depends on m and intercalate charge transfer value f), and use a modification of the tight-binding model of Blinowski and co-workers[53, 54] to find the wavefunctions $\Psi_{\mathbf{k}n}(\mathbf{r})$ of the states near the Fermi energy.

The tight-binding model of Blinowski and co-workers has been used successfully to describe the bulk electronic properties of staged GIC's for the larger guest species. Compared with their model, our tight-binding model uses the same basis states $u_{i\mathbf{k}}(\mathbf{r})$ (built of carbon atomic $2p_z$ orbitals $\varphi_z(\mathbf{r})$) for the wavefunction $\Psi_{\mathbf{k}n}(\mathbf{r})$ of the system of m graphite layers, but a different form of the Hamiltonian. The m graphite layers in their model are in the bulk of GIC, and they treat the charge-distribution-related Hamiltonian matrix elements phenomenologically. Our interest is in the surface region, and we calculate the charge distribution and hence find its effects on the Hamiltonian matrix elements by

Theoretical model: a modification of tight-binding model of Blinowski *et al*

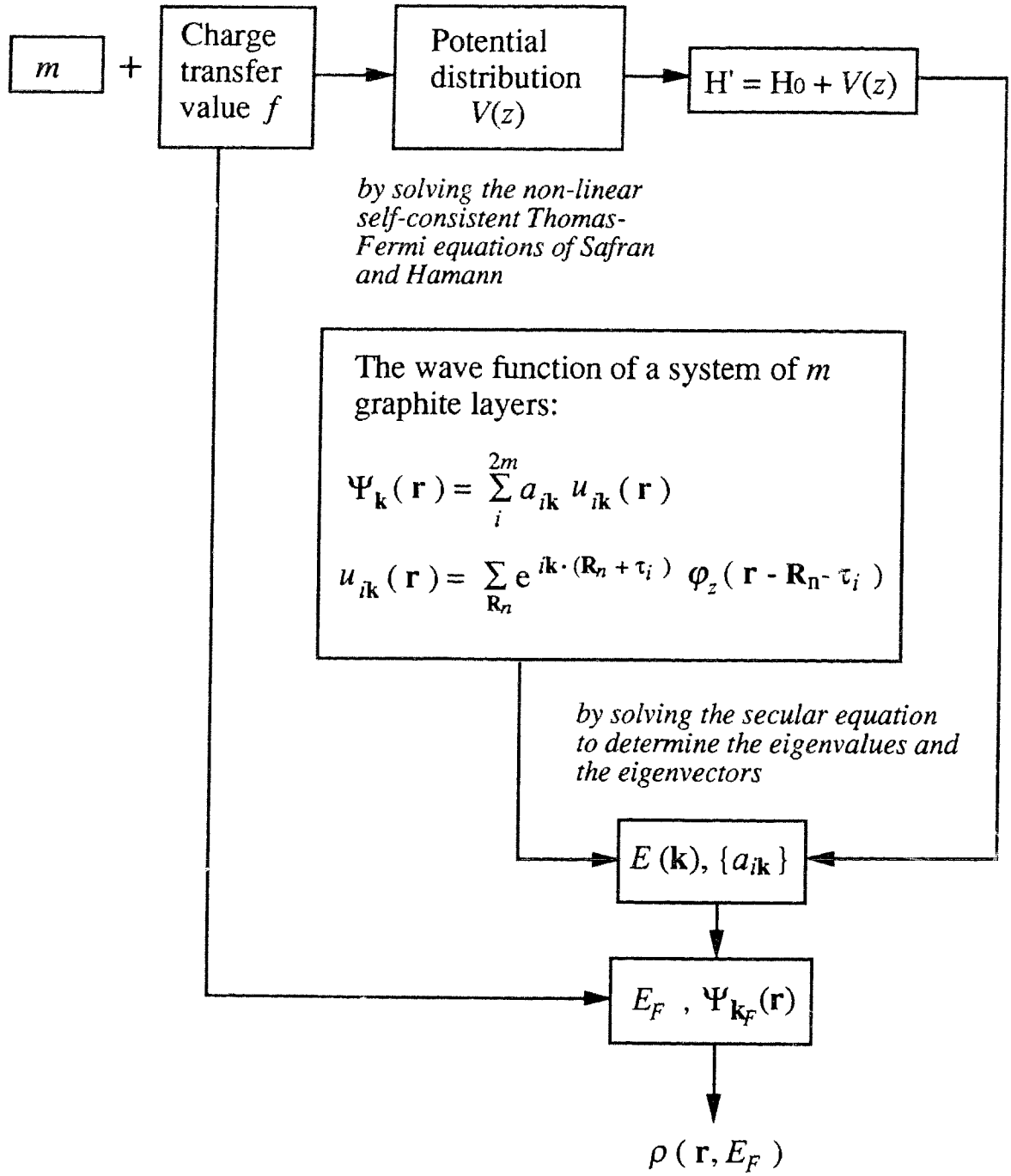

Fig.3-3.

numerically solving the nonlinear self-consistent Thomas-Fermi equations of Safran and Hamann.[50]

We note that simple tight-binding models are known to be capable of describing the main features of the STM image of pristine graphite.[40] Our calculations reproduce the results of the published first principles calculations of the STM images of multilayer slabs of pristine graphite[26] as well as of graphite monolayers[25] with reasonable accuracy. For example, we find an asymmetry of ~0.6-0.7Å between the α and β sites of a four layer slab of pristine graphite in constant current mode, which is close to the 0.5Å found by Batra *et al* [26] under similar conditions using a self-consistent pseudopotential method.

A. Potential and charge distribution

The Safran-Hamann Thomas-Fermi theory has, in the past, been found adequate for the description of GIC energetics of staging, a phenomenon which is very sensitive to the distribution of the transferred charge.[43, 44, 50, 55, 56] Safran and Hamann derived the nonlinear self-consistent Thomas-Fermi equations and solved them analytically to give the *bulk* potential distribution in GIC's. We calculate the potential distribution of a *surface domain* by solving the equations numerically for a semi-infinite GIC with appropriate surface boundary conditions.

Three important approximations are involved in the derivation of the nonlinear self-consistent Thomas-Fermi equations of Safran and Hamann:[50] (a) the transferred charge is homogeneously distributed in the layers perpendicular to the *c* axis, i.e. both the graphite and the intercalant layers are treated as charged sheets with an inhomogeneous potential along the *c* axis only;[57] (b) the effects of the small *c* axis band dispersion of the graphite energy bands are neglected, so that the energy bands can be described by a two-

dimensional model;[58] (c) a continuum approximation to represent the distribution between the intercalant layers is adopted.[58]

For donor guests, the Thomas-Fermi energy of the system is then given by[50]

$$E(n_e) = \frac{1}{2}\int eV(z)[n_i(z) - n_e(z)]dz \quad + \int t(n_e)n_e(z)dz \quad , \tag{1}$$

where $n_i(z)$ and $n_e(z)$ are the intercalate-ion and electron carrier density in the c axis direction, respectively; $t(n_e)$ is the total band energy per electron due to the in-plane (2D) graphite band dispersion; $V(z)$ is the potential distribution, and the electron potential energy is $(-e)V(z)$.

The first term in Eq.(1) represents the electrostatic energy, with $V(z)$ satisfying

$$\frac{d^2V(z)}{dz^2} = -\frac{4\pi e}{\epsilon}[n_i(z) - n_e(z)] \, , \tag{2}$$

where $\epsilon \cong 5.4$ is the c-axis dielectric constant[50]of graphite layers.

The second term in Eq.(1) is the band kinetic energy of the electron carriers. The graphite band dispersion is given approximately by $\varepsilon(\kappa)=(3/2)\gamma_0 b|\kappa|$,[53, 54] the energy being measured near the location of the Fermi level of pristine graphite. Here b=1.42Å is the in-plane nearest neighbor distance of graphite, κ is the 2D wavevector measured from the corner of the hexagonal 2D Brillouin Zone(see Fig.3-2(c)), $\gamma_0 = 2.51eV$[59] is the tight-binding Hamiltonian matrix element associated with in-plane nearest neighbor coupling.[53, 54] The total band energy per electron $t(n_e)$ is then

$$t(n_e) = \frac{2}{3}t_0 n_e^{1/2} \tag{3}$$

where $t_0 = (3/2)\gamma_0 b(\pi c_0)^{1/2}$, and $c_0 = 3.35$ Å is the interlayer spacing of graphite.

Based on the Thomas-Fermi approximation, if $t(n_e)$ and $(-e)V(z)$ have their zeros defined by the Fermi level of pristine graphite, the minimization of Eq.(1) with respect to $n_e(z)$ yields a local relation between charge and electrostatic potential [50]

$$eV(z) = t_0 n_e^{1/2}(z) \ , \tag{4}$$

and one can rewrite Eq.(2) and (4) as

$$\frac{d^2\phi(\xi)}{d\xi^2} = \tilde{n}_e(\xi) - \tilde{n}_i(\xi) \ , \tag{5}$$

$$\phi^2(\xi) = \tilde{n}_e(\xi) \ , \tag{6}$$

where

$$\phi(z) = eV(z) \ , \tag{7}$$

$$\tilde{n}_e(\xi) = t_0^2 n_e(z) \ , \quad \tilde{n}_i(\xi) = t_0^2 n_i(z) \ , \tag{8}$$

and

$$\xi = (e/t_0)(4\pi/\varepsilon)^{1/2} z \ . \tag{9}$$

In the region of graphite layers, $n_i(z) = 0$, we combine Eq.(5) and (6) to yield

$$\frac{d^2\phi(\xi)}{d\xi^2} = \phi^2(\xi) \ . \tag{10}$$

Now, let us consider the boundary conditions at the intercalate layers. We define σ, the areal charge density on the intercalate layers, as

$$\sigma = \frac{f}{q/2}\frac{e}{\Omega}, \tag{11}$$

where f is the number of electrons received or donated per intercalate unit; qxn is the number of carbon atoms per intercalate unit for stage n GIC, which is related with the stoichiometry of GIC's; $\Omega = 3b^2 sin60^\circ$ is the area of the unit cell of 2D graphite. Thus, $2f/q$ is the number of electrons transferred per 2D graphite unit cell on the intercalate layers. Therefore, at the Lth intercalant layer, the boundary conditions are given by[50]

$$\phi(\xi_L^+) = \phi(\xi_L^-), \tag{12}$$

$$\phi'(\xi_L^+) - \phi'(\xi_L^-) = -p, \tag{13}$$

where $p = 2\sigma t_0(\pi/\varepsilon)^{1/2}$, ξ_L^+ and ξ_L^- are locations just above and below the Lth intercalant layer, respectively (see Fig.3-4).

The numerical results presented here are for a model in which the intercalate layers are represented by charged sheets of infinitesimal thickness so that electro-static boundary conditions at the graphite-intercalate interfaces take the simple form (Eq.(12) and (13)). We have also carried out more detailed calculations in which finite intercalate thickness typical of various GIC's are assumed and found the effect on the calculated STM images to be very small (<0.01 a.u.), justifying the above idealization.

In order to solve the potential distribution of a surface domain (m graphite layers), we need to give appropriate surface boundary conditions. Since there is no free areal charge density on the GIC surface, and the GIC should be neutral as a whole, for a semi-infinite GIC, we can take the electric field outside the GIC to be zero, so that the surface boundary condition is

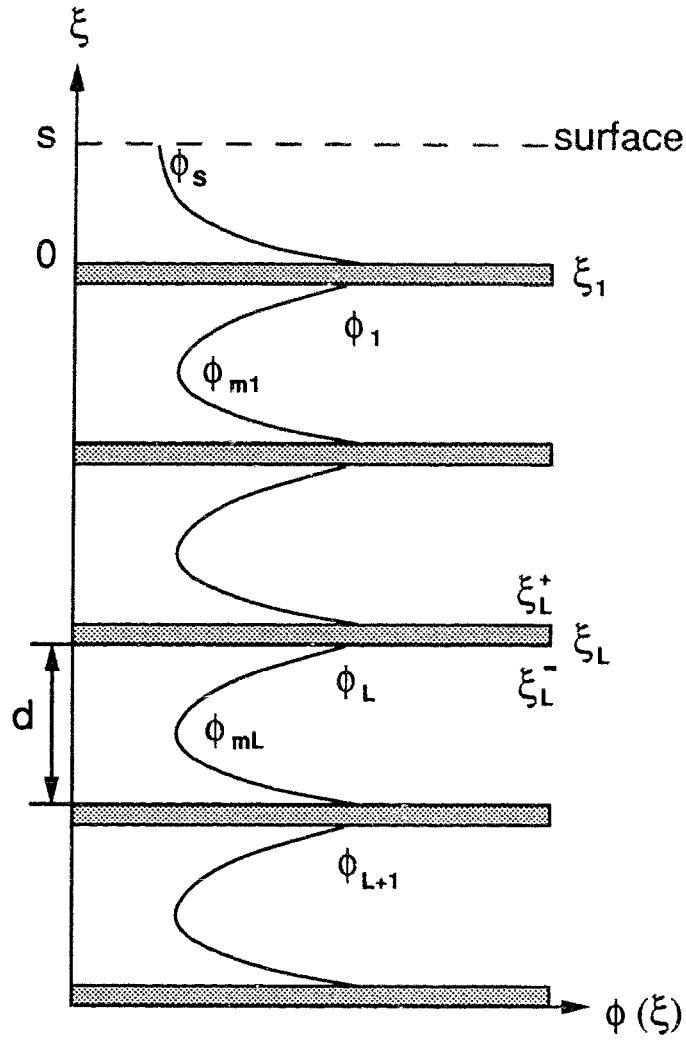

Fig.3-4: Schematic representation of the charge transfer associated potential energy distribution between intercalant layers and between the surface and the 1st subsurface intercalant layer.

$$\phi_s' = 0 \,. \tag{14}$$

We multiply Eq.(10) by $2\phi'(\xi)$ and integrate over the near surface region ($o \leq \xi \leq s$, see Fig.3-4) with the consideration of the surface boundary conditions to obtain

$$\phi'(\xi) = -\{\frac{2}{3}[\phi^3(\xi) - \phi_s^3]\}^{1/2} \,. \tag{15}$$

Similarly, in the region $\xi_L^- \leq \xi \leq \xi_{L+1}^+$

$$\phi'(\xi) = \pm\{\frac{2}{3}[\phi^3(\xi) - \phi_m^3]\}^{1/2} \,, \tag{16}$$

where ϕ_m is the minimum value of the region.

From (12), (13) and the above Eq.(16), we obtain

$$[\frac{2}{3}(\phi_{L+1}^3 - \phi_{mL}^3)]^{1/2} + [\frac{2}{3}(\phi_{L+1}^3 - \phi_{mL+1}^3)]^{1/2} = -p \,. \tag{17}$$

By integrating (15), we find

$$s = (\frac{3}{2})^{1/2} \int_{\phi_s}^{\phi_1} \frac{d\phi}{(\phi^3 - \phi_s^3)^{1/2}} \,, \tag{18}$$

where s is the distance from the first intercalant layer to the surface. Similarly, from (16)

$$d = (\frac{3}{2})^{1/2} \{ \int_{\phi_{mL}}^{\phi_L} \frac{d\phi}{(\phi^3 - \phi_{mL}^3)^{1/2}} + \int_{\phi_{mL}}^{\phi_{L+1}} \frac{d\phi}{(\phi^3 - \phi_{mL}^3)^{1/2}} \} \quad , \tag{19}$$

where $d = |\xi_L^- - \xi_{L+1}^+|$ is the distance (corresponding to nc_O in z-space) between two neighboring intercalant layers.

Defining

$$f(x) = (\frac{3}{2})^{1/2} \int_x^1 \frac{dy}{[y\ (1 - y^3)]^{1/2}} \quad , \tag{20}$$

we rewrite (18) and (19) as

$$(\phi_s)^{1/2}\, s = f(\phi_s / \phi_1) \, , \tag{21}$$

$$f(\phi_{mL} / \phi_{L+1}) = (\phi_{mL})^{1/2} d - f(\phi_{mL} / \phi_L) \, , \tag{22}$$

and (17) as

$$\phi_{mL+1} = \{ \phi_{L+1}^3 - [\, (\frac{3}{2})^{1/2} p - (\phi_{L+1}^3 - \phi_{mL}^3)^{1/2} \,]^2 \}^{1/3} \, . \tag{23}$$

Thus, (21),(22) and (23) are our iteration equations. We try a value of ϕ_S, and obtain ϕ_1 from (21), then use (23) and (22) repeatedly to find ϕ_{m1}, ϕ_2, ϕ_{m2}, ϕ_3... etc. The iteration of ϕ_{mL}(or ϕ_L) should tend gradually towards the bulk solution ϕ_{mb} (ϕ_b), otherwise the initial value ϕ_s should be adjusted until a proper ϕ_s is found. ϕ_{mb} and ϕ_b are determined by numerically solving the following two equations

$$2\left[\frac{2}{3}(\phi_b^3 - \phi_{mb}^3)\right]^{1/2} = p \ , \tag{24}$$

$$d = 2\left(\frac{3}{2}\right)^{1/2} \int_{\phi_{mb}}^{\phi_b} \frac{d\phi}{(\phi^3 - \phi_{mb}^3)^{1/2}} \ . \tag{25}$$

Having found ϕ_s, we use the Runge-Kutta numerical method for solving the initial value problem for the differential equation (15) to find $\phi(\xi)$ in the surface region ($0 \le \xi \le s$, or $0 \le z \le mc_0$), and hence the potential distribution $V(z)$ among the m surface graphite layers.

The above treatment can be easily extended to the case of acceptor GIC's. The form of $V(z)$ obtained is the same as for donors except for sign.

Since we treat the intercalant layers as uniformly charged sheets, the model Hamiltonian (see below) does not reflect superlattice effects (due to the in-plane intercalate periodicity being different from that of the graphite). This simplification appears to be a reasonable one since A.Selloni and co-workers,[60] who carried out detailed psuedopotential calculations for the case of stage 1 LiC_6, found the superlattice effects on the STM corrugation amplitude to be very small. Note however that some recent experiments carried out by Kelty and Lieber[61] in an argon atmosphere suggest that in some stage 1 alkali-metal GIC's such superlattice effects may be observable.

B. Tight-binding *H* matrix

In our tight-binding model Hamiltonian of the graphite layers we follow Blinowski and co-workers[53, 54] by including only the nearest neighbor in-plane and interlayer

hopping terms. All electronic hopping terms between host layers separated by a guest layer are ignored. For a single graphite layer, as there are two atoms per unit cell, the wavefunction with wave vector $\mathbf{k}$ is constructed using two tight-binding basis functions $u_{i\mathbf{k}}(\mathbf{r})$ built of atomic $2P_z$ orbitals $\varphi_z(\mathbf{r})$. For a system of m graphite layers, the wavefunction $\Psi_{\mathbf{k}}$ is then a linear combination of $2m$ tight-binding basis functions[53, 54]

$$u_{i\mathbf{k}}(\mathbf{r}) = C \sum_{\mathbf{R}n} \exp[i\mathbf{k}\cdot(\mathbf{R}_n + \tau_i)]\varphi_z(\mathbf{r} - \mathbf{R}_n - \tau_i) , \tag{26}$$

$$\Psi_{\mathbf{k}}(\mathbf{r}) = \sum_i a_{i\mathbf{k}} u_{i\mathbf{k}}(\mathbf{r}) \qquad (i=1,2,\ldots\ 2m), \tag{27}$$

where C is the normalizing factor , $\mathbf{k}$ is the 2D wavevector, and $\mathbf{R}_n = n_1\mathbf{A}_1 + n_2\mathbf{A}_2$ is the 2D lattice vector formed from primitive translation vectors $\mathbf{A}_1$ and $\mathbf{A}_2$. τ_{2j-1} and τ_{2j} (j=1,2,...m) are the shortest vectors from the origin τ_1=0 (see Fig.3-2) to α and β type atoms, respectively, in the jth graphite layer.

In the basis defined by equation (26) our approximate Hamiltonian for an m =4 surface domain is represented by the following matrix

$$\begin{vmatrix}
H_{11}\pm\Delta_1 & -\gamma_0 g(\mathbf{k}) & \gamma_1 & 0 & 0 & 0 & 0 & 0 \\
-\gamma_0 g^*(\mathbf{k}) & H_{11}\pm\Delta_1 & 0 & 0 & 0 & 0 & 0 & 0 \\
\gamma_1 & 0 & H_{11}\pm\Delta_2 & -\gamma_0 g^*(\mathbf{k}) & \gamma_1 & 0 & 0 & 0 \\
0 & 0 & -\gamma_0 g(\mathbf{k}) & H_{11}\pm\Delta_2 & 0 & 0 & 0 & 0 \\
0 & 0 & \gamma_1 & 0 & H_{11}\pm\Delta_3 & -\gamma_0 g(\mathbf{k}) & \gamma_1 & 0 \\
0 & 0 & 0 & 0 & -\gamma_0 g^*(\mathbf{k}) & H_{11}\pm\Delta_3 & 0 & 0 \\
0 & 0 & 0 & 0 & \gamma_1 & 0 & H_{11}\pm\Delta_4 & -\gamma_0 g^*(\mathbf{k}) \\
0 & 0 & 0 & 0 & 0 & 0 & -\gamma_0 g(\mathbf{k}) & H_{11}\pm\Delta_4
\end{vmatrix} \tag{28}$$

where Δ_j represents the potential energy in graphite layer j, which is determined by averaging the self-consistent screened potential energy $eV(z)$ over the range of c_0 occupied by the jth layer; $g(\mathbf{k})=\exp(i\mathbf{k}*\tau_2)+\exp(i\mathbf{k}*D_3\tau_2)+\exp(i\mathbf{k}*D_3^{-1}\tau_2)$,[53, 54] and D_3 is the operator of the $2\pi/3$ rotation about the c-axis; γ_0 is the resonance integral[53, 54] between the carbon $2P_z$ orbitals of nearest-neighbor α-β atoms within a graphite layer, while γ_1 is that between the orbitals of nearest-neighbor α-α atoms on adjacent graphite layers. We take γ_0=2.51eV and γ_1=0.377eV.[59] The "+" sign is for the case of acceptor guests and "-" sign for the case of donor guests. All matrix elements between two carbon atoms separated by more than the distance c_0 are neglected. Also, all matrix elements between graphite layers separated by a guest layer and between graphite and guest are neglected.

Shifting all energy levels by $H_{11}\pm\Delta_1$, we write the secular equation of the matrix (28) as

$$\begin{vmatrix}
-E & -x & \gamma_1 & 0 & 0 & 0 & 0 & 0 \\
-x^* & -E & 0 & 0 & 0 & 0 & 0 & 0 \\
\gamma_1 & 0 & -(E\pm\delta_{12}) & -x^* & \gamma_1 & 0 & 0 & 0 \\
0 & 0 & -x & -(E\pm\delta_{12}) & 0 & 0 & 0 & 0 \\
0 & 0 & \gamma_1 & 0 & -(E\pm\delta_{13}) & -x & \gamma_1 & 0 \\
0 & 0 & 0 & 0 & -x^* & -(E\pm\delta_{13}) & 0 & 0 \\
0 & 0 & 0 & 0 & \gamma_1 & 0 & -(E\pm\delta_{14}) & -x^* \\
0 & 0 & 0 & 0 & 0 & 0 & -x & -(E\pm\delta_{14})
\end{vmatrix} = 0 \quad (29)$$

where $\delta_{1j}=\Delta_1-\Delta_j$ is the potential energy difference between the first graphite layer and the jth layer, which is always a positive value, and x represents $\gamma_0 g(\mathbf{k})$.

For $m<4$ surface domains, the H matrices are simply the upper-left $2m$x$2m$ parts of the m=4 matrix.

Thus, in our model the presence of the intercalate is felt only through its influence on the site-diagonal Hamiltonian matrix elements δ_{1j} (j=2,...m) and on the total number of electrons present. The former are very sensitive to the charge transfer value $2f/q$ and m, and the latter is ultimately determined by the value $2f/q$.

Using as input the results of the self-consistent Thomas-Fermi calculation of $V(z)$ described in **3.2**.A, we find the matrix elements of the tight-binding Hamiltonian of the m surface graphite layers. We then solve the secular equation (29), determine the energy bands and the Fermi level, and evaluate $\rho(\mathbf{r},E_F)$ using Herman-Skillman tight binding carbon orbitals.[62]

3.3 Calculation results

In Fig.3-5 we show the calculated constant-current STM profiles for a typical acceptor GIC, stage 4 $SbCl_5$-graphite, with stoichiometry $SbCl_5C_{14x4}$ and charge transfer coefficient f=0.31[63] ($2f/q$ =0.31/7). $SbCl_5$-graphite is of particular interest because of the previous experimental observation of the surface domain structure in that system.[51]

The results for a stage 4 alkali-metal donor GIC with stoichiometry MC_{6x4} and f=1 ($2f/q$ =1/3) are shown in Fig.3-6. MC_{6x4} is a donor GIC with a high areal density of transferred charge.

In Figs 3-5 and 3-6, the vertical axis represents the distance from the center of curvature of the tip to the plane containing the carbon nuclei in the surface graphite layer. The horizontal axis stands for the surface coordinate. Curves 1,2,3 and 4 in each figure correspond to m=1,2,3 and 4 graphite layers at the surface covering the top guest layer as

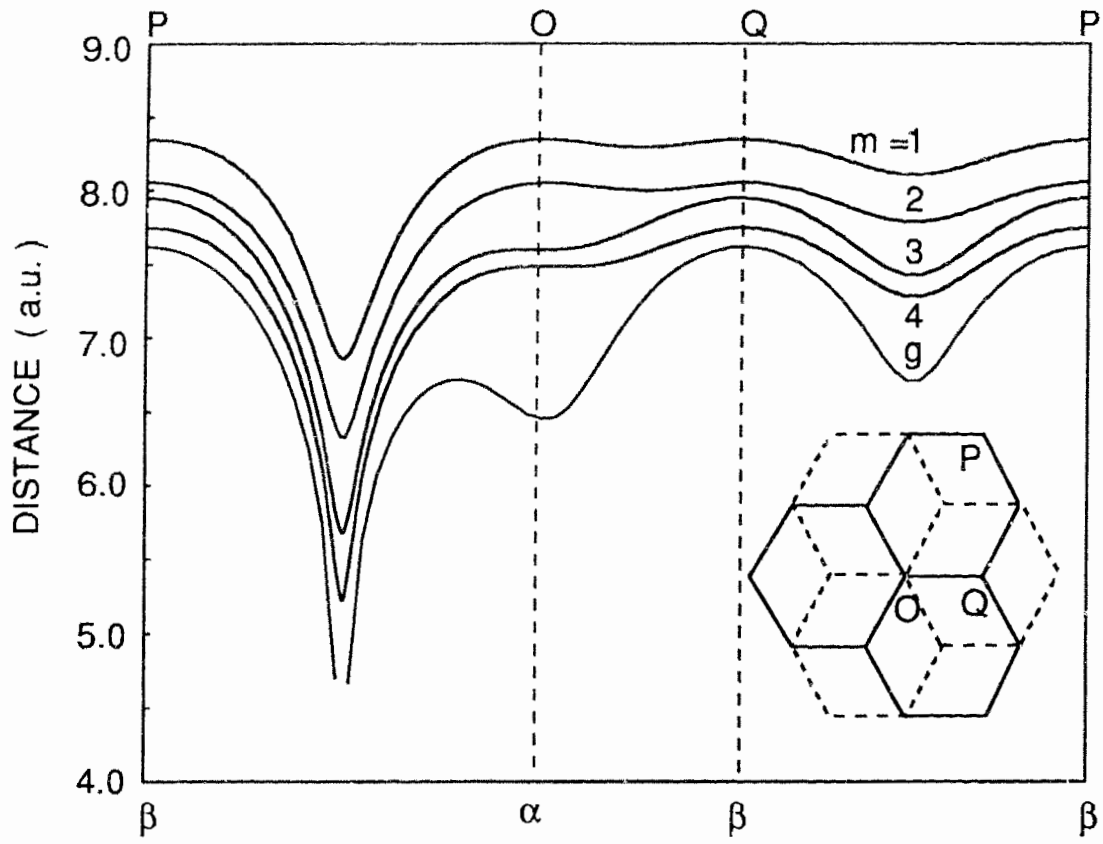

Fig.3-5: Calculated constant-current STM profiles for stage 4 $SbCl_5$-graphite surfaces (curves 1-4 correspond to m=1-4 graphite layers covering the top guest layer as in Fig.3-1), and for a 4-layer slab of pristine graphite (curve g). For curve g the Fermi energy was taken to be 0.0258eV to reflect in a rough way the thermal broadening of the Fermi surface as discussed by Batra *et al.*[26] The scans shown are along PO-OQ-QP in the inset. Inset: Structure of the surface graphite layer (solid hexagons), and (for cases m=2,3,4) of the first subsurface graphite layer (dashed hexagons). No corrections for finite instrumental resolution are included.

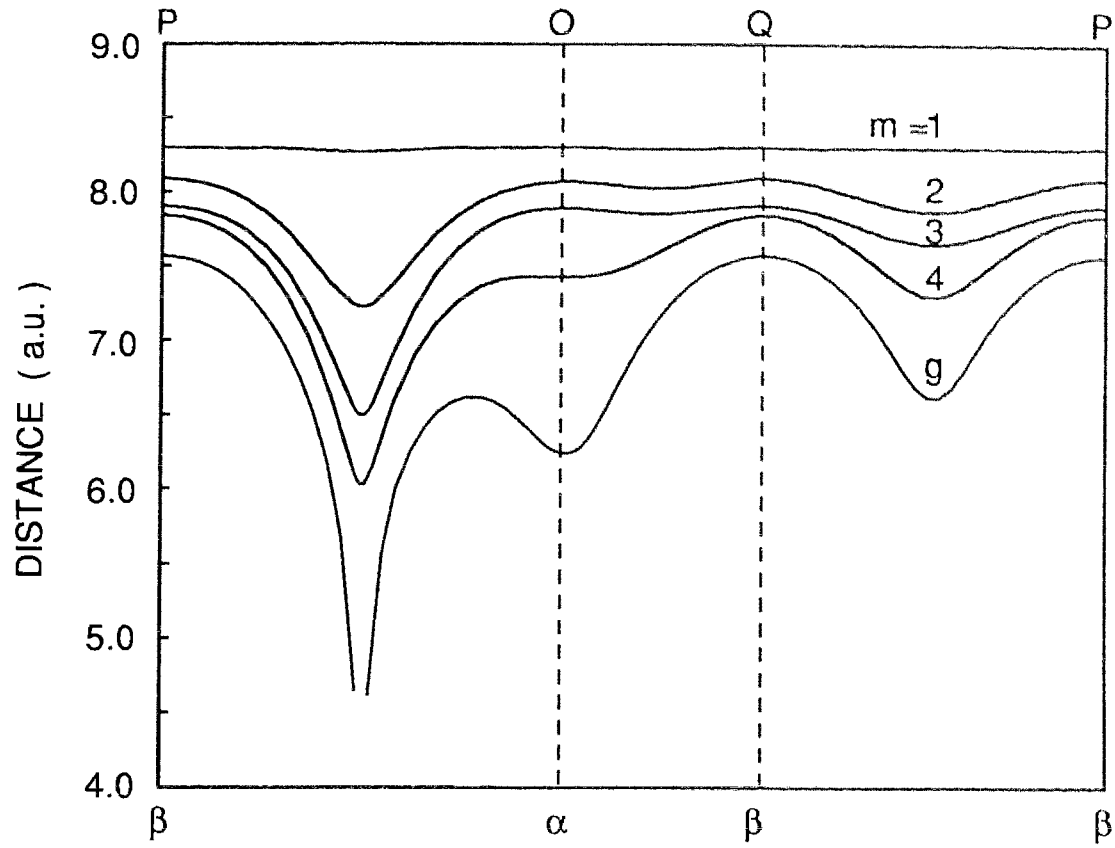

Fig.3-6: Calculated constant-current STM profiles for stage 4 MC_{6x4} alkali metal-graphite surfaces and for pristine graphite. Notation as in Fig.3-5.

in Fig.3-1. Curve *g*, shown for comparison, is the result for a four-layer slab of pristine graphite. The scanning path across the surface is along the line PO-OQ-QP as defined in the inset of Fig.3-5. The points labelled α and β on the horizontal axis mark the locations of the α and β atoms of the surface graphite layer. The five curves in each figure correspond to the same tunneling current. With increasing *m*, the charge density of the top surface layer decreases due to the screening, so that the tip has to be closer the surface in order to keep the same tunneling current. Thus the curves shift to lower distance with increasing *m* in the Figures.

Among alkali metal GIC's only Li-graphite has equilibrium phases with a *bulk* stoichiometry of MC_{6xn} at ambient pressures, the other alkali metals being more dilute. However, guest concentrations as high as MC_6 in the first sub-surface gallery have been reported for the other alkali metals.[52] As shown by Lagues and co-workers,[52, 64, 65] in many graphite intercalation compounds the intercalant composition near the surface is often different from their bulk one: donor compounds exhibit an increased intercalant concentration near the surface, whereas acceptor compounds at equilibrium exhibit two or three pure graphite layers at the surface. While the results shown in Figs.3-5 and 3-6 are for stage 4 compounds, the calculated profiles are very insensitive to the bulk stage, and reflect mainly the number of graphite layers covering the guest layer closest to the surface, and the in-plane density σ or the $2f/q$ of that guest layer. The physical origin of the insensitivity to the bulk stage is that the influence of the 2nd guest layer from the surface is very weak because of the screening effects.[50] *Thus the results presented are also representative of other bulk stages with similar in-plane densities.*

A striking feature of the STM profiles shown in Figs 3-5 and 3-6 is the marked reduction in the strength of the depression at the center of the carbon hexagon upon intercalation. This feature was evidenced recently in the STM imaging of $CrCl_3$-graphite

surface reported by Biensan *et al.*[48] This is due to the fact that the Fermi surface of the graphite is greatly expanded by the carriers transferred from the guest, so that the wave functions of the Fermi electrons no longer have an exact node at the hexagon center, as was anticipated by Tersoff.[25] The increase in the strength of the depression as the number of host layers m between the first guest layer and the surface increases can be understood qualitatively as an effect of the screening of the guest layer by the transferred charge: The further the surface graphite layer is from the guest layer the smaller the free carrier density at the surface and the more the STM image resembles that of pristine graphite. The depression in the profile is weaker for a given value of m in Fig.3-6 than in Fig.3-5 for two reasons: (a) There is a higher density of transferred charge in the former case, and (b) The linear combination coefficients a_{ik} which determine the form of the electron eigenfunctions Ψ_k are different for donor and acceptor guests in such a way that the corrugations are weaker for donors than for acceptors even when $2f/q$ and the shape of the Fermi surface (*but not the Fermi level*) are the same.

The combination of these effects is so strong when there is only one graphite layer covering the alkali metal guest (curve m=1, Fig.3-6) that the STM image is predicted to be nearly featureless on the atomic scale. Thus we are able to explain the quite remarkable absence of atomic scale features in the STM image of BiCs-graphite reported recently by Gauthier *et al*,[47] if as was noted by those authors, there is a high concentration of Cs in the first subsurface gallery of their samples due to segregation effects.[47]

The calculated corrugation amplitudes increase by about 20% if the average tip-to-surface separation is decreased by 2.5 a.u.(see Fig.2,3 in Ref.[45]), but the carbon site asymmetry values do not show strong dependence on the tip separation.

The behavior of the asymmetry between the α and β carbon sites is very interesting. There is no hint of any asymmetry for m=1 or 2 in Fig.3-5 or for m=1,2, or 3 in Fig.3-6.

This is a surprise since bilayers and trilayers of *AB* stacked pristine graphite display a strong asymmetry. Tomanek and Louie[40] have pointed out that in stage 1 alkali metal GIC's which have *AA* stacking there should be no carbon atom asymmetry since the asymmetry is linked to *AB* stacking. In agreement with our calculation, Biensan *et al* [48] also show the absence of carbon-site asymmetry in their experiments on m=1 domain of stage 2 $CrCl_3$-graphite which has a similar charge transfer coefficient to $SbCl_5$-graphite. The experiments did not show any evidence of absence of carbon site asymmetry in nominally m=2 domain, but the identification of the m=2 nature of the surfaces was indirect relying on bulk x-ray diffraction data.

Here we predict that the the asymmetry should be absent for small numbers of graphite layers covering the first guest layer, *even for AB stacking*. One can think of this very roughly as follows. The coupling between adjacent graphite layers is the reason why the CSA in the STM image of pristine graphite is linked to *AB* stacking. The coupling is stronger at α sites than β sites since the distance between the nearest-neighbor α-α sites on adjacent layers is the shortest one. Therefore, on the top surface layer the electrons on the α atoms have the larger probability of being attracted downward due to the coupling with the layer underneath, so that the β atoms are more visible in the STM image. When we intercalate some guests, say, acceptors, the charge transfer effect will cause carbon atoms to lose electrons. The electrons on the β atoms are somewhat less tightly bound to their sites and thus have the greater probability of being taken up by the intercalate. If the charge transfer is strong enough, it is possible to greatly reduce the difference between α and β sites in the STM image. This is a <u>very</u> rough and intuitive explanation; a more detailed explanation of the absence of CSA based on the properties of the system wavefunctions, the energy band structure and the Fermi surface will be given later below.

The asymmetry appears *abruptly* at m=3 in Fig.3-5 and at m=4 in Fig.3-6 but is weaker than in pristine graphite. This is quite different from the behavior of the corrugation hole at the center of the carbon hexagon which never disappears totally and grows *smoothly* with increasing m. We find that the finite asymmetry appears *discontinuously* with decreasing charge transfer at fixed m>1, when the highest electron (deepest hole) surface subband is emptied of electrons.

In Fig.3-7(a) we show the calculated carbon site asymmetry vs. $2f/q$ for m=2 surface domains. The CSA value is the height difference between α and β sites in the STM image. Curves "D" and "A" represent donor and acceptor guest GIC's, respectively, with the same constant tunneling current. In the Figure, there is a point at which the CSA switches on from zero to a finite value. The corresponding $2f/q$ is about 0.034 which varies very slightly (by $\leq 5\%$) with the bulk stage. As the STM probes the local electron density of states at the Fermi level, the discontinuity should be linked with the energy band structure and the Fermi level of the system. Figures 3-8(a) and (b) show the energy bands of pristine graphite bilayers and the m=2 surface domain of a donor GIC at the onset of the CSA with θ=0, respectively. Notice that the Fermi level coincides with the bottom of the highest electron surface subband in Fig.3-8(b). Consider the situation at κ=0, the corner of the hexagonal 2D Brillouin Zone (see Fig.3-2(c)). There $g(\mathbf{k})$=0, and the m=2 secular equations are

$$\begin{aligned} -a_1E + a_3\gamma_1 &= 0 \\ -a_2E &= 0 \\ -a_1\gamma_1 - a_1(E - \delta_{12}) &= 0 \\ -a_4(E - \delta_{12}) &= 0 \end{aligned} \qquad (31)$$

For pristine graphite bilayers, $\delta_{12} = 0$, and $E_F = 0$ as shown in Fig.3-8(a). Then from (31) we find $a_1 = a_3 = 0$, but a_2 and a_4 are not equal to zero. From Fig.3-2(b) it is clear that this

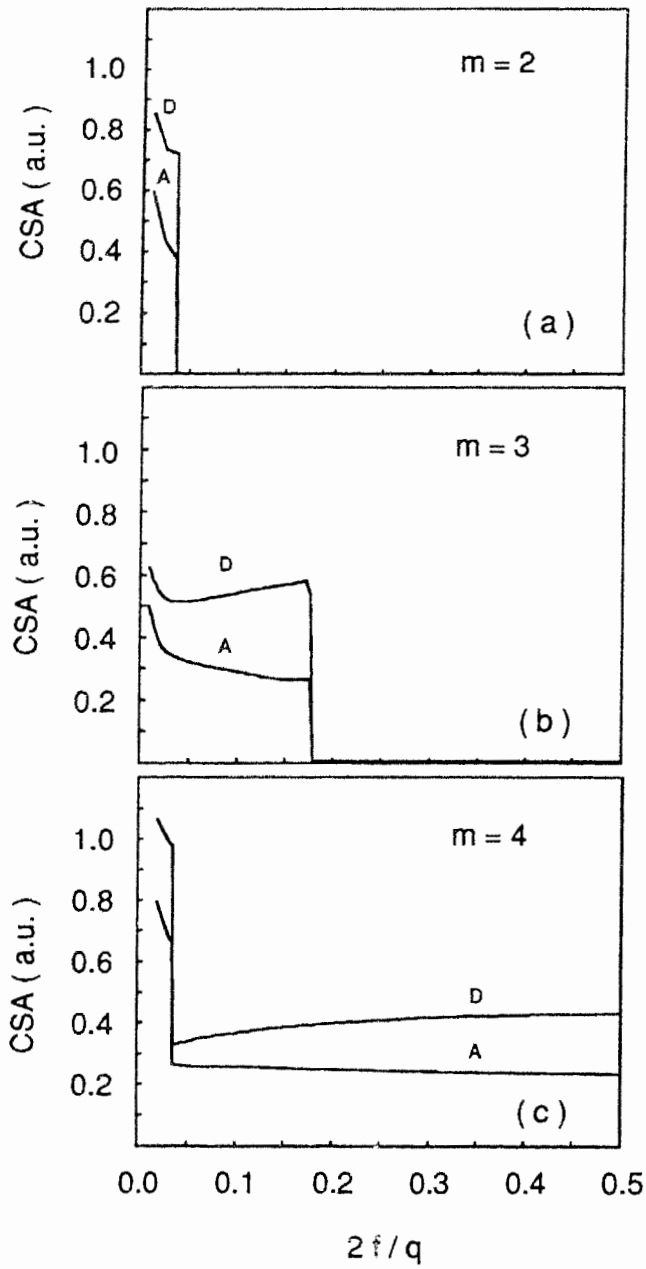

Fig.3-7: The calculated curves of carbon site asymmetry vs. $2f/q$ for (a) m=2, (b) m=3, and (c) m=4. A = acceptor, D = donor.

means that the Fermi electron wavefunction vanishes on the α sites. The tunneling current is therefore contributed only by β type atoms implying a strong CSA. By contrast, for a donor GIC at the CSA onset, the E_F just approaches the bottom of the highest electron surface subband E_{C1}. Since in this case $E_F > \delta_{12}$, it follows from (31) that for states at the bottom of this subband $a_2 = a_4 = 0$, but a_1 and a_3 are not equal to zero. This means that the subband E_{C1} strongly favors the α sites. Since the lower conduction surface subband E_{C2} also has many states at the Fermi level, and this subband strongly favors β sites, by adding these two parts we get the tunneling current contributed not only by β type but also by α type atoms implying a greatly reduced CSA. The higher conduction surface subband is parabolic at its extremum, which implies that (in two dimensions) it has a nearly constant density of states. Thus its contribution to the tunneling current (which strongly favors the α site) switches off discontinuously as it empties, which explains how it is possible for the asymmetry to be a discontinuous function of the Fermi level, or of the $2f/q$. The calculated results show that there is no CSA when $E_F \geq E_{C1}(\kappa=0)$.

We find that the energy bands of an acceptor GIC are simply the mirror image of those of the donor GIC with the same $2f/q$, and the Fermi level is the same in magnitude and differs only in its negative sign. That is why both kinds of GIC's have the common CSA onset.

From (31) we can obtain analytically the condition for the absence of CSA for donor GIC's in the case of m=2: $E_F \geq [\delta_{12} + (\delta_{12}^2 + 4\gamma_1^2)^{1/2}]/2$. Similarly, for acceptor GIC's, the condition is $E_F \leq -[\delta_{12} + (\delta_{12}^2 + 4\gamma_1^2)^{1/2}]/2$.

The CSA vs. $2f/q$ is plotted for m=3 and m=4 cases in Fig.3-7(b) and (c), and the respective energy bands in Fig.3-8(c) and (d), and (e) and (f). In Fig.3-7(b), the onset for m=3 is at about 0.175 which is much larger than the value for m=2. This is reasonable since the screening of the 1st guest layer increases with m, and the larger m, the less the

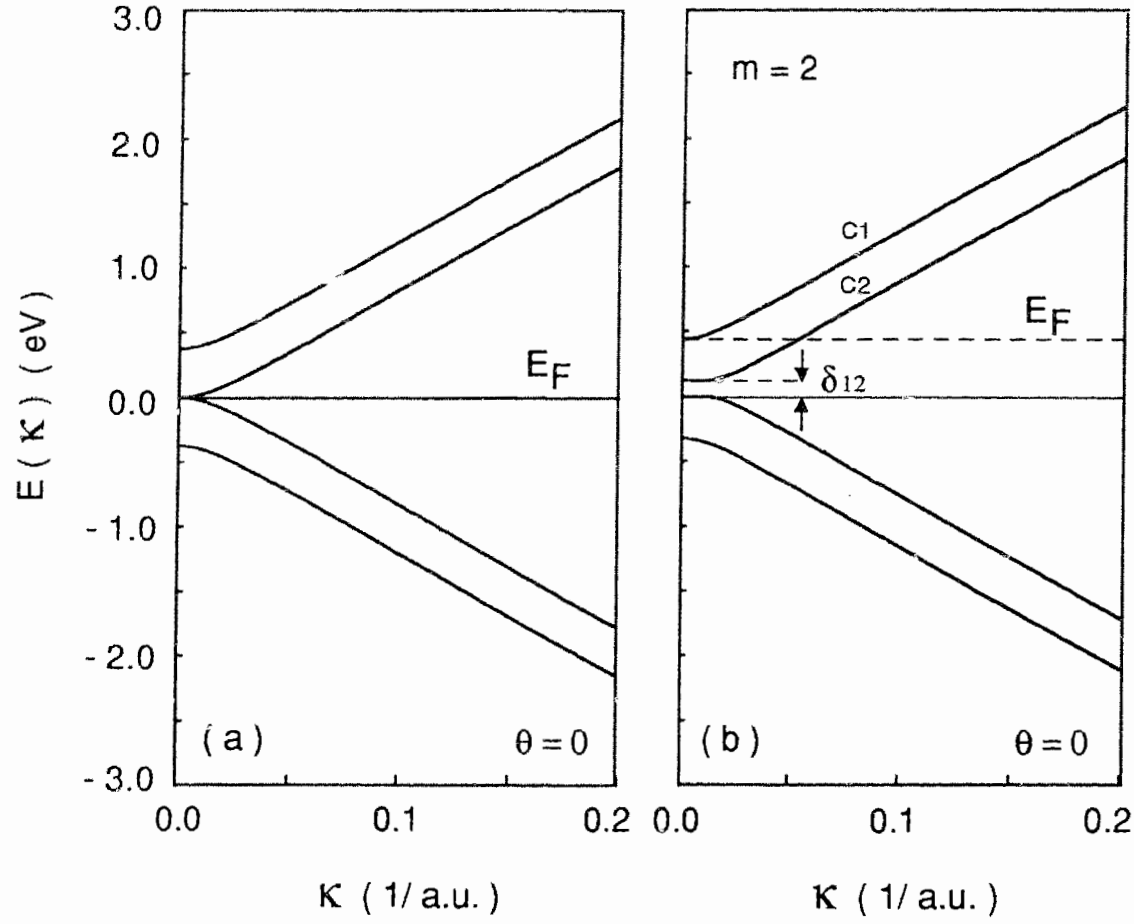

Fig.3-8(a) and (b): The energy band structure of m graphite layers with $\theta = 0$ (the band structure will change somewhat with θ, but the relative locations of subbands are always close to that shown). Pristine graphite bilayers in (a), m=2 surface domain of donor GIC's at the CSA onset in (b) with $2f/q$ value of 0.034.

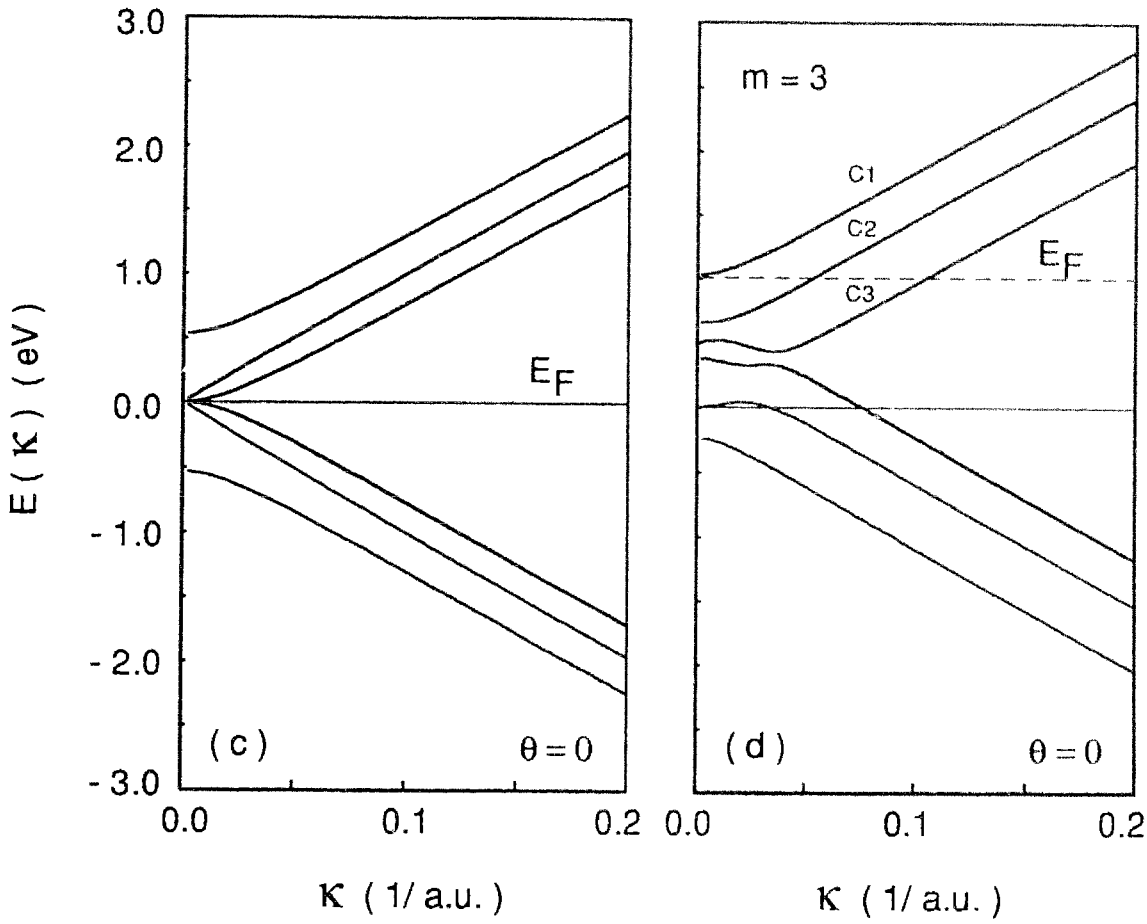

Fig.3-8(c) and (d): The energy band structure of m graphite layers with $\theta = 0$. Pristine graphite trilayers in (c), m=3 surface domain of donor GIC's at the CSA onset in (d) with $2f/q$ value of 0.175.

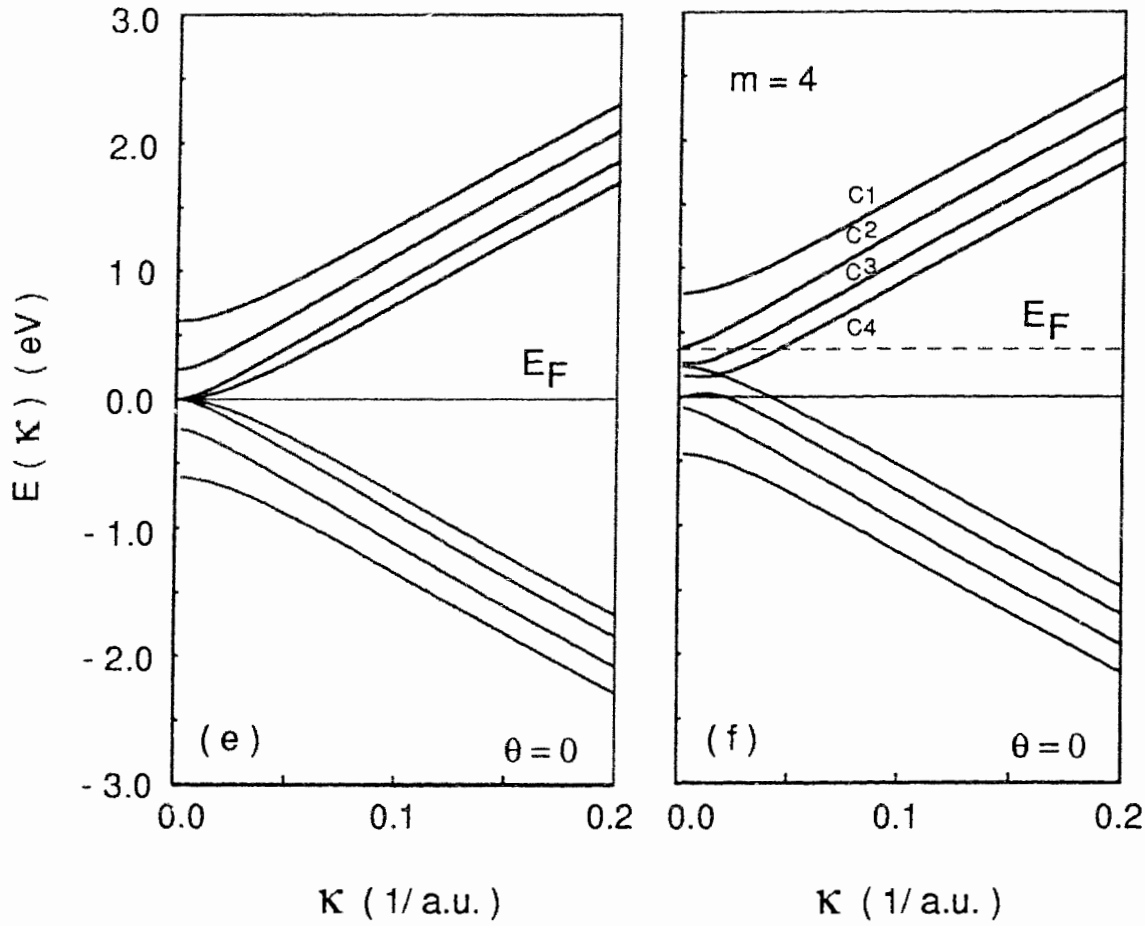

Fig.3-8(e) and (f): The energy band structure of m graphite layers with $\theta = 0$. Pristine graphite 4-layers in (e), m=4 surface domain of donor GIC's at the CSA discontinuity in (f) with $2f/q$ value of 0.037.

charge transfer affects the top surface. In Fig.3-7(c) the screening for m=4 is so strong that there is some CSA even when $2f/q$ reaches 0.5. But notice that the CSA jumps from a lower to a higher value when the 2nd conduction subband empties as shown in Fig.3-8(f). This occurs at an $2f/q$ of about 0.037, and the conditions of lower value of the CSA are that $E_F \geq E_{C2}(\kappa=0)$ for donors and $E_F \leq -E_{C2}(\kappa=0)$ for acceptors.

In general, the $2f/q$ at the CSA onset increases with m because of the effects of screening. The overall trend is for the CSA to increase with decreasing $2f/q$, but some deviations from this do occur. The difference between donor and acceptor asymmetry values tends to decrease with $2f/q$. It is zero for $2f/q$=0, i.e. for pristine graphite. For a fixed $2f/q$ the donor CSA is always larger than the acceptor CSA; this is because the form of $\Psi_{\mathbf{k}}$ is different for donor and acceptor GIC's even though their Fermi surfaces are the same.

It is interesting to see from Fig.3-7 that for some GIC's the CSA may be *larger* for smaller m. Fig.3-9 shows the STM images of m=1,2,3 and 4 domains for stage 4 MC_{12x4} with an $2f/q$=1/6. The asymmetry *decreases* significantly from m=3 (dashed line) to m=4. The reason is that the different surface subbands contribute differently to the asymmetry strength, so that their number and character and the location of the Fermi level *relative to them* are all important *and change with m*. It is clear that careful asymmetry measurements would be very interesting.

An excellent way to test our predictions experimentally would be to map out the surface domain structure of a freshly cleaved staged GIC, since different domains with different m values should have differing corrugation strengths and carbon atom site asymmetries, as well as having their surfaces offset vertically from each other[49] because of the bends in the graphite layers at the domain walls.

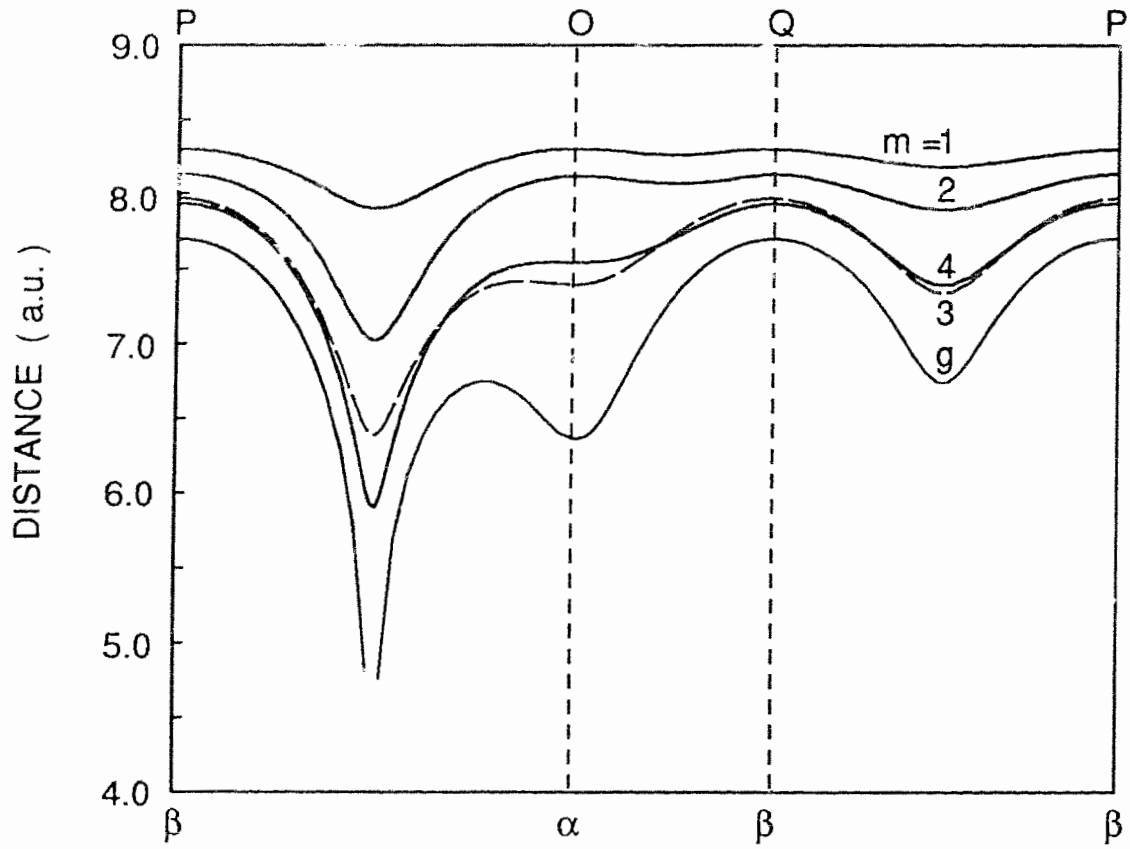

Fig.3-9: Calculated constant-current STM profiles for stage 4 MC_{12x4} alkali metal-graphite surfaces and for pristine graphite. Notation as in Fig.3-5.

3.4 Conclusions

We have developed the first theory of the STM images of the surfaces of staged graphite intercalation compounds. The number m of graphite layers covering the first guest layer and the charge transfer value are the important parameters entering our theory. We determine the transferred charge distribution along the c-axis, the surface energy bands and the Fermi level by using the Thomas-Fermi equations of Safran and Hamann and a modification of the tight-binding model of Blinowski and co-workers, and calculate the constant current mode STM image using Tersoff and Hamann theory.

We find that the corrugation amplitude and carbon site asymmetry are very sensitive to the m and the charge transfer, but insensitive to the bulk stage due to the screening of intercalant layers. The corrugation amplitude increases with increasing m, with decreasing charge transfer, and also with decreasing tip-to-surface separation. The asymmetry does not strongly depend on the tip-to-surface separation, but has a surprising dependence on the charge transfer and m, switching on discontinuously with decreasing charge transfer. We predict that in many cases there should be no carbon site asymmetry in the STM image even when the usual AB stacking of the graphite layers occurs at the GIC surface. The published experimental studies on some stage-2 accepter[48] and alkali-metal [61] GIC's have not observed this predicted anomalous behavior for the m=2 domains; further experimental work on this problem, preferably in vacuum, would be of interest.

For a given charge transfer, the corrugation amplitude is larger for acceptor GIC's and the asymmetry is larger for donor GIC's.

Our calculations explain the unusual absence of atomic-scale features in the STM images of BiCs-graphite reported by Gauthier and co-workers,[47] and the results for pristine graphite are in good agreement with those obtained using different theoretical

methods. Our prediction of the absence of carbon site asymmetry for m=1 case and the marked reduction in the strength of the depression at the center of the carbon hexagon upon intercalations have been evidenced recently in the STM study of $CrCl_3$-graphite surface by Biensan *et al.*[48] The marked reduction in the corrugations for alkali-meltals K, Rb and Cs GIC's have also been found by Kelty and Lieber,[61] which are consistent with our calculation results.

Our results for GIC's can be used to map the stage domains across a freshly cleaved surface and our predictions should stimulate further experimental and theoretical work in this interesting new area of surface science. Such studies will also help to clarify some currently controversial issues about the bulk properties of intercalation compounds.

Chapter 4

Atomic scale imaging of transition-metal-dichalcogenides surfaces with the STM

Like graphite, other layered materials such as transition-metal-dichalcogenides also have pseudo-two-dimensional character, i.e. the layers are weakly connected with van der Waals bonds. However, the distinct difference is that each layer consists of cations (transition metal) sandwiched between the two close packed sheets of anions (chalcogens). Each metal is surrounded by six chalcogen nearest neighbors either in trigonal prismatic or octahedral coordination (Fig.4-1) in the different compounds.[66] Since the surfaces of these compounds are expected to be flat on an atomic scale and to be easily cleaved, the atomic resolution STM images can be obtained even in air.

In this Chapter, I present our STM studies on the crystalline surfaces of 2H-MoS_2, WTe_2, and $ReSe_2$ compounds. Atomic resolution images are compared with the known crystal structure of these materials. Obviously, each transition-metal-dichalcogenide consists of two different types of atoms, not like graphite composed with only carbon atoms. Thus the natural questions on the STM images are not only which image is the principal image obtained by a single-atom tip, but also what is the chemical identity of the individual atomic species that has been registered in the images of the compounds surfaces. We give our interpretations for the images of each material, and discuss some tip induced artifacts affecting the STM results.

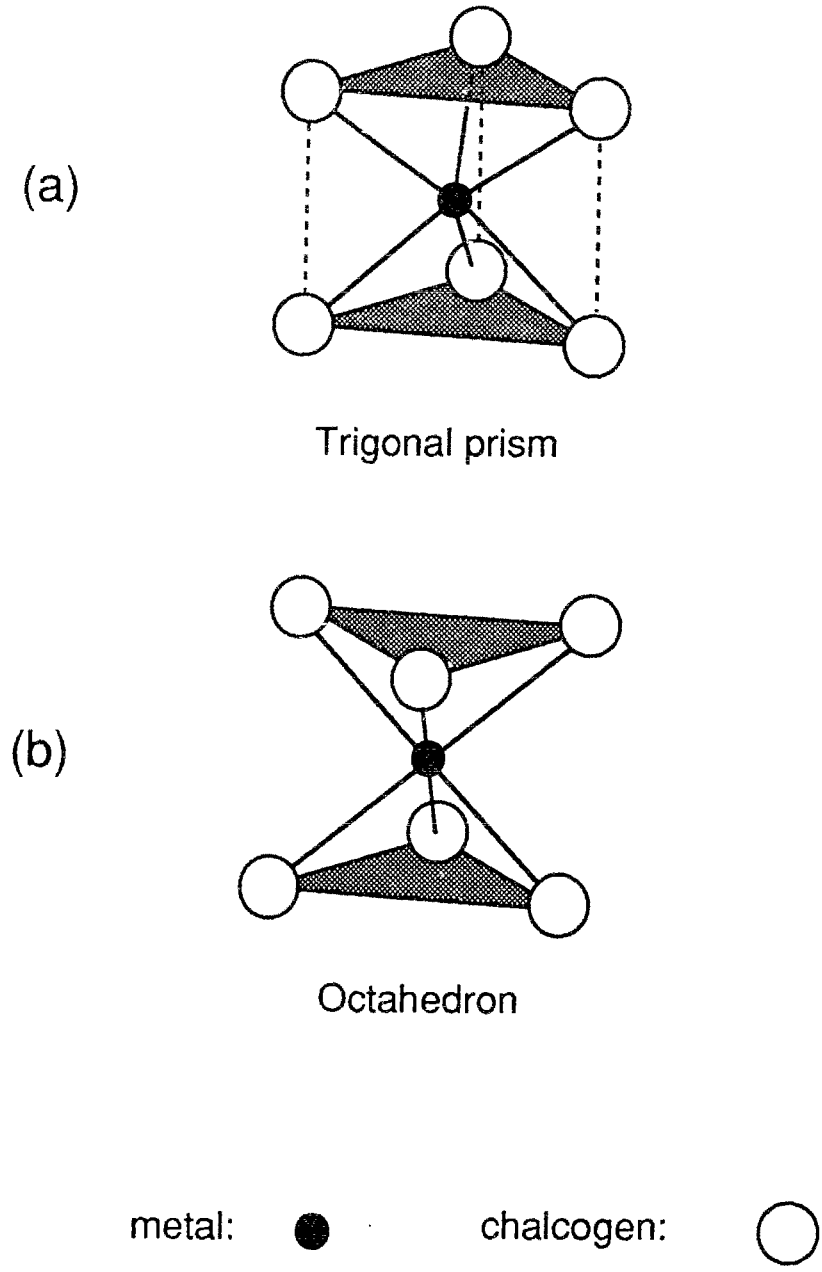

Fig.4-1: Two different types of coordination units of six nearest chalcogen atoms around one transition metal.

4.1 Molybdenum disulfide

Molybdenum disulfide is a relatively inert semiconductor compound, with a structure consisting of hexagonal layers of Mo atoms sandwiched between two hexagonal layers of S atoms (Fig.4-2). Each Mo has six S nearest neighbors arranged in the form of a trigonal prism coordination, the bulk unit cell spans two layers when MoS_2 crystallines in the $2H$ polytype, which occurs naturally as the mineral molybdenite.

The samples used for the STM studies were mined from China and Norway and kindly donated by Dr. Frindt. Since electrical resistivity parallel to the basal plane (10 ohm-cm) is two orders of magnitude less then that exhibited perpendicular to the planes,[66] we use silver paste to glue a copper electrode wire on the corner of a $2H$ -MoS_2 surface and usually to coat the edges of the sample in order to take advantage of this higher in-plane conductivity.

Because there is a substantial Mo $4d$ contribution at the top of the valence band and the bottom of the conduction band, Stupian and Leung[67] suggested that the MoS_2 image is a representation of the electron density primarily associated with molybdenum atoms, not sulfur atoms, even though the latter are on the top surface. Weimer *et al*[68] claim that they have obtained two distinct atomic sites in the STM images of MoS_2 surface, and concluded that the brighter spots were due to sulfur atoms since they are closest to the tip, while the faint spots arose from molybdenum atoms right below the top S atoms sheet. They also found that there is no qualitative different in the image pattern between difference bias polarities.

There has been no conclusive evidence to prove whether the 2H-MoS_2 image reflects the surface sulfur layer, or the metal layer underneath. This controversy arises because both the S atoms in the top surface layer and the Mo atoms in the middle of the first sandwich

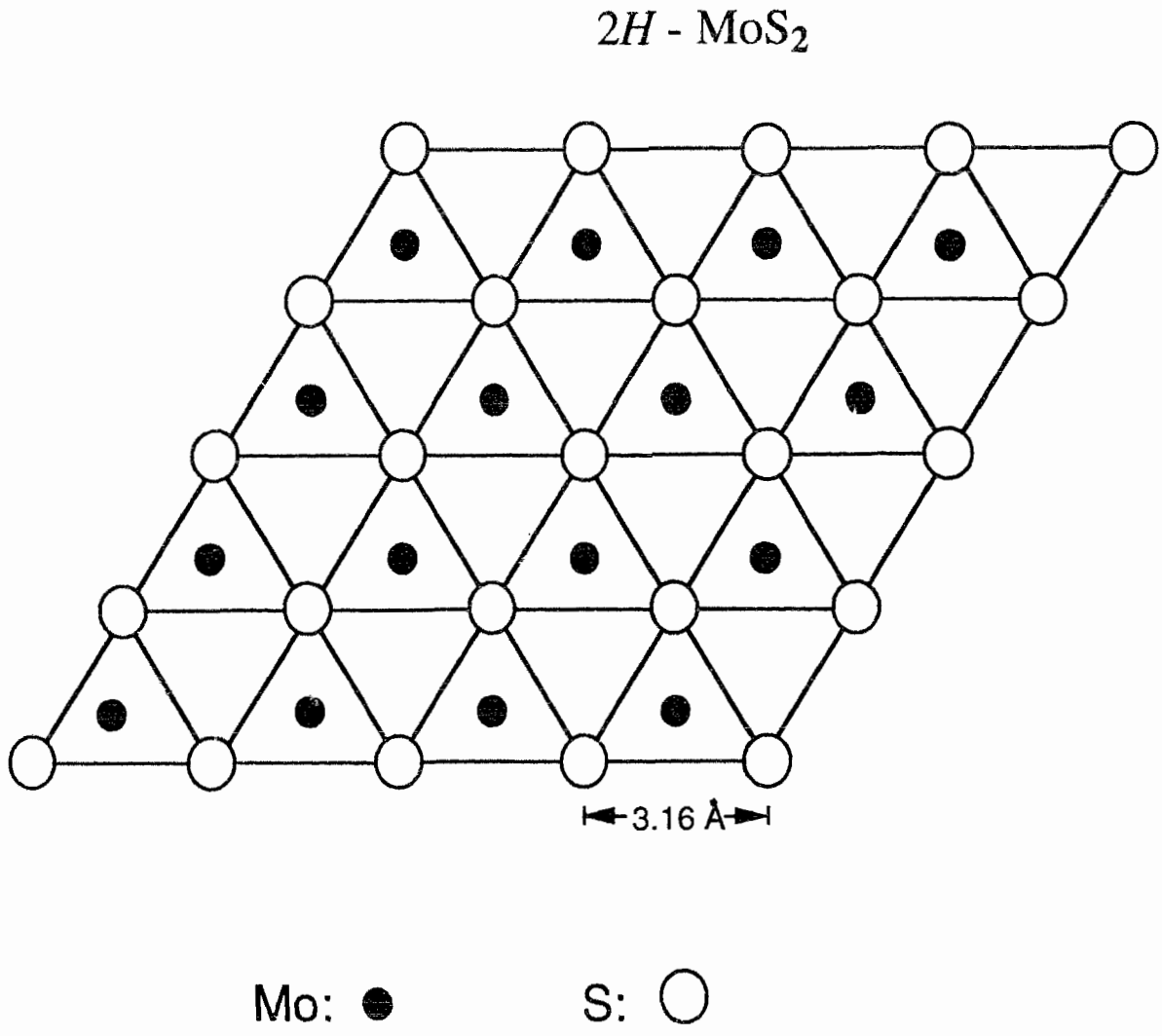

Fig.4-2: Basal surface structure projection of $2H$ -MoS_2. The Mo atoms are in the plane 1.59Å below the S atom plane.

appear in equal numbers, and the atomic structures for both layers have the same symmetry. Consequently, an image of either Mo or S atoms would have the same pattern with the same lattice constant. But the claim of seeing two distinct atomic sites is rather speculative, because it is difficult to distinguish them from tip induced artifacts, as the image may also be explained by two single-atom tips effect similar to that exhibited in graphite case.[27]

Fig.4-3 shows the raw data of a grey scale current image (constant-height mode) of a single crystal 2*H*-MoS_2, which was taken with the STM system described in Chapter 2 with a positive tip bias of 155mV(sample is grounded), an average tunneling current of 1.5 nA and a scan rate of 1774 Å/sec. The image consists of an array of bright spots with the expected sixfold symmetry. The calibrated lattice constant is $a_0 = 3.1 \pm 0.1$ Å, which is in good agreement with the crystallographic value of 3.16 Å.[66]

The above image was obtained with rather low bias voltage compared with the approximately 1 eV[69-72] band gap for 2*H*-MoS_2. We can even obtain very good atomic-resolution images at positive tip biases of order of 10 mV(Fig.4-4), though generally we found it easier to achieve very stable tunneling with a tip bias larger than 100 mV. The fundamental reason for the low bias imaging may arise from the existence of a certain doping density inside naturally mined samples, as it is known that molybdenites can be n-type, p-type or heavily compensated semiconductors.[66, 73] Fan and Bard[74] found that an STM image of the (001) surface of n-TiO_2 could be obtained with low forward bias condition (positive tip bias). With a reverse bias, the tip may crash onto the surface because the presence of a space charge layer within the semiconductor inhibits the tunneling.[75] However, Uosaki *et al* found that for highly doped (N_D~8×10^{18} cm^{-3}) n-GaAs, STM measurements were possible even under reverse bias conditions.[76]

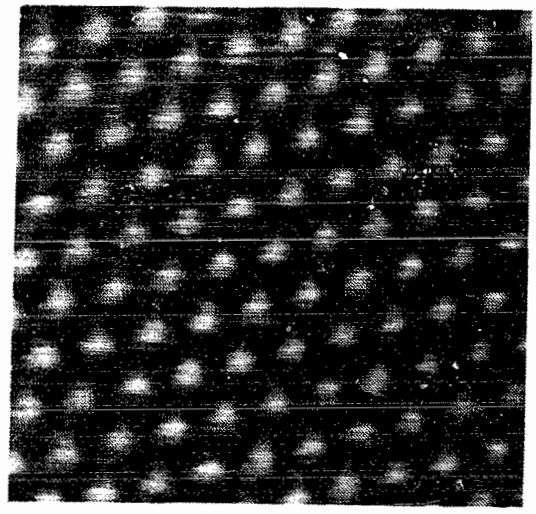

Fig.4-3: A constant-height mode image (~28Å x 28Å) of a single crystal 2*H*-MoS_2 (China).

The doping levels of the molybdenites we used were not characterized, so that we can only suggest the following possibilities for the mechanism of the low bias imaging. With a very small tip(metal)-sample(semiconductor) distance, the molybdenite energy band will bend at the surface either like a Schottky barrier or close to an Ohmic accumulation condition.[77] Positive tip bias condition corresponds to a forward bias situation for n-type molybdenite, and reverse bias for p-type molybdenite. If the accumulation condition occurs, then there is not much question on the possibility of tunneling at even small bias, since the accumulation layer in the semiconductor serves as a ready reservoir of majority carriers for conduction. If the Schottky type of barrier occurs, however, we need to discuss n-type and p-type situation separately.

If the molybdenites we used are the n-type, there is an electron layer at the surface of the semiconductor and a positively charged depletion layer in the semiconductor near to the surface to form a Schottky barrier. With the application of a forward electric field to the tunneling unit, the barrier height from the bottom of the conduction band in the semiconductor is reduced(Fig.4-4(b)). Therefore electrons in the conduction band may overcome the barrier to reach the surface, or tunnel through the space charge region toward the surface, hence contributing to the STM tunneling current. The probability for barrier tunneling depends on the thickness of the space charge region which decreases with increasing doping density. It has been reported that a considerable space charge tunneling can be observed even for the less highly doped n-GaAs,[76] and that the electron concentration at the surface of n-type semiconductors increases rapidly with the forward bias.[74, 76] Under these circumstances, it is possible for us to obtain STM images of a n-type molybdenite with a low positive tip bias, even though the sample may be less highly doped. If the molybdenites we used are p-type, then the doping level must be very high to be able to get STM tunneling current. Since the barrier height is enlarged under reverse bias

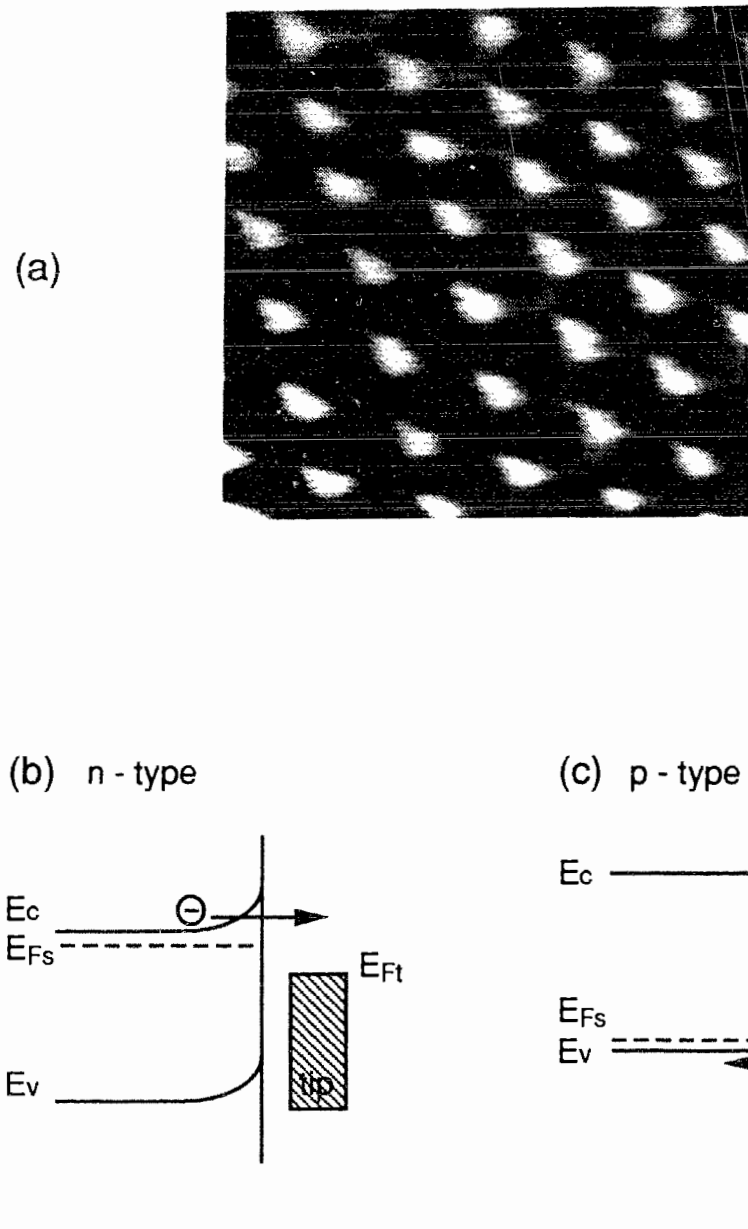

Fig.4-4: (a)Another constant-height mode image (15Å x 20Å) of a molybdenite (Norway) with positive tip bias of 44 mV and average current of 1nA. Energy band diagrams for low positive tip bias with a molybdenite of (b)n-type or (c)p-type.

(Fig.4-4(c)), the doping density should be so high that the space charge region is thin enough that the holes can tunnel from the tip to the semiconductor valence band. Further experiments on the characterization of the sample doping level and on the tunneling spectroscopy of the semiconductor surface would be necessary to give detailed information about the small bias imaging.

We also observed very active tip reforming effects in the experiments. Fig.4-5 presents a set of constant-height mode images obtained from a molybdenite surface around a same location, with positive bias of 140 mV and average tunneling current 1.2 nA. After scanning for a while the image suddenly became noiseless with very high corrugation (Fig.4-5(a)). If we look at the image carefully, we see that the image consists of two sets of hexagonal bright spots— a large size set and a very small size one. Sometimes the smaller size spots are absent, as shown in Fig.4-5(b). A few minutes later we got an image shown in Fig.4-5(c), in which there was a tip change as indicated by the abrupt horizontal break. The image evidences that the two sets of bright spots observed in Fig.4-5(a) were due to a tip effect, as the relative brightness of the two kinds of spots had been switched after the break. Then we obtained images shown in Fig.4-5(d) and Fig.4-5(e), different patterns of the overlap of two sets of hexagonal lattices. Finally, an image pattern was obtained which remained extremely smooth and noise free for almost *two hours*. An example of this image is shown in Fig.4-5(f) as it was obtained without being filtered by computer software.

We learn again that the STM image interpretation is not straightforward. The main obstacle is that the tip structure is unknown and it has a subtle effect on the STM image. By using a time ordered sequence of real-time images, however, we can usually rule out artifacts. For instance, according to the previous images obtained we tend to believe that Fig.4-5(f) is due to a superposition of two images of the type shown in Fig.4-5(b), rather than the sample properties.

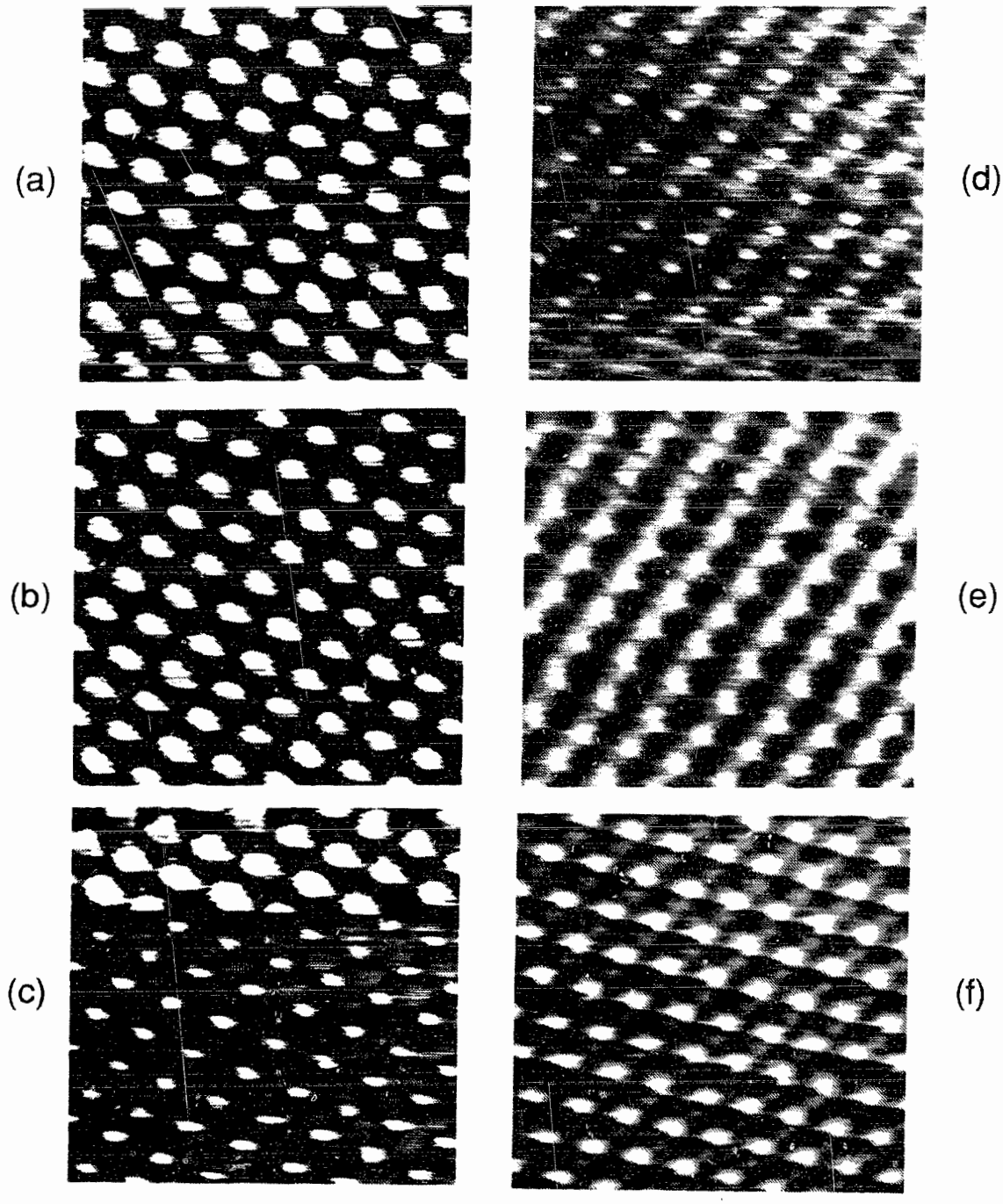

Fig.4-5: A set of constant-height mode images (~ 26Å x 26Å) of a molybdenite (Norway) surface.

It is our experience that in contrast to the graphite case high quality images were seldom obtained immediately from the MoS_2 crystals. The initially noisy MoS_2 images are associated with more active tip reforming processes than are present in the graphite case and the best image often occurs all of a sudden, as shown in Fig.4-6. However, once this noise-free image is obtained it can be retained during two hours of high-quality and noise free scanning (Fig.4-5(f)) without visible change in the image pattern, compared to the approximately 10 minute periods in the graphite case. The underlying reason for these phenomena is not clear. We speculate that these may be related with the possibility that there are S and Mo species terminating the tip, which could be lifted from MoS_2 surface during the low bias imaging. This is analogous to the situation in graphite[78] and other materials[79, 80] where surface atoms are sometimes found on the tip. As the atoms picked up from the surface on the tip may not have the stoichiometric ratio of 2:1 for S and Mo, and thus the tip may tend to pick up the additional atoms required to achieve chemical balance by means of reforming itself to find a proper structure configuration through interaction with the MoS_2 surface in the tunneling process. Presumably, the reforming may be much more active and prolonged than is found in graphite case, because more than one atomic species and more dangling bonds are involved. The extreme stability of the two hours long imaging may be due to the fact that a stable and chemically attractive interaction between the tip and the surface has been achieved with a stable configuration of a Mo atom, for example, adsorbed on the Pt-Ir tip.

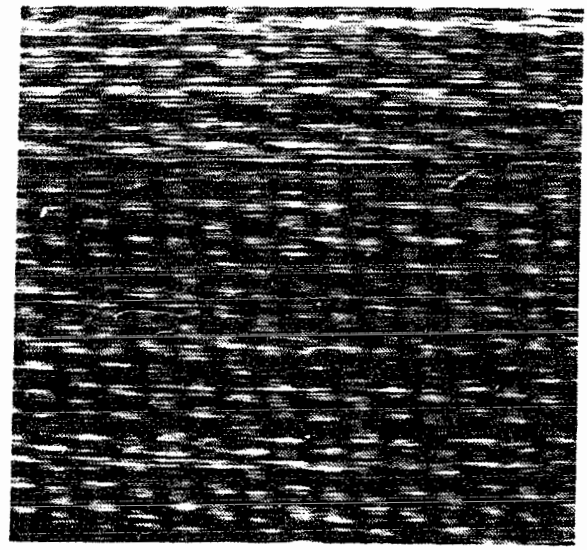

(a)

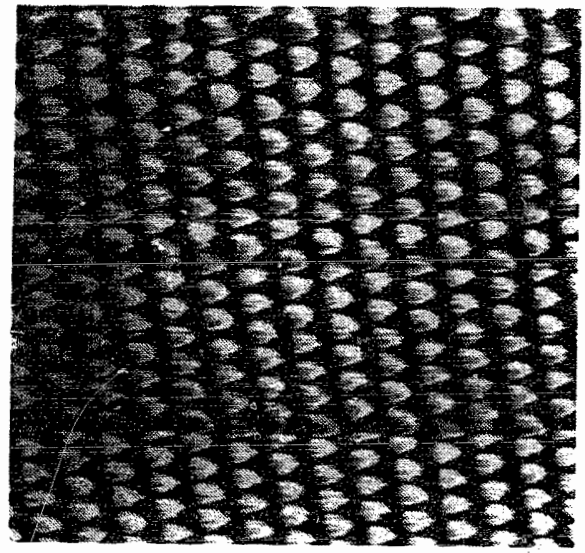

(b)

Fig.4-6: Two constant-height mode images taken from a same surface location of a molybdenite (China) with a positive tip bias of 226 mV and average tunneling current of 3.5 nA. (a)The imaging is rather noisy initially for a quite while, and (b)high quality image (36Å x 58Å) often appears all of a sudden.

4.2 Tungsten ditelluride

Crystalline WTe_2 possesses a distorted octahedral structure. Within each layer, the W atoms were displaced from their octahedral coordination unit centers in such a way that every two rows of W atoms pair to form zigzag and slightly buckled chains. This also causes the Te atom sheets to buckle somewhat, but appear approximately hexagonal in the surface projection view (Fig.4-7). The perpendicular distance between the paired W rows is 2.2Å, and the surface unit cell is rectangular with the dimensions of 6.28Å x 3.50Å.[81-83] The surface projection structure is an 2x1 superlattice of the approximately hexagonal sublattice of Te atoms.

Since the symmetry of the metal and chalcogenide sublattices is different, one may expect to address the surface Te layer and the subsurface W layer distinctly in the STM image. Tang *et al*[82, 83] have imaged WTe_2 with an STM and found zigzag structure in the images. Based on their calculations of the spatial distribution of the valence charge density (due to the filled states) on the WTe_2 surface,[83] they concluded that the Te charge cloud centers shift from the real atomic sites and give an overall paired zigzag and buckled appearance. The distance between the two paired clouds is larger than that between the paired W rows, and increases with tip-to-surface distance. Also, the spatial distribution of charge is bias voltage and polarity dependent. Therefore, they conclude that for this highly covalent compound the image is not necessarily in registry with the surface atomic positions.

Fig.4-8 shows two constant-current mode images obtained from a WTe_2 sample (made and given by Dr. Frindt) surface being scanned in perpendicular directions. Both images were taken in air, with low positive tip bias of 97 mV and relatively high tunneling

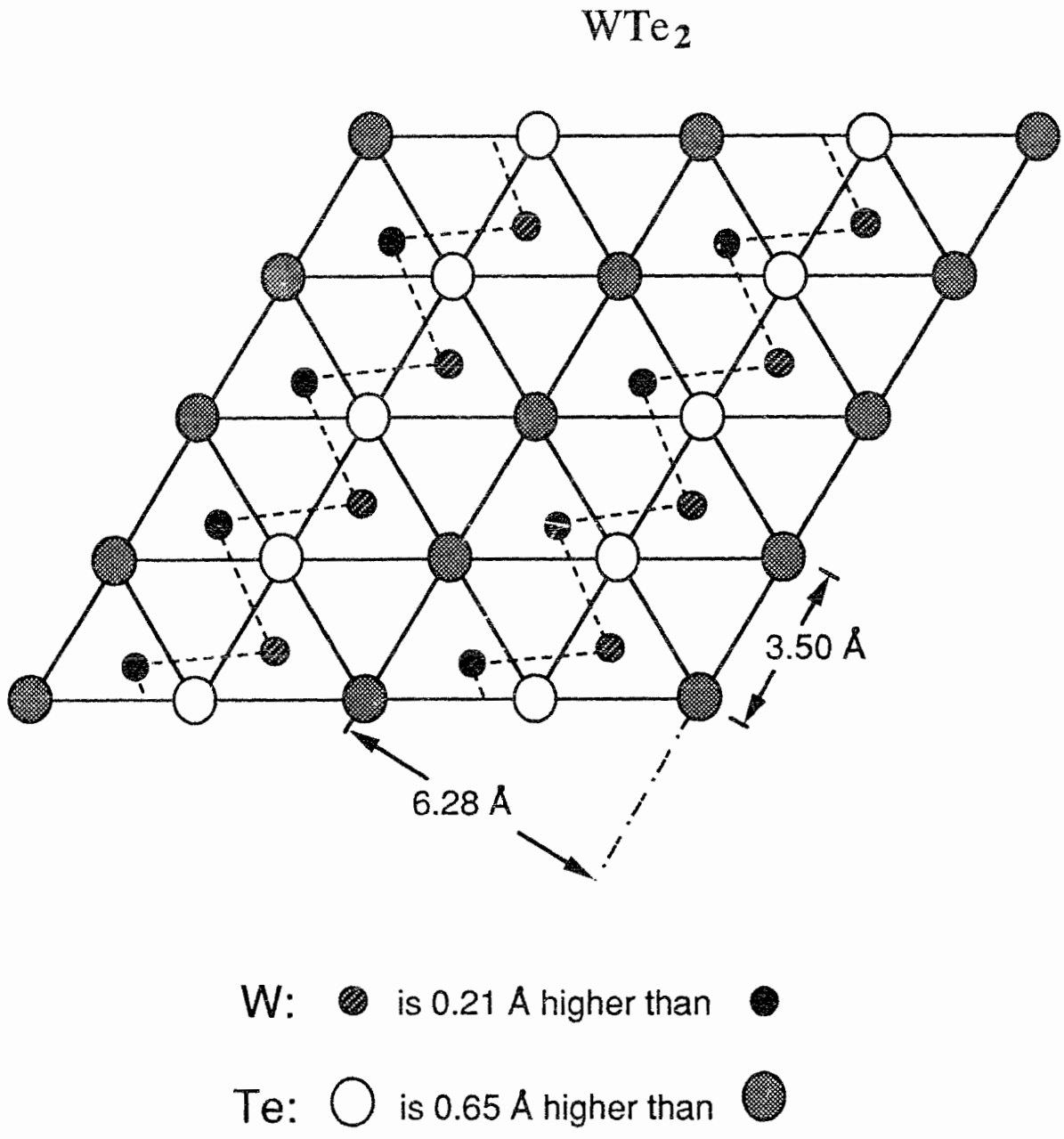

Fig.4-7: Basal surface structure projection of WTe_2.

current of 2.2 nA, as WTe_2 is a semi-metal compound with much lower resistivity of ~$2x10^{-3}$ ohm-cm than that for MoS_2.[66] The images clearly show the expected 2x1 structure. There are two alternating types of rows with spots different in size and brightness.The calibrated rectangular unit cell parameters are 3.4 ± 0.1Å and 6.4 ± 0.2Å in agreement with the crystallographic values of 3.5Å and 6.28Å (Fig.4-7), respectively.

The image shown in Fig.4-8(a) looks particularly like the spatial charge density distribution of a WTe_2 surface due to the filled states calculated by Tang *et al*,[83] thus we tend to believe that it represents the principal image scanned by a single-atom tip. Also, we found that the distance between the two paired rows changes from images obtained at different positive tip bias. Evidently, the phenomenon supports the prediction calculated by Tang *et al* that the surface charge density distribution is dependent on the tip-to-surface distance.[83] In our experiments the tunneling current is constant and equal to the preset value regardless of the bias voltage applied to the tunneling unit. Therefore, changes in the bias value will result in the changes of the tip-to-surface distance.

The two images in Fig.4-8 are consistent with each other, except Fig.4-8(a) shows higher resolution. The relatively poor resolution in Fig.4-8(b) is mainly due to the faster scan speed in the horizontal direction than that in the vertical direction. Faster scan speeds limit the corrugation amplitude probed in the constant-current mode image, especially if the tip is not sharp enough.

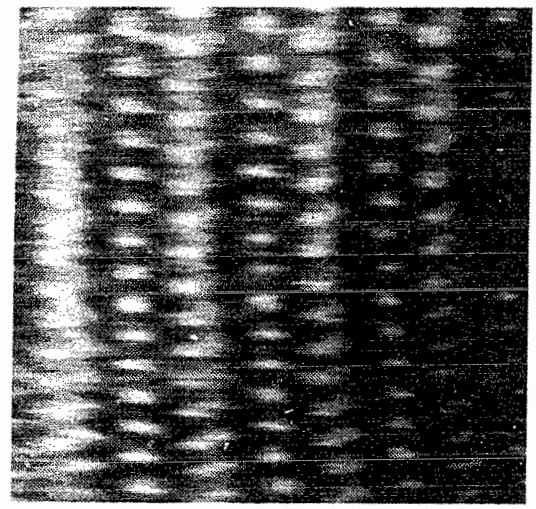

(a)

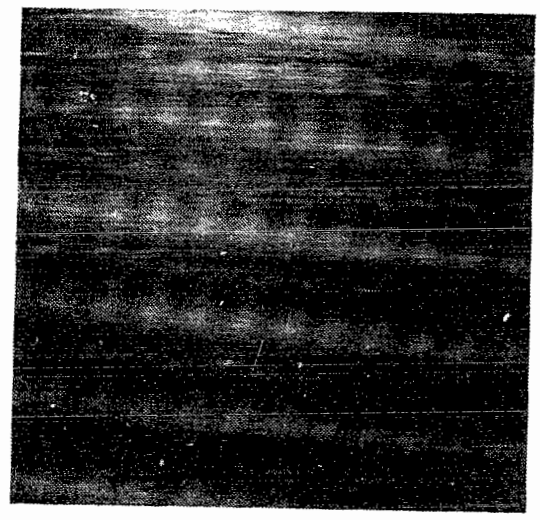

(b)

Fig.4-8: Constant-current mode images obtained from a WTe_2 surface being scanned in perpendicular directions. The image dimensions are 25Å x 50Å for (a) and 36Å x 32Å for (b).

4.3 Rhenium diselenide

Crystal $ReSe_2$ is a semiconductor compound with about the same energy gap (1.18eV)[84] and resistivity (8 ohm-cm)[84] as that for crystal MoS_2.

Similar to WTe_2, $ReSe_2$ also possesses a distorted octahedral structure, but the metal clustering is a slight modification of the regular zigzag structure. The Re atoms shift off from their regular octahedral sites in such way as to form chains of metal-metal-bonded "diamond" clusters (Fig.4-9). The average bond distance within each Re_4 cluster is 2.83Å, and each diamond cluster is connected with a 3.07Å Re-Re bond.[66, 85] This causes the Se atom sheets to buckle slightly, but appear approximately hexagonal from above. Thus the basal plane lattice is a 2x2 superlattice of the hexagonal sublattice of Se atoms. There are four Se-atom sites for the basal plane unit cell, which are designated Se(1), Se(2), Se(3) and Se(4) in Fig.4-9. The lattice constant along the chain direction is 6.60Å which is a little different from the other unit cell parameter 6.72Å.[85, 86] This difference, however, is difficult for the STM to resolve.

Again, in crystalline $ReSe_2$ the symmetry of the metal and chalcogenide sublattices are quite different. Parkinson *et al*[87] explain that the STM image is a representation of Se atoms on the surface, although there are greater contributions of Re 5d orbitals than Se 4p orbitals on the bottom of conduction band and top of valence band. According to their calculations of the local density of states (LDOS) $\rho(\mathbf{r},E_F)$ for the Se 4p orbitals of the surface layer, the brightness of the four Se atoms in the surface unit cell is bias voltage and polarity dependent. In the case of valence band imaging, Se(3) and Se(4) atoms would give rise to brighter STM images, although the Se(1) and Se(2) atoms are geometrically closer to the tip.

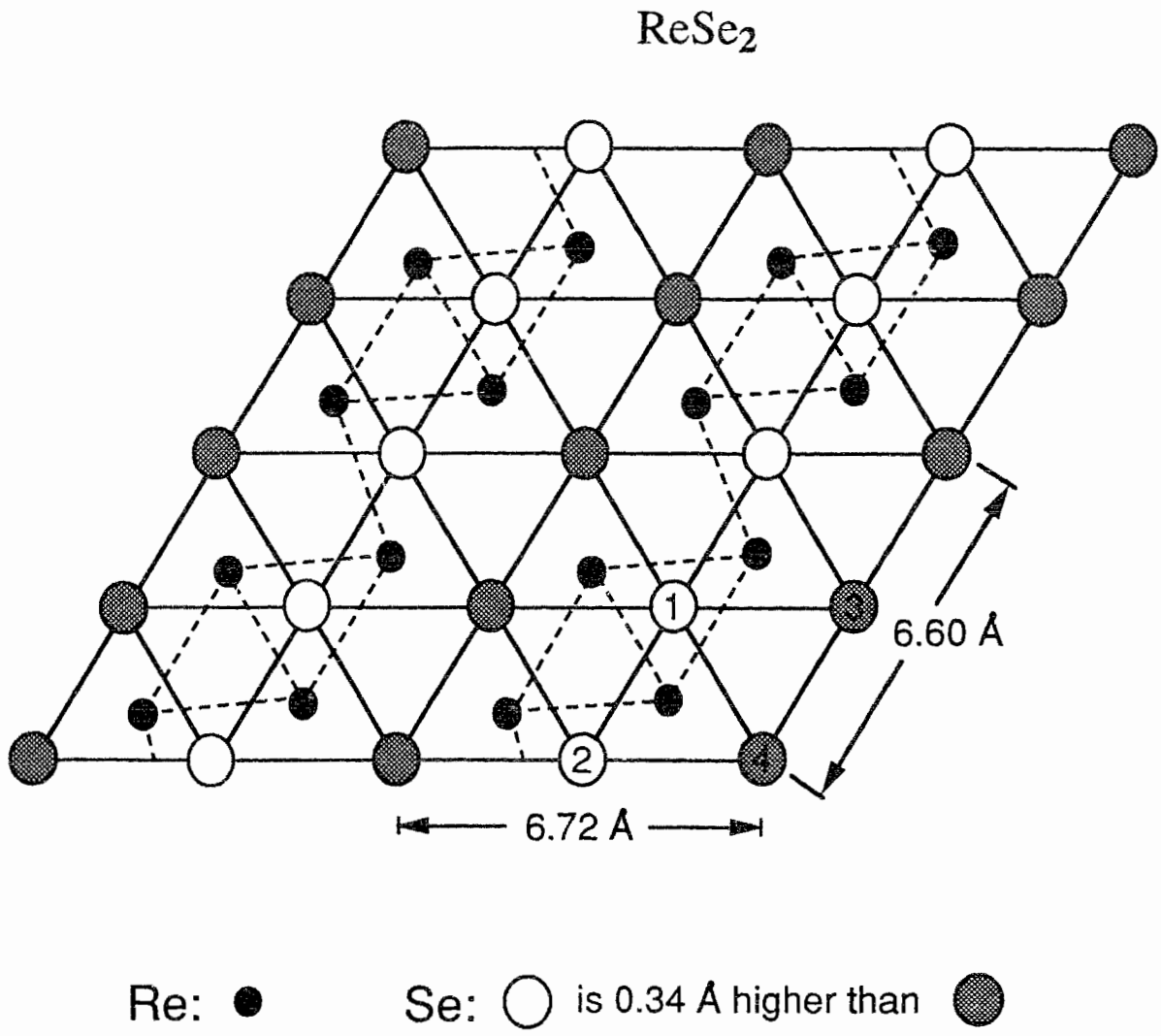

Fig.4-9: Basal surface structure projection of $ReSe_2$.

We use a $ReSe_2$ sample (made and given by Per Joensen) which was cleaved with Argon gas blowing on the sample surface, and imaged by using a glove bag with an Argon gas environment. We used an Argon gas environment for the observation because we found that in air the bias had to be continually increased with time in order to see the surface atomic structure, presumedly because the surface is very reactive and easily contaminated.

Fig.4-10 shows three 42Å x 42Å greyscale images obtained with constant-height mode under the same experimental conditions. A positive tip bias of 2.3V was used, resulting in surface-to-tip electron tunneling, which involves tunneling from states near the top valence band. The average tunneling current was set to be 1.5nA. The 2.3V bias is found necessary for the 1.5 nA current in order to get atomic-resolution images from the $ReSe_2$ surface. Such current and bias values are consistent with the published measurement of the tunneling current as a function of the bias voltage by Parkinson *et al.*[87] The calibrated average lattice constant is given as 6.6 ± 0.2 Å which is in good agreement with the crystallographic unit cell parameters (see Fig.4-9).

Fig.4-10(a) clearly shows the expected 2x2 surface structure. The image pattern is similar to the LDOS calculation published by Parkinson *et al.*[87] There are four distinct bright spots, with three located at the right sites of the hexagonal sublattice of Se atoms and one (close to the brightest) displaced from the regular position, which appear with differences in brightness and size. From the structural symmetry point of view, we agree that Se atoms are primarily represented in the STM image. However, the difference of these spots in brightness and size, and the appearance of the one site displacement are strong indications of Re_4 cluster influence in the subsurface.

To determine the diamond chain direction or to identify each individual Se atom in the image is not that straightforward. Since the LDOS calculations[87] show that the image

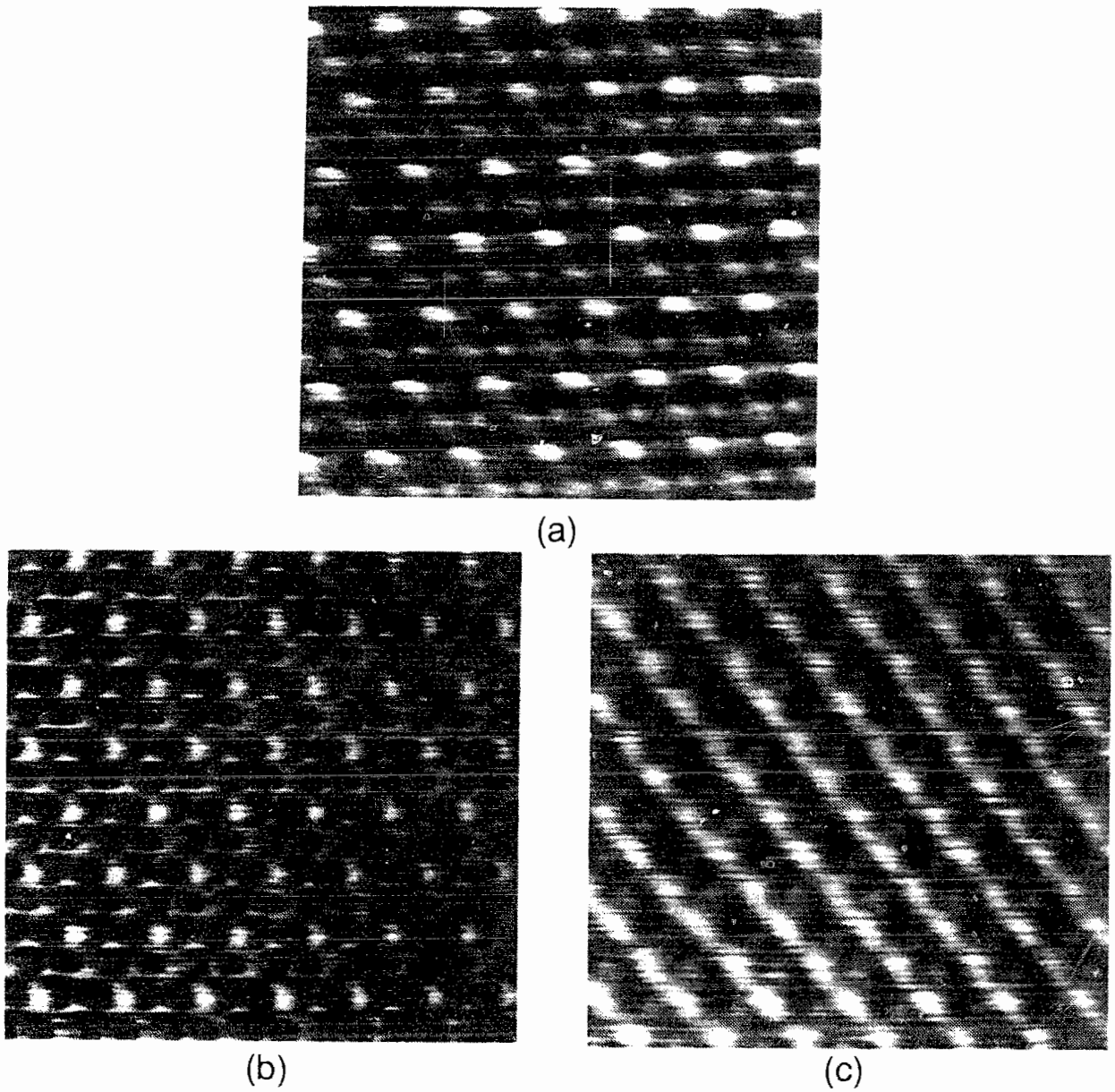

Fig.4-10: Three constant-height mode images (42Å x 42Å) of a $ReSe_2$ surface .

depends on the bias voltage. With a bias which puts the band levels within 0.5 eV from the valence band top, the brightness in the image decreases in the order Se(3) > Se(4) > Se(2) > Se(1); however, with larger bias the Se(4) atoms may be the brightest and the other three appear about the same; hence with certain bias, Se(3) and Se(4) atoms may appear identical in brightness. Fig.4-10(a) should belong to the 2nd case, since 2.3V is a large bias if it is compared with the $ReSe_2$ band gap of 1.18 eV. Therefore, the brightest spots in the image correspond to Se(4) atoms. But the three types of faint spots are difficult to register in terms of brightness, although one type size is distinctly larger than the other two. Geometrically, we know that the strong depression in the tunneling current should happen around the centers of the triangles formed by Se(4), Se(3) and Se(2) sites, where less atoms are around. Notice that there are rather large dark hollows closely located in the lower-left places nearby each Se(4) atom (the brightest spots), we then can register Se(1) atoms to the largest faint spots in the image. However, Se(2) and Se(3) atoms less likely can be determined by this image alone. The image structure could be in the atomic arrangement shown in Fig.4-9, or in such a manner that the diamond chain direction is approximately horizontal. Since the $ReSe_2$ image depends sensitively on the bias voltage and bias polarity, further experiments with different bias, especially simultaneous image acquisitions at two different biases (for example, by forward scanning with one bias and backward scanning with a different one, or by scanning alternate lines at each bias) would help to unambiguously identify the different Se atomic sites.

We have also obtained novel patterns of the valence band image. Fig.4-10(b) and Fig.4-10(c) are images of about the same surface location, obtained about 40 minutes in separation. The images appear quite smooth without using any computer filtering function. Fig.4-10(b) obviously shows the 2x2 lattice structure. However, there are likely four kinds of distinct dark "holes" located approximately at the hexagonal sites of the Se sublattice

instead of bright spots, which are different in size and darkness. It seems the inverted image of the real surface. We attribute this to a multi-tip effect, just similar to the honeycomb pattern (see Fig.2-5) observed in the graphite image. Fig.4-10(c) still shows the 2x2 structure if one notices the period of the larger dark spots in the image, though at the first sight looks like a kind of 2x1 lattice. The image is composed of two rows with clearly different brightness. Since the bias voltage is the same for all three images shown in Fig.4-10, it is not likely due to an electronic reason that Se(3) and Se(4) sites appear equal in Fig.4-10(c). It must be concluded that changes in tip condition account for the differences between Fig.4-10(a) and Fig.4-10(c). Actually, the image pattern shown in Fig.4-10(c) can be viewed as a sum of two images (due to two single-atom tips) like that shown in Fig.4-10(a). Therefore, we believe that Fig.4-10(c) is not the principle image of the surface.

There is no significant image difference between the positive and negative tip bias conditions in our experiments. The LDOS calculation[87] shows only different Se atom sites being brighter in the conduction band image. All the images we obtained show the expected 2x2 structure, but the internal structure of the basal plane unit cell is often different from one image to another. This could be due to an electronic reason if the bias voltage is different. For the same bias voltage, then, as we know previously, tip induced artifacts are always possible in the STM images.

4.4 Comparisons and conclusions

The overall structure for the chalcogen sheets of the three different crystalline surfaces is an approximately hexagonal lattice, as shown in Figs.4-2, 4-7 and 4-9. However, the metal sheet sandwiched between the two chalcogen sheets has very different atomic

arrangement for each crystal. The Mo sheet in MoS_2 shows the ideal hexagonal lattice, whereas W sheet in WTe_2 adopts an atomic zigzag structure, and the Re sheet in $ReSe_2$ appears with chains of Re_4 diamond clusters. Therefore, the surface projections of the three crystals can be viewed as 1x1 lattice of the corresponding chalcogen sublattice for 2*H* - MoS_2, 2x1 superlattice for WTe_2, and 2x2 superlattice for $ReSe_2$.

Our STM observations on these three crystal surfaces indeed display the expected the structural lattices (i.e. 1x1, 2x1 and 2x2), even though the images are not necessarily the reflections of the metal layers. Since the symmetry of Re layers in $ReSe_2$ crystal is different from that of Se layers, the observed four types of distinct bright spots in the image primarily represent the Se atomic sites, though the Re layer underneath has influence on the spot size and brightness and on the one spot site slightly shifted from the regular position of the Se sublattice. For the WTe_2 crystal, however, the observed zigzag pattern in the valence band images does not correspond to the W atomic sites, and changes with the tip-to-surface distance, indicating rather strong contributions from the surface Te atom layer. For a 2*H* - MoS_2 surface, there is no conclusive evidence to confirm which chemical identity has been imaged in the STM images, as there is no difference in the symmetry between the two types of atom sheets.

Chapter 5

Real-space imaging of single-layer MoS_2 in water by scanning tunneling microscopy

As we know from Chapter 4, molybdenum disulfide is a compound semiconductor, consisting of S-Mo-S sandwich layers.[66] In crystalline 2H-MoS_2, each Mo atom is coordinated by six S atoms in a trigonal prismatic arrangement. The adjacent layers are weakly connected with van der Waals bonds so that it is very easy to break these bonds by simply "pulling" off layers to obtain an atomically flat surface, or to intercalate guest atoms between the MoS_2 sandwiches. Recently, it has been shown[88, 89] that single molecular layers of MoS_2 can be obtained by exfoliation of lithium-intercalated MoS_2 powder in water and in several alcohols. When the single layers are restacked, a large variety of organic molecules can be included between layers of MoS_2. This holds the promise of making new artificial two-dimensional materials which would be difficult to obtain by other methods.[90, 91]

For the case in water, the exfoliated single layers are "washed" and suspended in water, to form an aqueous suspension of single-layer MoS_2 particles. As the aqueous suspension dries, it forms into restacked MoS_2 with two monolayers of water between parallel but rotationally disordered MoS_2 layers. Such a water bilayer phase may exist for several days at room temperature in air.[89]

Detailed studies of the resulting MoS_2 have been performed to examine whether the structure of such new forms of MoS_2 are the same as bulk 2H-MoS_2. Extended X-ray absorption fine structure (EXAFS) spectroscopy investigations[89] found two distinct

nearest Mo-Mo distances of 2.8 Å and 3.8 Å for single-layer MoS_2 in suspension, and that the 2H-MoS_2 lattice constant of 3.16 Å reappeared in the water bilayer MoS_2. The same experiments found that the Mo-S distance in both single layer aqueous suspensions and water bilayer form is essentially unchanged from that of 2H-MoS_2. Since EXAFS basically reveals local structural information around individual atoms, the overall structure of the material could not be inferred from the results. X-ray diffraction and Raman scattering results[92, 93] show that both single-layer MoS_2 in suspension and a water bilayer MoS_2 have a structure in which the Mo atoms are octahedrally coordinated in contrast to the trigonal prismatic coordination that pertains in 2H-MoS_2. In addition, evidence was obtained[92, 93] for the existence of a $2a_0$ superlattice. The question of whether it is a 2x2 or 2x1 superlattice was left open, because both structures would yield a similar X-ray diffraction pattern and Raman spectra. If the restacked MoS_2 is allowed to dry the structure transforms back to the trigonal prismatic coordination of Mo atoms with the bulk 2H-MoS_2 lattice constant, and the layers can exhibit partial rotational disorder.[89, 92]

In an attempt to resolve the question of the superlattice structure, atomic resolution images of restacked MoS_2 surfaces were obtained with the STM(described in Chapter 2) operating in air.[94, 95] In this Chapter, we demonstrate that the real-space image of water-bilayer MoS_2 surface shows a 2x1 super-structure directly and unambiguously. The image of a dry restacked MoS_2 film shows the same structure as that for crystalline 2H-MoS_2, in good agreement with other experiments previously reported.[89, 92] Finally, the basal plane lattice parameters obtained from the images were used, in conjunction with the previous EXAFS data, to derive a possible unit cell structure for the single-layer of MoS_2.

5.1 Single-layer MoS_2 sample preparation

The preparation of single-layer MoS_2 in suspension has been described previously.[88] By soaking 2H-MoS_2 powder in a solution of n-butyl lithium in hexane for at least 48 hours in an argon atmosphere, one can obtain stage 1 lithium-intercalated MoS_2 (Li_xMoS_2) with a mole fraction of at least x=1. When the dry intercalation compound powder is immersed in water, the water and the intercalated lithium interact to form hydrogen gas between the MoS_2 layers, and the expansion of this gas tends to separate the layers. As the reaction proceeds more deeply into each crystallite the layers become further separated. Therefore, the compound becomes completely exfoliated into single-layer MoS_2 layers which remain suspended in the aqueous solution.

In order to form a thin, flat restacked film suitable for imaging the MoS_2 basal plane, a graphite substrate has been used to provide good electrical contact to the MoS_2 layers. The sample electrode is then placed on the graphite, and a tiny drop of the single-layer MoS_2 suspension is spread out on the freshly cleaved surface of the graphite. After a few minutes the drop has adopted a quasi-equilibrium configuration with the MoS_2 layers restacked in the water bilayer phase. The thickness of the film is approximately the order of 10 monolayers of MoS_2 as estimated from the concentration of the single layer suspension. The sample was imaged within a few hours after preparation. The reason we have selected graphite as the substrate is because it is very inert and it is easy to obtain large regions that are atomically flat. This results in an almost ideal substrate for operating the STM in air, and for obtaining a rather flat restacked MoS_2 film.

Since the sample has a bilayer of water between the MoS_2 layers, an ultra-high-vacuum (UHV) environment would not be appropriate for the observations.

In order to get dry restacked MoS_2, we first make the water-bilayer restacked film, and then accelerate the drying process by heating the sample, including the graphite substrate, at 100°C in a vacuum of ~ 10^{-3} Torr for 5 hours.

5.2 Experimental results

(a) X-ray diffraction measurement

Fig.5-1 shows x-ray diffraction patterns of a freshly deposited MoS_2 film on graphite, obtained from an aqueous suspension. The measurement was carried out with a Philips diffractometer using nickel-filtered Cu $K\alpha$ radiation. In the figure, the solid curve was obtained a few minutes after the film was deposited and the black dots were taken 5 hours later. At small angles two peaks appear, which are located at the diffraction angles 2θ = 7.5° and 14.9°, corresponding to the (001) and (002) reflections of separated MoS_2 layers. From x-ray diffraction formula we know that

$$2\theta = 2\ sin^{-1}\left(\frac{\lambda l}{2c}\right).$$

With an x-ray wavelength of λ =1.542Å, the two peaks (i.e. l =1 and l =2) give a same spacing between Mo planes of c = 11.8Å. For crystalline 2H-MoS_2 or dry restacked MoS_2,[89] the c-spacing between Mo-planes is 6.2Å corresponding to an x-ray diffraction peak located at 2θ = 14.28°, which is not found in Fig.5-1. Therefore the c-spacing has been expanded by 5.6Å in freshly deposited MoS_2 film. The expansion value is smaller than 6.2Å, the thickness associated with a single molecular layer of 2H-MoS_2, but does,

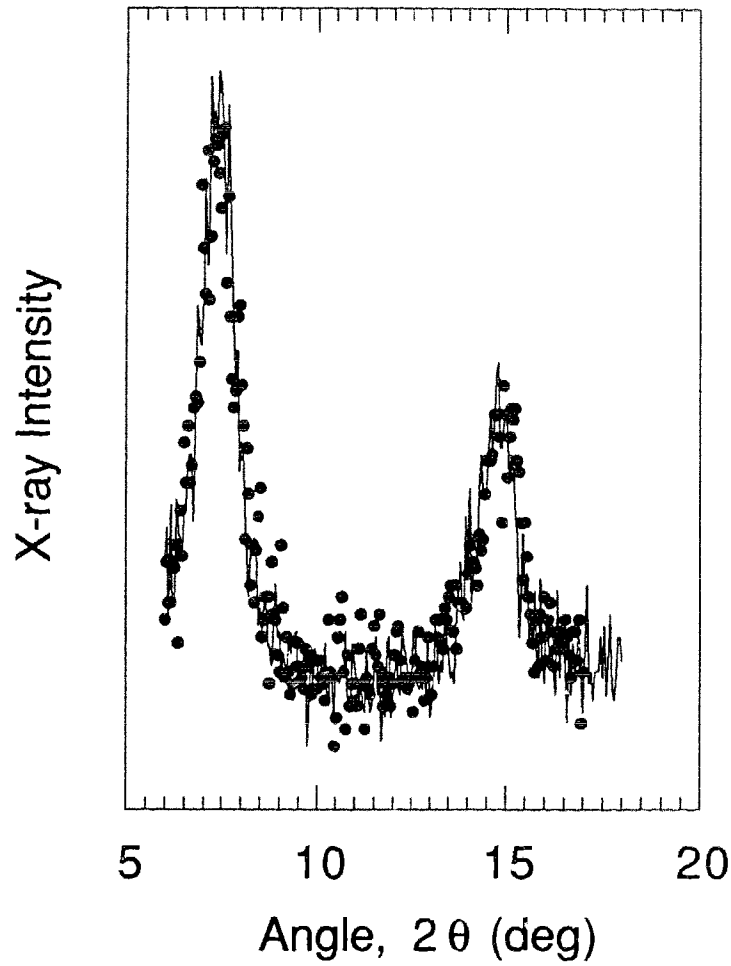

Fig.5-1: X-ray diffraction patterns of a water-bilayer form of MoS_2 restacking film on graphite. The solid curve was obtained immediately after the film was made and the black dots were taken 5 hours later.

however, agree closely with the twice of the size of a water molecule. It appears that each layer of MoS_2 hosts an adsorbed monolayer of water approximately 2.8Å thick, and the layers are closely stacked so that *there are two layers of water between MoS_2 layers.*

Apparently, there is almost no difference between the two sets of data in Fig.5-1, indicating that the water-bilayer phase of the MoS_2 film is stable in air for at least 5 hours, which is certainly long enough for performing the STM experiments.

(b) STM images of single layers of MoS_2

As we have seen in Chapter 4, the 2*H* -MoS_2 image (see Fig.4-2) obtained by the STM shows the expected hexagonal structure with the measured lattice constant $a_0 = 3.1 \pm 0.1$ Å, which is in good agreement with the crystallographic value of 3.16 Å.[66] Fig.5-2 is a current image of a water bilayer MoS_2 surface, taken with a positive tip bias of 42 mV, an average tunneling current 2nA and a scan rate of 1830Å/sec. The image clearly shows an approximate 2x1 structural pattern with a basal plane unit cell containing two bright spots. Previous studies on this material, including x-ray diffraction and Raman scattering, have indicated that there is a $2a_0$ superstructure, but the exact pattern of the structure could not be obtained by either method. The STM image allows us to see the real-space 2x1 form of the lattice directly and unambiguously. The sample has been scanned in perpendicular directions to ensure that the 2x1 pattern is not due to a tip effect. Also, the structure was found to be independent of tip bias polarities. The sample surface was not parallel to the tip scanning plane as indicated by the decrease in image intensity as one moves to the right in the image.

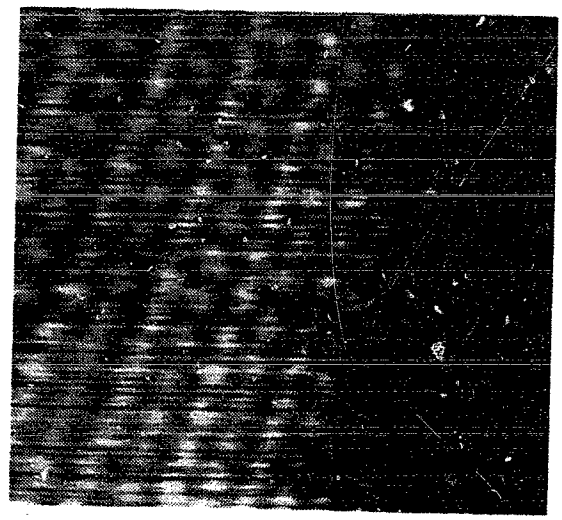

Fig.5-2: A constant-height image (~40Å x 33Å) of a water-bilayer MoS_2 surface. A stripe-like 2x1 superlattice structure is apparent.

Fig.5-3(a) is an image of another sample with the same experimental conditions as for Fig.5-2. It appears that the surface was not tilted with respect to the tip scanning plane in the central part, but was bent down slightly at both right and left sides of the image. By superimposing a grid on the image as shown in Fig.5-3(b), the 2x1 superlattice is more obvious, and the basal plane projection of the unit cell are shown schematically in Fig.5-4. After calibrating a number of images obtained from this sample at different surface locations, we measure the lattice parameters as $|\mathbf{a}| = 3.2 \pm 0.1$ Å, $|\mathbf{b}| = 6.1 \pm 0.2$ Å and $\alpha = 53 \pm 1°$.

Comparing the lattice constant $a_0 = 3.1 \pm 0.1$ Å obtained from imaging the 2H-MoS_2 crystal surface as shown in Fig.4-2, we find that $|\mathbf{a}| \approx a_0$ and $|\mathbf{b}| \approx 2a_0$, hence further confirming the $2a_0$ x a_0 superlattice structure of the freshly deposited MoS_2 film surface. However, notice that the measured α is about 53°, and thus the $2a_0$ x a_0 pattern can not be considered as a simple superlattice of the hexagonal basal plane structure of 2H-MoS_2 where α should be 60°.

Fig.5-5 shows a larger area image (~132 Å x 100 Å) of the same water-bilayer surface as that in Fig.5-2. The image was taken in the constant-current mode with a tunnel current of 1.5 nA, tip bias voltage of 48 mV, and a scan rate of 1376 Å/sec. As shown in Fig.5-5 the upper and lower parts of the image represent two crystallites with different orientations. In the upper part of Fig.5-5 it can be seen that there is an array of periodic rows approximately along the vertical direction.The periodicity along the direction perpendicular to these rows is about 5 Å which is in good agreement with the distance $|\mathbf{b}|\sin\alpha$ (see Fig.5-4). Along the vertical direction, it is obvious that the periodicity is less than $2a_0$, otherwise it would have been resolved. Therefore the image still possesses the same 2x1 pattern as shown in the higher resolution but smaller scan range image (Fig.5-2). These results indicate that the 2x1 structure extends over large areas, which is then

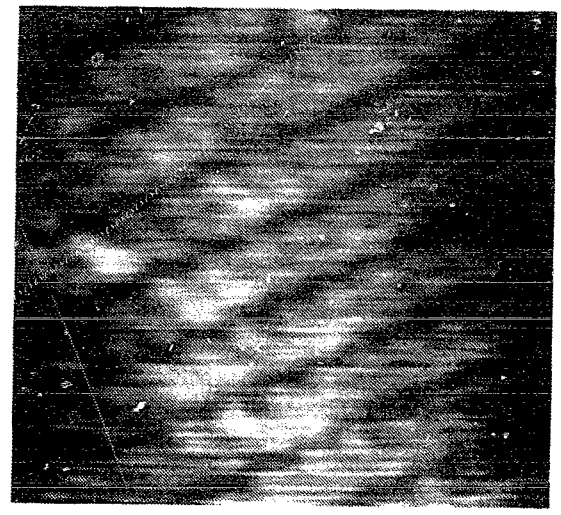

(a)

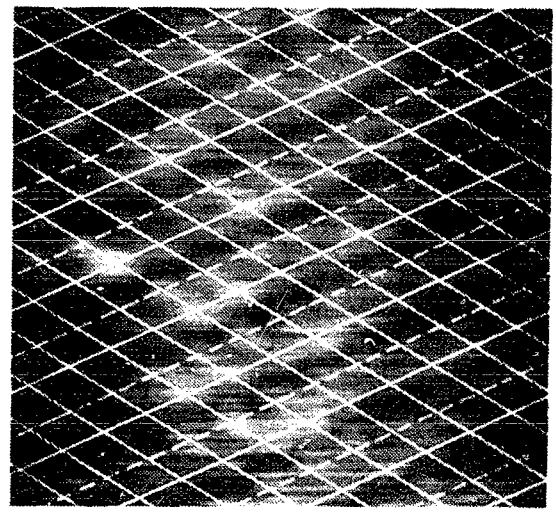

(b)

Fig.5-3: (a) A constant-height image (~38Å by 30Å) of another water bilayer MoS_2 sample.(b) The same image with a grid superimposed to show the 2x1 superstructure and its unit cell projection more clearly.

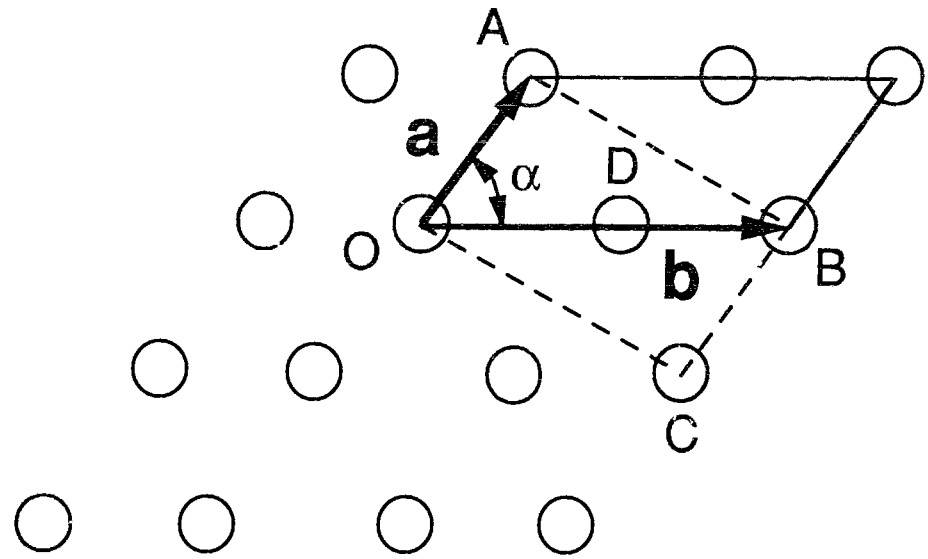

Fig.5-4: Schematic representation of the image pattern shown in Fig.5-3. The open circles represent the bright spots in the current images. The $2a_0$xa_0 unit cell is outlined with solid lines, where |**a**| = 3.2±0.1Å ≈a_0 and |**b**| = 6.1±0.2Å ≈ $2a_0$. The dashed lines show an alternative definition of a unit cell.

Fig.5-5: A constant-current image (~132 Å x 100 Å) of the same water-bilayer sample surface as that shown in Fig.5-2. The image still possesses the same 2x1 pattern as shown in the higher resolution but smaller scan range image (see Fig.5-2).

consistent with the x-ray diffraction measurement. From images obtained with even larger scan ranges the areal size of the crystallites was estimated to be ~100 x 100 $Å^2$.

Fig.5-6(a) shows a current image of a completely dry restacked MoS_2, taken at a positive tip bias of 1 V, an average tunneling current of 2 nA and a scan rate of 3627 Å/sec. The larger tip bias was used because of the consideration that the dry restacked layers have a much smaller conductivity than the water-bilayer suspensions. The image clearly shows the appearance of the hexagonal structure without any trace of the 2x1 superlattice. The lattice constant is measured to be 3.1 ± 0.1 Å (calibrated by the graphite image shown in Fig.5-6(b)) which is in good agreement with the crystallographic value of 3.16 Å, confirming that the trigonal prism layers have been recovered. This result agrees very well with that of previous experiments.[89, 92]

We believe that the STM images shown in Fig.5-2 and Fig.5-3 reflect the atomic structure of a single layer of MoS_2 at the top surface of the water bilayer phase MoS_2 film. The second MoS_2 layer from the top surface has very little effect on the tunneling image, since there are two monolayers of water between each of the MoS_2 layers which are parallel to each other but rotationally disordered,[89] and our STM observations on different samples and different surface locations of a sample all show the same 2x1 superlattice. Therefore, it is most likely that the structure of the single-layer MoS_2 in suspension has basically the same pattern as that shown in Fig.5-2 and Fig.5-3. As Raman scattering experiments[92, 93] have shown one obtains identical superlattice modes for both single-layer MoS_2 in suspension and a water bilayer MoS_2 film. EXAFS results for the Mo-Mo distances, 3.8Å and 2.8Å, are also obtained from both forms.[89] However, the structure may not be exactly the same for the two cases due to slightly different water environments. As was shown in the EXAFS experiments, the bulk lattice constant 3.16Å, which is not observed in the single-layer suspension, reappears in the water bilayer form.[89]

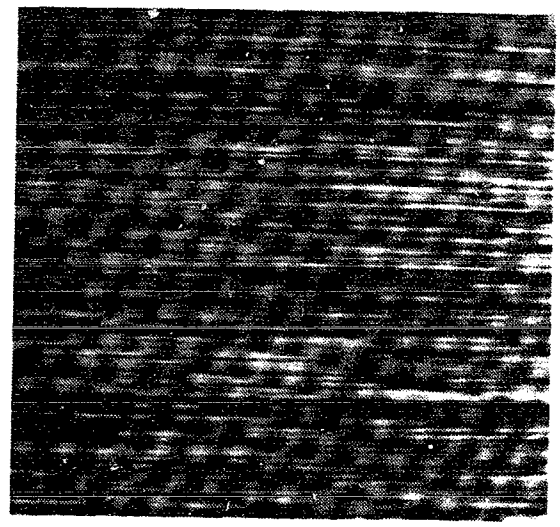

(a)

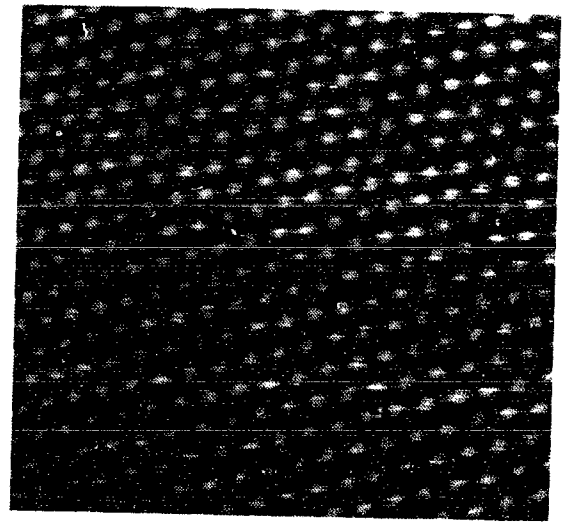

(b)

Fig.5-6: (a)A constant-height image (~46 Å by 41 Å) of a dry restacked MoS_2 surface. (b) The calibration image obtained from the substrate graphite surface with the same experimental conditions as that of the above image.

Fig.5-7 shows two current images that were obtained from two different water-bilayer MoS_2 films. The common feature is that a domain boundary appears on the surfaces, though the underlying reason for this is not yet clear. As shown in Fig.5-7(a), we see two domains with differently oriented parallel rows. Obviously, the 2x1 pattern is still there for both domains despite the lack of atomic resolution in the image. The x scale (about 32Å) is smaller than the y scale in the figure, mainly due to different drive voltages added on the x and y piezoelectric bimorphs. An atomic resolution image is shown in Fig.5-7(b). One can see that there is a hint of a domain boundary appearing in the lower-left part of the image, as the bright spots tend to be equal in size, equally spaced and the 2x1 pattern tends to be oriented along the direction rotated ~120° counter-clockwise. These domain structures may be caused by the edge effect of the second MoS_2 layer under the top layer, and the water molecules may be ordered relative to adjacent MoS_2 layers.

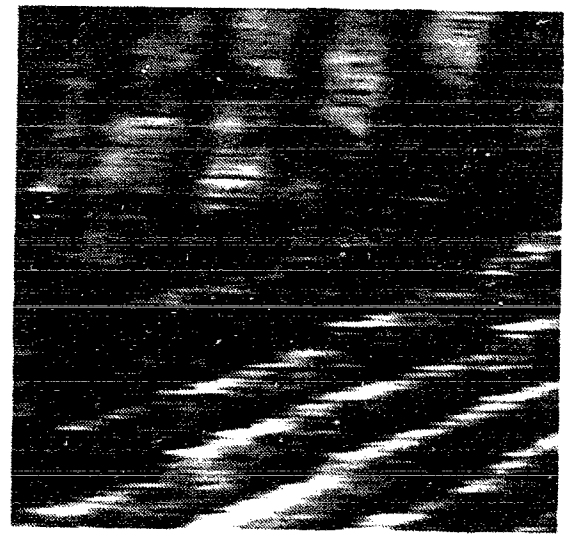

(a)

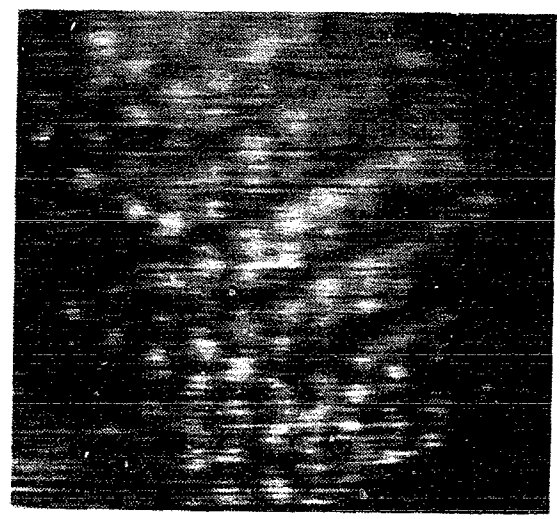

(b)

Fig.5-7: Domain structures appear on the surfaces of two different the water-bilayer MoS_2 samples imaged in the constant-height mode. The distortion is apparent in (a), which is due to the different x and y scales presented on the computer screen from which the photograph was taken.

5.3 A possible unit cell structure

Comparing EXAFS results with our STM measurements for freshly restacked MoS_2, one obvious aspect is that the single crystal 2H-MoS_2 lattice constant has been found by both methods. It is more difficult to find a direct correspondence between two nearest Mo-Mo distances 3.8Å and 2.8Å obtained by EXAFS and the lattice constants determined from the STM images. Since the STM probes the local electron density of states around the Fermi level of the surface,[23, 24] the bright spots in the current image do not necessarily correspond to the positions of individual atoms of the surface.[25] On the other hand, the STM image must reflect the projection of the real lattice. As one can tell from Fig.5-2, the image can be viewed as an array of two rows of spots not quite identical in size and brightness. One possible reason is that the surface is periodically buckled.

Combining the $2a_0$ x a_0 pattern with $\alpha = 53°$ measured by STM with the three nearest Mo-Mo distances (3.16 Å, 3.8 Å and 2.8 Å) given by EXAFS, we can construct a model for the unit cell which is shown in Fig.5-8. For $\alpha = 53°$, $\overline{OA}$ = |a| and $\overline{OB}$ = |b| measured by the STM to be consistent with the Mo-Mo distances measured by EXAFS , one row of Mo atoms has to be displaced vertically by $h = 0.9$Å. The D' point on the projection plane is then slightly displaced (~ 0.05 Å) from the $\overline{OB}$ line according to the model. Such a small difference would not be detectable in the STM images shown in Fig.5-2 and Fig.5-3. Also, the projected lines $\overline{AD'}$= 3.04 Å and $\overline{D'C}$ = 2.65 Å (shown in Fig.5-8) calculated with h = 0.9 Å are in agreement with the lengths $\overline{AD}$ = 3.0 ± 0.1 Å and $\overline{DC}$ = 2.6 ± 0.1 Å (shown in Fig.5-4) measured with the STM.

We know from Chapter 4 that WTe_2 possesses a distorted octahedral layer structure, whose basal plane projection is similar to the structure shown in Fig.5-4. In the WTe_2

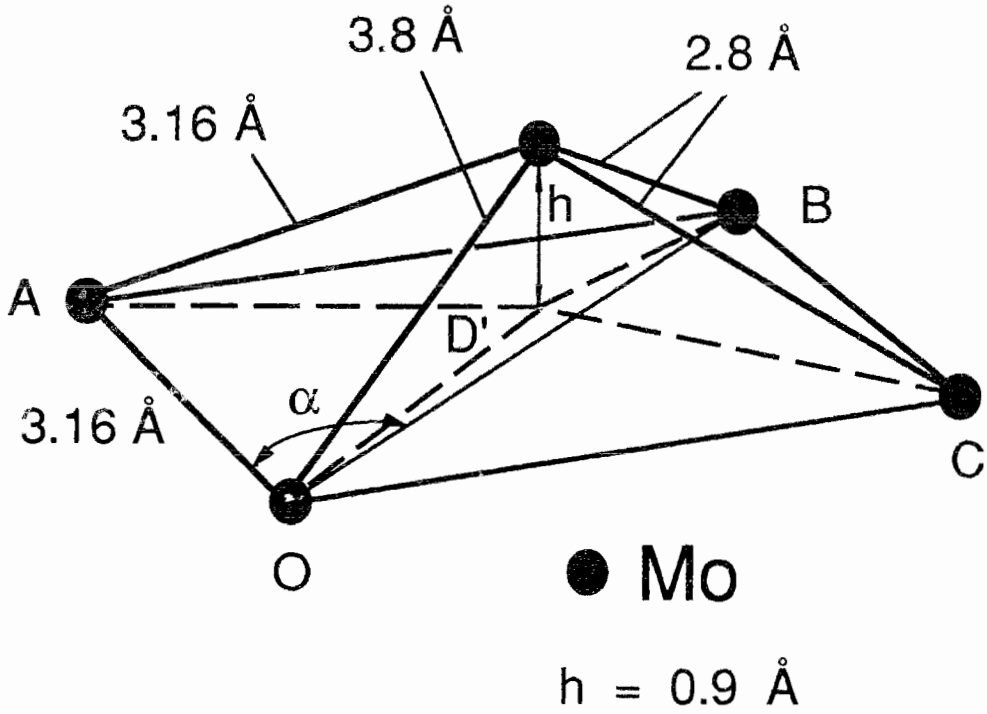

Fig.5-8: Schematic 3D perspective model for consistency between results obtained from STM and EXAFS. The solid lines represent the unit cell of Mo atoms based on the bond distances obtained by EXAFS. The dashed lines represent the projections of the corresponding solid lines in the projection plane, where $\alpha = 53\ °$, $\overline{OA} = |\mathbf{a}| = a_0$, and $\overline{OB} = |\mathbf{b}| = 2a_0$, as given by STM.

structure the adjacent rows of W atoms are displaced by 0.21 Å. With the unconstrained single layer MoS_2 a larger distortion then that found in crystalline WTe_2 is not unreasonable. If it is assumed that the STM images reflect the relative positions of the Mo atoms, an *h* value of 0.9 Å must be considered to be very large. For example, one might expect a 0.9 Å layer corrugation to result in a current varying by about one order of magnitude for a clean tip and surface.[3, 4] However, the possibility of a 0.9 Å corrugation cannot be ruled out. Since we operate the STM in air, contamination on the tip and the sample surface can reduce the effective tunnel barrier height,[3, 4] hence a 0.9 Å corrugation may result in a current variation much less than one order of magnitude. These type of effects thus make it very difficult to draw any conclusions from the images (Fig.5-2 and Fig.5-3) about the relative heights of adjacent atomic rows and any variation in relative heights that might be suggested by a comparison of different images. On the other hand it is perhaps possible that the S atom planes are less rippled than the Mo atom planes. The STM images could then be interpreted as support for the view that tunneling is occurring between the tip and the surface sulfur atoms. Additional experimental evidence will be required to resolve this question.

5.4 Conclusions

In conclusion, STM observations in air have been carried out on single MoS_2 layers separated by a bilayer of water molecules. The atomic resolution images clearly show an approximate 2x1 superlattice structure for the single-layer of MoS_2 at the top of the film surface. One of the basal plane lattice constants is found to have the same value as the bulk 2H-MoS_2 case, and the other one is about twice that of the bulk value. After drying by heating or aging, the atomic arrangement of restacked MoS_2 layers transforms back to the

bulk hexagonal trigonal prism structure, and the measured lattice constant is found to be in good agreement with the single crystal value.

Chapter 6

Scanning tunneling microscopy of single-layer MoS_2 in butanol

It has been shown [88, 89] that single molecular layers of MoS_2 can be obtained by the exfoliation of lithium-intercalated MoS_2 powder not only in water but also in several alcohols.

In Chapter 5 we have studied the structure properties of the water-bilayer MoS_2 surface, and a 2x1 superstructure pattern has been unambiguously observed in the STM images. However, whether the water is the reason causing such a structure is a natural question. To investigate the role played by the water molecules in determining the structural properties of the single layers, and to investigate the influence of the MoS_2 single layer and solvent layer interface interaction on the basal plane structure, suspensions have been prepared in butanol [$CH_3(CH_2)_3OH$] and STM experiments were carried out on the surface of butanol-bilayer MoS_2 films on graphite substrates. Atomic resolution STM images from the single layers of MoS_2 in butanol again reveal the existence of a 2x1 superlattice, which is qualitatively similar to that obtained from the aqueous suspensions.[95] Therefore, these results suggest that the 2x1 pattern may be the intrinsic structural form of single-layer MoS_2.

In this Chapter, we describe the procedures used to obtain the STM images and compare the results obtained from the butanol and water suspensions.

6.1 Sample preparation

The butanol suspension used was made as follows. The lithium-intercalated MoS_2 was obtained first as described in Ref.[88], then exfoliated in methanol, and washed with n-butanol using centrifuging methods, with the washing procedure repeated at least three times.

As in the water case (see Chapter 5), graphite was used as the substrate, and a tiny drop of the single-layer MoS_2 suspension was deposited on it. After a few seconds, instead of a few minutes for the water case, the drop adopted a quasi-equilibrium configuration with the MoS_2 layers restacked in the solvent bilayer phase. The film is more than 10 times thicker than the situation for the water-bilayer film as estimated from the relative concentrations of the single-layer suspensions.

In order to obtain dry restacked MoS_2, the drying process can be accelerated by heating the sample, including the graphite substrate, at 70°C in a vacuum of ~ 10^{-3} Torr for 6 hours. Then the sample was kept in the vacuum at room temperature for up to 12 hours before imaging.

6.2 Experimental results

(a) X-ray diffraction measurement

The single layers of MoS_2 in a butanol suspension were deposited on graphite as mentioned above and were first investigated using x-ray diffraction.

Figure 6-1 shows x-ray diffraction patterns of a butanol suspension MoS_2 film on graphite. The solid curve in Fig.6-1 was obtained immediately after the film preparation

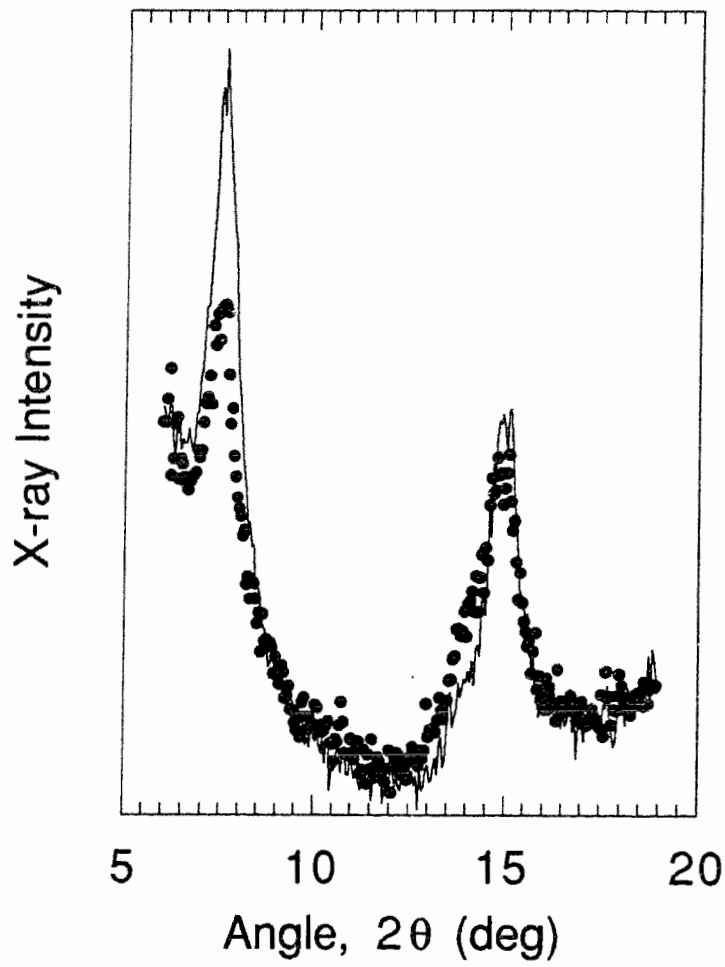

Fig.6-1: X-ray diffraction patterns of a butanol-bilayer form of MoS_2 restacked film on graphite. The solid curve was obtained immediately after the film preparation and the black dots were taken 4 hours later.

and the black dots were taken 4 hours later. Again, there are two peaks appeared at the diffraction angle $2\theta = 7.5°$ and 14.9° respectively, corresponding to the (001) and (002) reflections of separated MoS_2 layers.

From the figure it is evident that the intensity of the peak at 7.5° has decreased after four hours and is accompanied by a shoulder at an angle corresponding to the bulk 2H-MoS_2 value of 14.28°. This indicates that some of the butanol has evaporated after four hours, probably from regions near the edges of the crystallites. It should be noted, however, that all our images were obtained within two hours after preparing the film.

The peak positions shown in Fig.6-1 indicate that the c-spacing between two Mo planes in the film restacked from the butanol suspension is the same as that in the film restacked from the water suspension. Although butanol and water molecules are quite different in size, they both have an OH group which may play a major role in the c-spacing expansion, and oxygen is the largest element in both molecules. On the other hand, the energetically favorable configuration of the butanol molecule in the restacked film may be with its longer dimension parallel with the MoS_2 plane. This could yield a c-spacing between Mo planes identical to that of the water-bilayer MoS_2 film. That is, there are two monolayers of orientated butanol molecules in between two MoS_2 single layers.

(b) STM measurements

Fig.6-2 shows two current images of a butanol-bilayer MoS_2 surface at slightly different locations, taken with a positive bias voltage of 85 mv, an average tunneling current of 1 nA and a scan rate of 1830Å/sec. We see that the images still show a 2x1 superlattice pattern similar to the water-bilayer case.

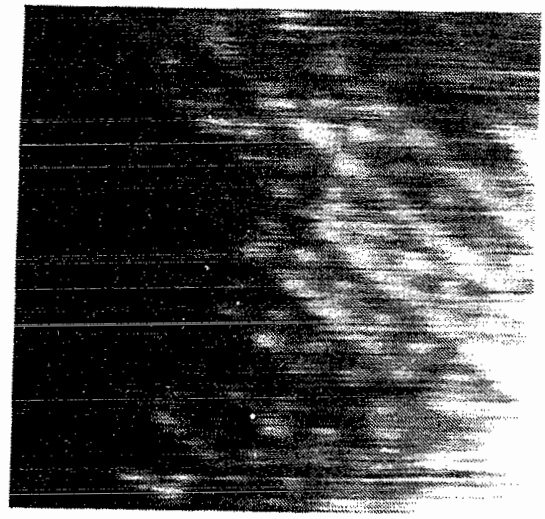

(a)

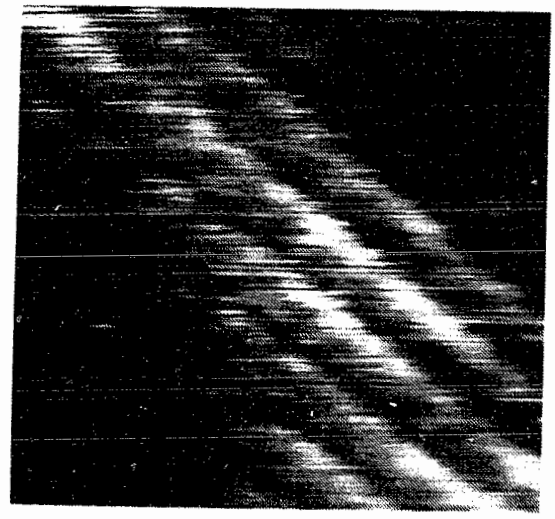

(b)

Fig.6-2: Constant-height images (~32 Å x 47 Å) of a butanol-bilayer MoS_2 surface at two different locations.

To obtain the lattice constants, Fig.6-2 was calibrated using graphite images taken under the same conditions. The calibrated unit cell parameters are |**a**|= 3.9± 0.2Å, |**b**|= 5.9± 0.2Å and $\alpha = 60 \pm 1°$(see Fig.5-4). These values are different from those obtained in water-bilayer case; especially, a larger expansion along the **a** direction. We have calibrated a dozen images obtained from two independent samples at different surface locations, and the resulting **a** value is 3.9 ± 0.3Å, still the same expansion. If the butanol molecules are ordered relative to adjacent MoS_2 layers, a different lattice distortion in the top single-layer MoS_2 is perhaps not unreasonable.

Nevertheless, from Fig.6-2 it can be seen clearly that the MoS_2 supported by the butanol-bilayer has a "2x1" superstructure that is qualitatively similar to that of the water-bilayer case. The expression 2x1 is put in quotation marks to indicate the fact that the lattice constant in the **a** direction does not appear to have the same value as that in the 2H-MoS_2 crystal.

6.3 Comparisons of different solvent results

From the previous discussion we see the common point in the surfaces of MoS_2 single layers separated by different solvent materials is the approximate "2x1" reconstruction. In the water-bilayer case it is almost a true 2x1 reconstruction of the 2H-MoS_2 hexagonal basal plane except for a small change in the angle α, whereas in the butanol-bilayer case the difference appears in the **a** direction lattice constant. The "2x1" pattern seems to be the intrinsic structural form of single-layer MoS_2, which, however, can be modulated by the interface interaction between the MoS_2 layer and the solvent molecules.

An interesting experiment was also carried out for the dry restacked MoS_2 sample. The parameter **a** was measured (from images at different surface locations) to be 3.2 ± 0.2Å, approaching the crystallographic value of 3.16Å for 2H-MoS_2. In many cases, the expected hexagonal structure pattern was observed in the STM images without any trace of superlattice. However, we did observe a likely 2x1 structure at a few surface locations *even though* the |a| is still measured to be around 3.2Å, as shown in Fig.6-3. This effect indicates that butanol molecules are most likely responsible for the large expansion along the **a** direction in the bilayer MoS_2 film, since the expansion disappeared with the absence of butanol alcohol after drying of the film. The remaining 2x1 structure may be related with the sample preparation procedure. Besides butanol molecules, there might be other smaller compound units in between the MoS_2 layers in the bilayer restacked film, which can not be dried out. They could exist between MoS_2 layers even in the dry restacked films, thus isolating the top MoS_2 single-layer from the second layer, and hence the intrinsic 2x1 structure of the single-layer could be kept unchanged. From our sample making process, the possible candidate for the units is lithium-methoxide formed from lithium and methanol during the exfoliation process, which is smaller then a butanol molecule and about the size of a water molecule. Thus the image of such a dry restacked film would be close to the image of water-bilayer case. Since the image quality obtained was not good enough for a quantitative extraction of other lattice parameters, we are not able to give further detailed measurement about the structure. Obviously, further investigations are necessary to confirm the contents of the material as well as the structure by other experimental techniques.

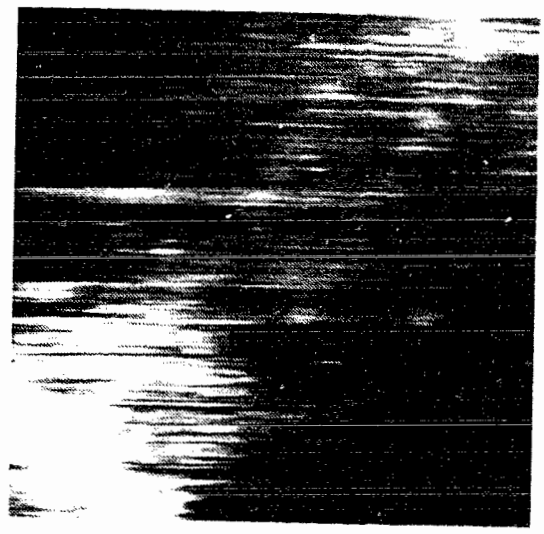

Fig.6-3: Constant-height image (~35 Å x 32 Å) of a dry restacked MoS_2 sample obtained from drying a butanol-bilayer MoS_2 film.

6.4 Mechanism speculations

The interactions between MoS_2 layer and solvent molecules could be elastic and electronic. Since the single layers in water and butanol suspensions appeared qualitatively with the same "2x1" pattern, the quantitative differences may be due to the elastic interaction, because butanol molecule size is larger than that of a water molecule. There might be possibilities that the solvent molecules influence the MoS_2 layers electronically, and cause the distorted octahedral structure.

The role of the suspension liquid in modifying the electronic structure is not clear. It is known that the intercalation of alkali metal[96] or of organic molecules[97] in some transition metal dichalcogenides can result in compounds with structure differing from those of the parent material. The electronic properties of these compounds would change due to charge transfer from the intercalant to the host material, and a modification of the band structure must also be considered due to the change in structure.

The experimental results of Py and Haering[96] on Li-intercalated MoS_2 indicated a transformation of the layers from trigonal prismatic to distorted octahedral, due to the charge transfer from the Li to the MoS_2 which increases the number of the non-bonding electrons on Mo *d* orbitals from 2 to 3 (i.e. from d^2 to d^3).[98] As was shown by Kertesz and Hoffman,[98] the number of non-bonding electrons on transition metal *d* orbitals (d^n) in a transition metal dichalcogenide is a key factor to determine its coordination structure. Based on the band structure and total energy calculations, they concluded that for d^0 the octahedral structure is more stable; then filling the lowest *d* bands starts to favor the trigonal-prismatic structure; for d^3 again the octahedral geometry is more stable, and metal clustering may occur to form a distorted structure like Re_4 in $ReSe_2$ (see Fig.4-9). Indeed, Chrissafis *et al*[99] observed a $2a_0$x$2a_0$ superstructure for the Li-intercalated MoS_2. The

overall structure is then quite similar to that of $ReSe_2$ crystal (Chapter 4), in agreement with a model proposed by Kertesz and Hoffman.[98] However, $ReSe_2$ is a semiconductor while Li-MoS_2 is more metallic,[96] indicating that there are some detailed differences between the two materials.

After the exfoliation process, solvent molecules (either water or butanol) are in between the MoS_2 layers instead of lithium atoms. It is reasonable to believe that the single layers of MoS_2 would possess a structure which might be different from that of both crystalline 2*H* -MoS_2 (i.e. 1x1 lattice) and Li-MoS_2 (i.e. 2x2 superlattice similar to $ReSe_2$), and might be a slight modification of both. The observed "2x1" superstructure is the expected intermediate result. As revealed by optical absorption measurements[92] and Raman scattering experiments,[93] MoS_2 single layer suspensions possess distorted octahedral structure and show an increase in metallic behavior. These properties are similar to that of crystalline WTe_2 (Chapter 4). In analogy with Li-intercalated MoS_2, we may speculate that the solvent molecules might provide a kind of driving force for the Mo atoms to form Mo-Mo-bonded zigzag chains, just like the W atoms within a WTe_2 layer. It has been reported that organic molecules, such as pyridine, intercalate into TaS_2 and form a bond by donating electrons to partially filled sulfur orbitals (x-ray electron emission measurements indicate that the bonding is to the nitrogen atoms in the organic molecule).[97, 100] Therefore, we might speculate that a similar bonding mechanism exists in both the water and butanol suspensions, which could result in the distorted octahedral structure and increased conductivity of the single MoS_2 layers in suspension. Further experiments will be required to corroborate these speculations.

Chapter 7

Summary and outlook

7.1 Theoretical section

We have presented the first theory of the STM images of the surfaces of staged graphite intercalation compounds (GIC's). We found that the corrugation amplitude (CA) and carbon-atom site asymmetry (CSA) are very sensitive to the number m of graphite layers covering the first guest layer and the charge transfer value, but insensitive to the bulk stage due to the screening of intercalant layers. The CA increases with increasing m, with decreasing charge transfer, and also with decreasing tip-to-surface separation. The CSA does not strongly depend on the tip-to-surface separation, but has a surprising dependence on the charge transfer and m, switching on discontinuously with decreasing charge transfer. We predict that in many cases there should be no CSA in the STM image even when the usual *AB* stacking of the graphite layers occurs at the GIC surface. For a given charge transfer, the CA is larger for acceptor GIC's and the CSA is larger for donor GIC's.

7.2 Experimental section

Graphite and three transition-metal-dichalcogenides (2*H*-MoS_2, WTe_2 and $ReSe_2$) crystalline surfaces have been imaged with a STM system assembled for operation in air. The atomic-resolution images of three transition-metal-dichalcogenides show the expected basal plane projection lattices (i.e. 1x1 lattice of the corresponding chalcogen sublattice for

2*H*-MoS_2, 2x1 superlattice for WTe_2, and 2x2 superlattice for $ReSe_2$), even though the images are not necessarily the reflections of the metal layers. There is no conclusive evidence to confirm which chemical identity has been imaged in the 2*H*-MoS_2 STM images, as there is no difference in the symmetry for both types of atom sheets. The observed zigzag pattern in the valence band WTe_2 images does not correspond to the W atomic sites, because the measured distance between the two paired rows changes with the tip-to-surface separation and is larger than the distance of the two W paired rows, indicating rather strong contribution from the surface Te atom layer. In the $ReSe_2$ surface images, we clearly observed four distinct types of bright spots which primarily represent the Se atomic sites, though the Re layer underneath has influence on the spot size and brightness and on the one spot site slightly shifted from the regular position of the Se sublattice.

We have, for the first time, successfully observed the structure of single-layer MoS_2 in suspensions with the application of the STM in air. The single molecular layers are obtained by exfoliation of Li-intercalated MoS_2 in water and in alcohols. When either an aqueous or butanol suspension of single-layer MoS_2 is deposited on graphite substrates, restacked films will be formed with solvent molecules included between layers of MoS_2. The STM images obtained from both types of films show that the unit cell of the single layers corresponds to an approximate 2x1 superlattice of the hexagonal 2*H* -MoS_2 structure. The "2x1" pattern can be modulated by the interface interaction between the MoS_2 layer and the solvent molecules. The unit cell parameters for water-bilayer MoS_2 film case, in conjunction with the published results obtained with x-ray diffraction, EXAFS and Raman scattering methods, imply that the single layers of MoS_2 adopt a distorted octahedral structure. The image of dry restacked MoS_2 obtained from an aqueous

suspension transforms back to the hexagonal MoS_2 pattern, which is also consistent with the results obtained by other methods.

Though the basal plane structure of single layers of MoS_2 has unambiguously been observed with the STM, the registration of surface atoms in the images is still uncertain. Further theoretical studies on the LDOS based on the measured single-layer MoS_2 structure would be of interest to interpret the STM images. Also further experimental and theoretical efforts are still required to solve the structure details of the atomic constituents of single-layer MoS_2, and to conform if solvent molecules play an important role in modifying the single-layer MoS_2 electronic structure. The recently developed technique of optical absorption microscopy and spectroscopy might be an appropriate method for further investigations.[101-105] By illuminating the tunnel junction of the STM with laser beam and mapping the optical absorption of the surface with atomic resolution, one can obtain the photoinduced tunneling current caused by the electron-hole pairs created by the absorption of incident radiation, and obtain an additional surface photovoltage caused by the generated extra carriers. Such induced tunneling current and photovoltage may provide information useful to study sample surface characteristics as well as chemical variations on atomic scale. It has been shown that the image obtained under illumination is different from the usual STM image,[101, 104, 105] hence simultaneously obtaining and comparing both type of images (for instance, one could record different modes for every other line in the image, then manipulate the data by computer so as to obtain separate images in registration with one another) would be helpful for the sample surface studies.

Appendix : Electronics

PREAMPLIFIER CIRCUIT

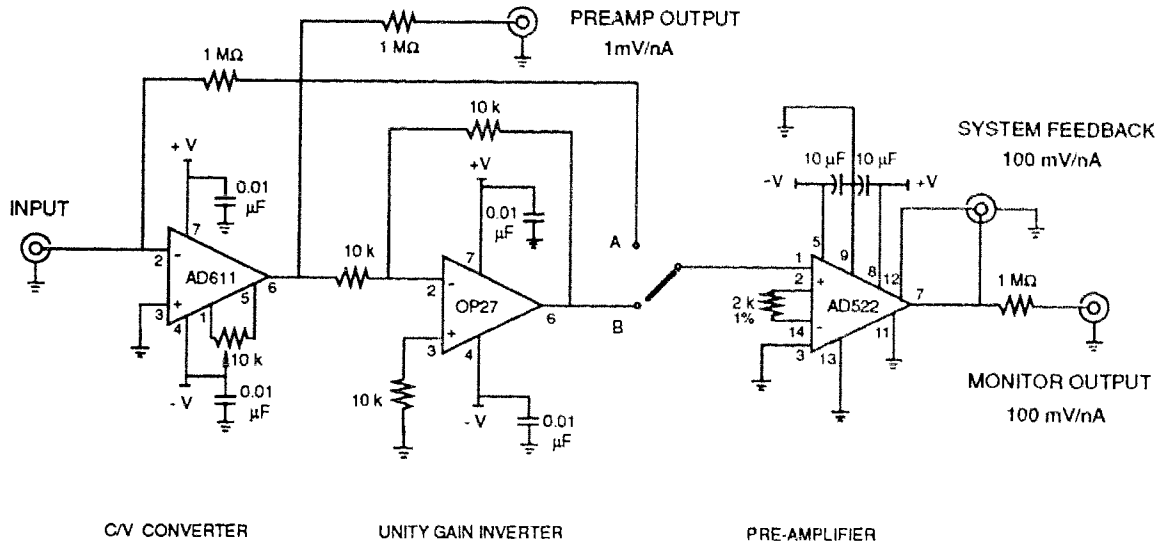

FEEDBACK MAIN CIRCUIT

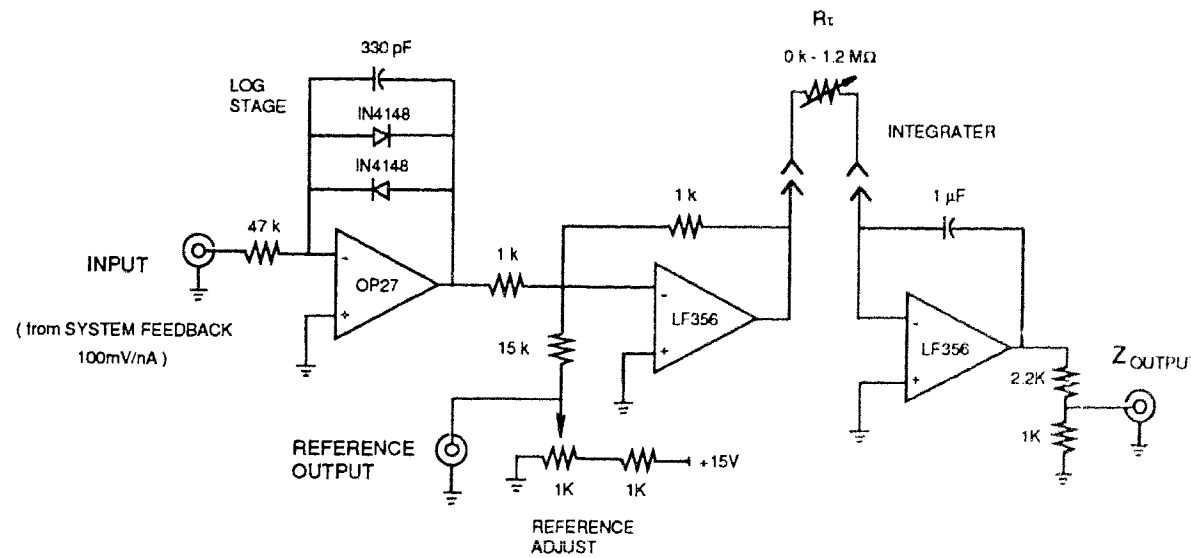

Note: The above two circuits are based on the feedback circuit designed by Dalhousie University as shown in Ref. [32]. When a positive bias voltage is applied to the tip, switch on "B", otherwise on "A".

CLAMP CIRCUIT

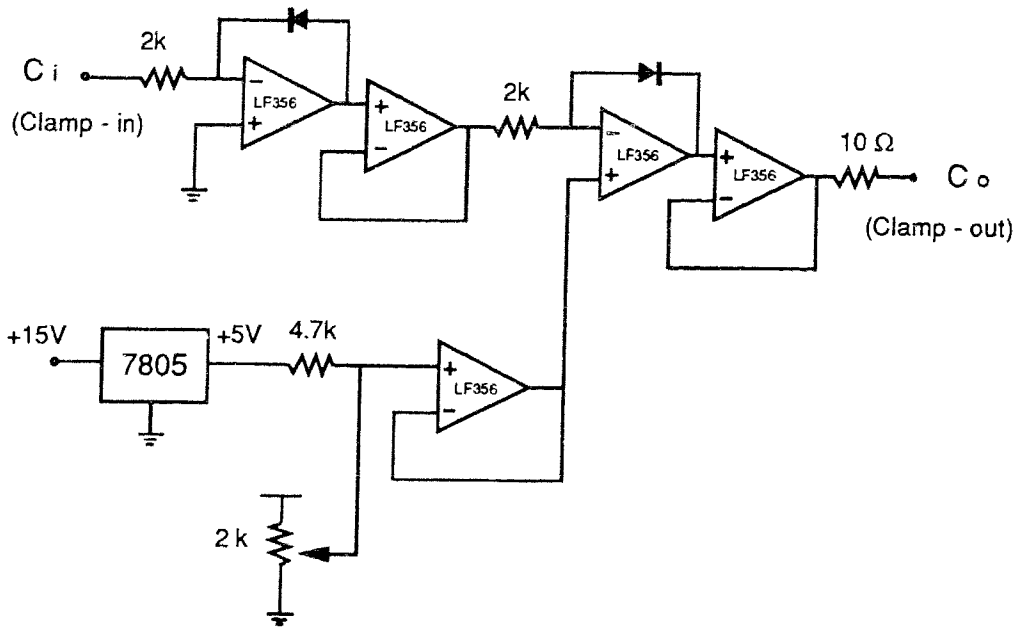

CONTRAST CIRCUIT

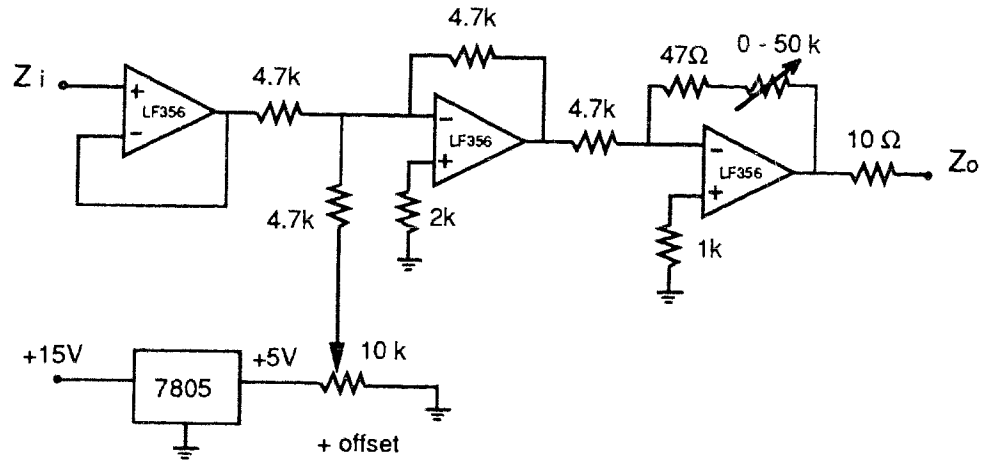

ROTATION CIRCUIT

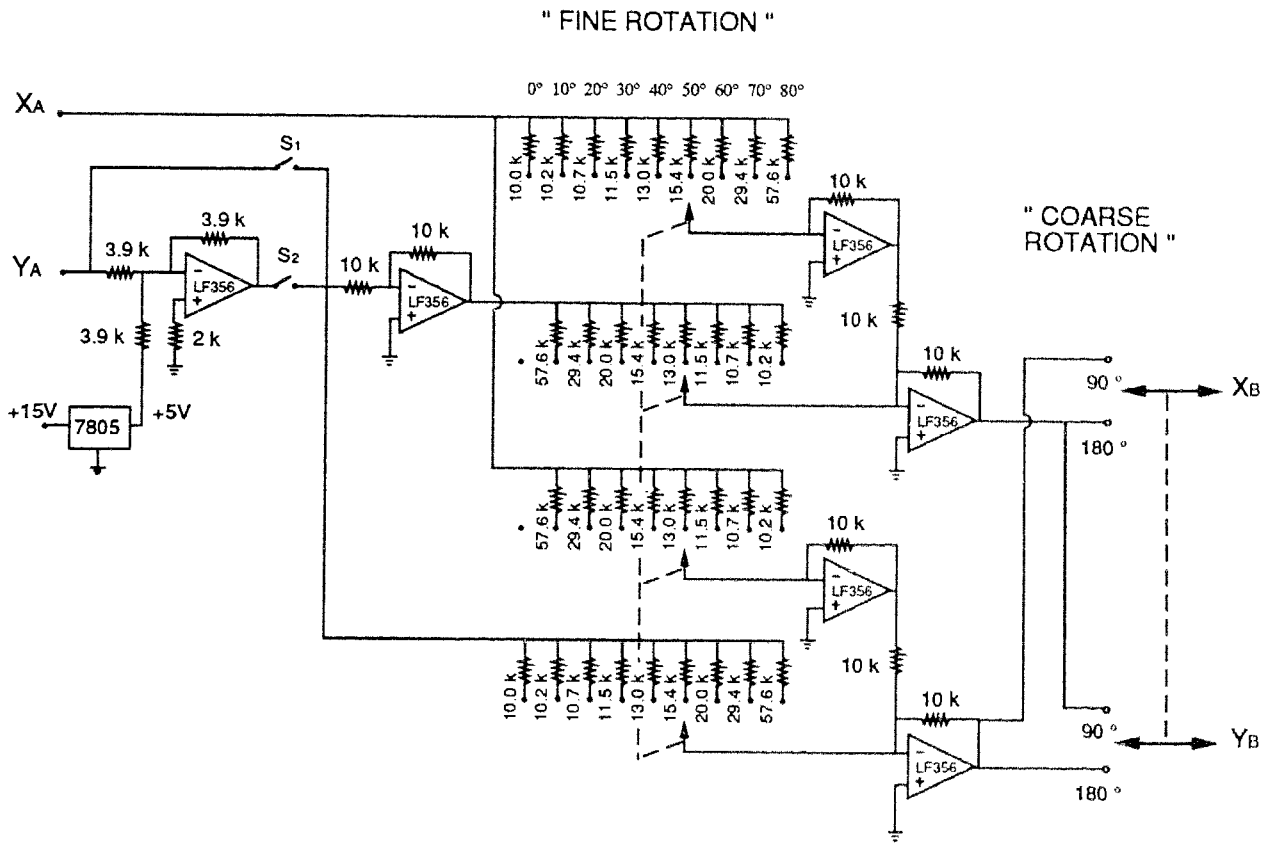

Note: The imputs "X_A" and "Y_A" are connected with the scan generator which provides ± 5V peak-to-peak voltage signols for both of the x and y outputs. In atomic scale imaging, switch on "S_1" while "S_2" is open; in large area imaging (> 200Åx200Å), switch on "S_2" while "S_1" is open for the purpose of providing the two H.V. amplifiers (KEPCO OPS 1000B) with negative input signols.

MAGNIFICATION CIRCUIT

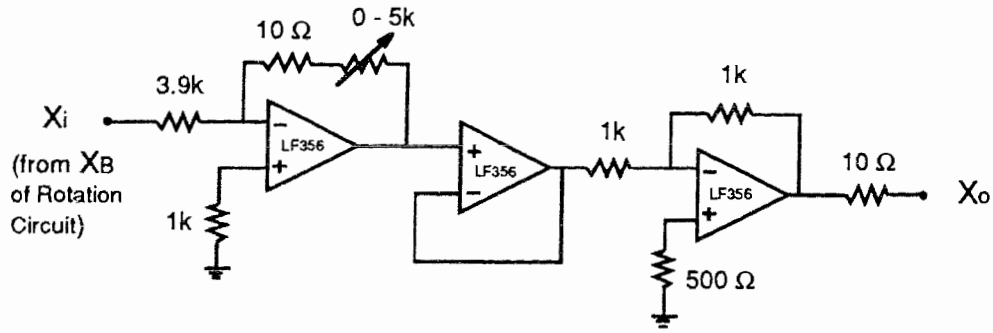

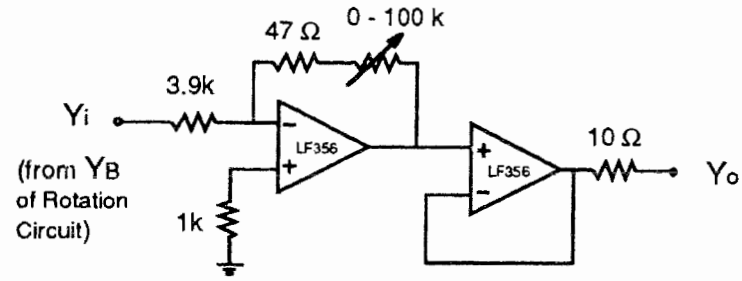

References

1. G. Binnig and H. Rohrer, IBM J. Res. Develop. **30**, 355(1986).
2. P.K. Hansma and J. Tersoff, J. Appl. Phys. **61**, R1(1987).
3. G. Binnig, H. Rohrer, Ch. Gerber , and E. Weibel, Appl. Phys. Lett. **40**, 178(1982).
4. G. Binnig, H. Rohrer, Ch. Gerber , and E. Weibel, Phys. Rev. Lett. **49**, 57(1982).
5. G. Binnig and H. Rohrer, Helvetica Physica Acta **55**, 726(1982).
6. G. Binnig, H. Rohrer, C. Gerber , and E. Weibel, Phys. Rev. Lett. **50**, 120(1983).
7. G. Binnig, C.F. Quate , and C. Gerber, Phys. Rev. Lett. **56**, 930(1986).
8. R.S. Becker, J.A. Golovchenko , and B.S. Swartzentruber, Nature **325**, 419(1987).
9. J.S. Foster, J.E. Frommer , and P.C. Arnett, Nature **331**, 324(1988).
10. D.M. Eigler and E.K. Schweizer, Nature **344**, 524(1990).
11. D.M. Eigler, C.P. Lutz , and W.E. Rudge, Nature **352**, 600(1991).
12. Y. Kuk and P.J. Silverman, Rev. Sci. Instrum. **60**, 165(1989).
13. Sang-il Park and C.F. Quate, Rev. Sci. Instrum. **58**, 2010(1987).
14. Sang-il Park and C.F. Quate, Rev. Sci. Instrum. **58**, 2004(1987).
15. R.V. Coleman, B. Drake, P.K. Hansma , and G. Slough, Phys. Rev. Lett. **55**, 394(1985).
16. R.V. Coleman, B. Giambattista, P.K. Hansma, A. Johnson, W.W. McNairy , and C.G. Slough, Adv. Phys. **37**, 559(1988).
17. Sang-il Park and C. F. Quate, Appl. Phys. Lett. **48**, 112(1986).
18. M. Tsukada, K. Kobayashi, N. Isshiki , and H. Kageshima, Surface Science Reports **13**, 265(1991).

19. J.G. Simmons, J. Appl. Phys. **34**, 1793(1963).

20. J. Bardeen, Phys. Rev. Lett. **6**, 57(1961).

21. W.A. Harrison, Phys. Rev. **123**, 85(1961).

22. C.B. Duke, *Tunneling in Solids* , (Academic, New York, 1969).

23. J. Tersoff and D.R. Hamann, Phys. Rev. Lett. **50**, 1998(1983).

24. J. Tersoff and D.R. Hamann, Phys. Rev. B **31**, 805(1985).

25. J. Tersoff, Phys. Rev. Lett. **57**, 440(1986).

26. I.P. Batra, N. Garcia, H. Rohrer, H. Salemink, E. Stoll , and S. Ciraci, Surf. Sci. **181**, 126(1987).

27. H.A. Mizes, Sang-il Park , and W.A. Harrison, Phys. Rev. B **36**, 4491(1987).

28. C.J. Chen, Phys. Rev. Lett. **65**, 448(1990).

29. C.J. Chen, to be published in Ultramicrocopy (1992).

30. L.A. Nagahara, T. Thundat , and S.M. Lindsay, Rev. Sci. Instrum. **60**, 3128(1989).

31. A. Selloni, P. Carnevali, E. Tosatti , and C.D. Chen, Phys. Rev. B **31**, 2602(1985).

32. B.L. Blackford, D.C. Dahn , and M.H. Jericho, Rev. Sci. Instrum. **58**, 1343(1987).

33. Channel Industries, P.O. Box 3680, Santa Barbara, CA 93105

34. Longreach Scientific Resources, RFD1, P.O. Box 549, Orr's Island, ME 04066.

35. KEPCO INC., 131-38 Sanford Ave., Flushing, NY 11352, USA

36. Data Translation, Inc., 100 Locke Drive, Marlborough, MA 01752-1192

37. Quantrum Vision Corporation, West Vancouver, British Columbia, Canada V7W 1P3.

38. G. Binnig, H. Fuchs, Ch. Gerber, H. Rohrer, E. Stoll , and E. Tosatti, Europhys. Lett. **1**, 31(1986).

39. D. Tomanek, S.G. Louie, H.J. Mamin, D.W. Abraham, R.E. Thomson, E. Ganz , and J. Clarke, Phys. Rev. B **35**, 7790(1987).

40. D. Tomanek and S.G. Louie, Phys. Rev. B **37**, 8327(1988).

41. J.M. Soler, A.M. Baro, N. Garcia , and H. Rohrer, Phys. Rev. Lett. **57**, 444(1986).

42. H.Jonathon Mamin, Eric Ganz, David W. Abraham, Ruth Ellen Thomson , and John Clarke, Phys. Rev. B **34**, 9015(1986).

43. H. Zabel and S.A. Solin. *Graphite Intercalation Compounds, Springer Topics in Current Physics* (Springer , New York,).

44. M.S. Dresselhaus and G. Dresselhaus, Adv.Phys. **30**, 139(1981).

45. Xiaorong Qin and George Kirczenow, Phys. Rev.B (Rapid Commun.) **39**, 6245(1989).

46. Xiaorong Qin and George Kirczenow, Phys. Rev. B **41**, 4976(1990).

47. S. Gauthier, S. Rousset, J. Klein, W. Sacks , and M. Belin, J.Vac.Sci. Technol. A **6**, 360(1988).

48. P. Biensan, J.C. Roux, H. Saadaoui , and S. Flandrois, Microsc. Microanal. Microstruct. **1**, 103(1990).

49. S.E. Ulloa and G. Kirczenow, Comments Cond.Mat.Phys. **12**, 181(1986).

50. S.A. Safran and D.R. Hamann, Phys. Rev. B **22**, 606(1980).

51. R. Levi-Setti, G. Crow, Y.L. Wang, N.W. Parker, R. Mittleman , and D.M. Hwang, Phys. Rev. Lett. **54**, 2615(1985).

52. M. Lagues, D. Marchand , and C. Fretigny, Solid State Commun. **59**, 583(1986).

53. J. Blinowski and C. Rigaux, Synth. Met. **2**, 297(1980).

54. J. Blinowski, N.H. Hau, G. Rigaux, J.P. Vieren, R.L. Toullec, G. Furdin, A. Herold , and J. Melin, J. Phys. (Paris) **41**, 47(1980).

55. R. Nishitani, Y. Uno , and H. Suematsu, Phys. Rev. B **27**, 6572(1983).

56. Y. Yosida, K. Sato, K. Suda , and H. Suematsu, J. Phys. Soc. Jpn. **55**, 561(1986).

57. S.A. Safran, Synthetic Metals **2**, 1(1980).

58. S.A. Safran and D.R. Hamann, Phys. Rev. B **23**, 565(1981).

59. Y. Yosida , and S. Tanuma, Synth. Met. **23**, 199(1988).

60. A. Selloni, C.D. Chen , and E. Tosatti, Physica Scripta **38**, 297(1988).

61. S.P. Kelty and C.M. Lieber, Phys. Rev. B **40**, 5856(1989).

62. F. Herman and S. Skillman, *Atomic Structure Calculations* , (Prentice-Hall, Englewood Cliffs, NJ, 1963).

63. D.M. Hwang, X.W. Qian , and S.A. Solin, Phys. Rev. Lett. **53**, 1473(1984).

64. C. Fretigny, D. Marchand , and M. Lagues, Phys. Rev. B **32**, 8462(1985).

65. M. Lagues, D. Marchand , and C. Fretigny, Annales de Physique (Paris) **11**, 49(1986).

66. J.A. Wilson and A.D. Yoffe, Adv. Phys. **18**, 193(1969).

67. G.W. Stupian and M.S. Leung, Appl. Phys. Lett. **51**, 1560(1987).

68. M. Weimer, J. Kramar, C. Bai , and J.D. Baldeschwieler, Phys. Rev. B **37**, 4292(1988).

69. J.C. McMenamin and W.E. Spicer, Phys. Rev.B **16**, 5474(1977).

70. R. Coehoorn, C. Haas, J. Dijkstra, C.J.F. Flipse, R.A. de Groot , and A Wold, Phys. Rev. B **35**, 6195(1987).

71. R. Coehoorn, C. Haas , and R.A. de Groot, Phys. Rev. B **35**, 6203(1987).

72. C.B. Roxlo, R.R. Chianelli, H.W. Deckman, A.F. Ruppert , and P.P. Wong, J. Vac. Sci. Technol. A **5**, 555(1987).

73. R.D. Audas, Ph.D thesis, Simon Fraser University, (1983).

74. Fu-Ren F. Fan and Allen J. Bard, J. Phys. Chem. **94**, 3761(1990).

75. K. Itaya and E. Tomita, Chem. Lett. 285(1989).

76. P. Carlsson, B. Holmstrom, H. Kita , and K. Uosaki, Surface Science **237**, 280(1990).

77. Richard H. Bube, *Electrons in Solids- An Introductory Survey* , (Academic Press, INC., 1981).

78. T. Tiedje, J. Varon, H. Deckman , and J. Stokes, J. Vac. Sci. Technol. A **6**, 372(1988).

79. J.E. Demuth, U. Koehler , and R.J. Hamers, J. Microsc. **151**, 299(1988).

80. S. Okayama , and et al, J. Vac. Sci. Technol. A **6**, 440(1988).

81. B.E. Brown, Acta Crystallogr. **20**, 268(1966).

82. S.L. Tang, R.V. Kasowski , and B.A. Parkinson, Phys. Rev. B **39**, 9987(1989).

83. S.L. Tang, R.V. Kasowski, A. Suna , and A. Parkinson, Surf. Sci. **238**, 280(1990).

84. J.V. Marzik, R. Kershaw, K. Dwight , and A. Wold, J. Solid State Chem. **51**, 170(1984).

85. N.W. Alcock and A. Kjekshus, Acta Chemica Scandinavica **19**, 79(1965).

86. J.C. Wildervanck and F. Jellinek, J. Less-Common Metals **24**, 73(1971).

87. B.A. Parkinson, J. Ren , and M.-H. Whangbo, J. Am. Chem. Soc. **113**, 7833(1991).

88. P. Joensen, R.F. Frindt , and S.R. Morrison, Mater. Res. Bull. **21**, 457(1986).

89. P. Joensen, E.D. Crozier, N. Alberding , and R.F. Frindt, J. Phys. C **20**, 4043(1987).

90. W.M.R. Divigalpitiya, R.F. Frindt , and S.R. Morrison, Science **246**, 369(1989).

91. W.M.R. Divigalpitiya, S.R. Morrison , and R.F. Frindt, Thin Solid Films **186**, 177(1990).

92. D. Yang, S.J. Sandoval, W.M.R. Divigalpitiya, J.C. Irwin , and R.F. Frindt, Phys. Rev. B **43**, 12053(1991).

93. S.J. Sandoval, D. Yang, R.F. Frindt , and J.C. Irwin, Phys. Rev. B **44**, 3955(1991).

94. X.R. Qin, D. Yang, R.F. Frindt , and J.C. Irwin, Phys. Rev. B **44**, 3490(1991).

95. X.R. Qin, D. Yang, R.F. Frindt , and J.C. Irwin, to be published in Ultramicroscopy (1992).

96. M.A. Py and R.R. Haering, Can. J. Phys. **61**, 76(1983).

97. F.R. Gamble, F.J. Di Salvo, R.A. Klemm , and T.H. Geballe, **168**, 568(1970).

98. M. Kertesz and R. Hoffman, J. Am. Chem. Soc. **106**, 3453(1984).

99. K. Chrissafis, M. Zamani, K. Kambas, J. Stoemenos, N.A. Economou, I. Samaras , and C. Julien, Materials Science and Engineering. B **3**, 145(1989).

100. J.F. Revelli, JR. , and W.A. Phillips, J. Solid State Chem. **9**, 176(1974).

101. D.G. Cahill and R.J. Hamers, Phys. Rev. B **44**, 1387(1991).

102. R.J. Hamers and D.G. Cahill, J. Vac. Sci. Technol. B **9**, 514(1991).

103. S. Akari, M.Ch. Lux-Steiner, M. Vogt, M. Stachel , and K. Dransfeld, J. Vac. Sci. Technol. B **9**, 561(1990).

104. C.C. Williams and H.K. Wickramasinghe, Nature **344**, 317(1990).

105. Y. Kuk, R.S. Becker, P.J. Silverman , and G.P. Kochanski, J. Vac. Sci. Technol. B **9**, 545(1991).